Area of Interest 1, CO_2 at the Interface: Nature and Dynamics of the Reservoir/Caprock Contact and Implications for Carbon Storage Performance

FINAL REPORT

October 1, 2010 through September 30, 2014

PRINCIPAL AUTHORS

PD/PI: Peter Mozley
(575) 835-5311, mozley@nmt.edu

PI: James Evans
(435) 797-1267 james.evans@usu.edu

FFRDC Co-Investigator: Thomas Dewers
(505) 845 0631 tdewers@sandia.gov

April 1, 2015

AWARD NUMBER

DE-FE0004844

SUBMITTED BY

New Mexico Institute of Mining and Technology
801 Leroy Place
Socorro, NM 87801-4750

Utah State University
1400 Old Main Hill
Logan, Utah 84322-1400

Sandia National Laboratories (FFRDC Contractor)
P.O. Box 5800 MS 0751
Albuquerque, NM 87175-0751

DISCLAIMER

ABSTRACT

We examined the influence of geologic features present at the reservoir/caprock interface on the transmission of supercritical CO_2 into and through caprock. We focused on the case of deformation-band faults in reservoir lithologies that intersect the interface and transition to opening-mode fractures in caprock lithologies. Deformation-band faults are exceeding common in potential CO_2 injection units and our fieldwork in Utah indicates that this sort of transition is common. To quantify the impact of these interface features on flow and transport we first described the sedimentology and permeability characteristics of selected sites along the Navajo Sandstone (reservoir lithology) and Carmel Formation (caprock lithology) interface, and along the Slickrock Member (reservoir lithology) and Earthy Member (caprock lithology) of the Entrada Sandstone interface, and used this information to construct conceptual permeability models for numerical analysis. We then examined the impact of these structures on flow using single-phase and multiphase numerical flow models for these study sites. Key findings include: (1) Deformation-band faults strongly compartmentalize the reservoir and largely block cross-fault flow of supercritical CO_2. (2) Significant flow of CO_2 through the fractures is possible, however, the magnitude is dependent on the small-scale geometry of the contact between the opening-mode fracture and the deformation band fault. (3) Due to the presence of permeable units in the caprock, caprock units are capable of storing significant volumes of CO_2, particularly when the fracture network does not extend all the way through the caprock. The large-scale distribution of these deformation-band-fault-to-opening-mode-fractures is related to the curvature of the beds, with greater densities of fractures in high curvature regions.

We also examined core and outcrops from the Mount Simon Sandstone and Eau Claire Formation reservoir/caprock interface in order to extend our work to a reservoir/caprock pair this is currently being assessed for long-term carbon storage. These analyses indicate that interface features similar to those observed at the Utah sites

were not observed. Although not directly related to our main study topic, one byproduct of our investigation is documentation of exceptionally high degrees of heterogeneity in the pore-size distribution of the Mount Simon Sandstone. This suggests that the unit has a greater-than-normal potential for residual trapping of supercritical CO_2.

TABLE OF CONTENTS

EXECUTIVE SUMMARY

We examined the potential influence of features at and near the interface between reservoir and caprock rocks on fluid flow. We address the question of whether such features might influence the transmission of supercritical CO_2 into and through the caprock (i.e., seal bypass). Reservoir/caprock interfaces have a variety of attributes that are imposed by stratigraphic (depositional), diagenetic, and deformational processes. In this study we focused mainly on the influence of deformation structures on fluid flow. Our approach was to first conduct reconnaissance field work to catalog potentially important features. Following this we identified a common and potentially significant type of interface structure and made it the focus of our detailed work. We focused on interfaces where deformation-band faults in the reservoir lithology transition to opening-mode fractures in the caprock lithology. Deformation-band faults are exceedingly common in sandstone reservoirs and thus such interface features are likely common elsewhere. The deformation-band faults are a low-permeability element in the reservoir (typically at least several orders of magnitude lower permeability than the host sandstone), whereas the fractures, if unmineralized, have much higher permeability than the host mudstones and fine-grained sandstones. We conducted petrographic and geochemical analyses to assess the environment of formation of the fractures and rule out the possibility that they formed during near-surface weathering. Key evidence indicating that the fractures originated at depth in the includes "bleaching" of the fracture margins due to dissolution of hematite, and the presence of pseudomorphs after pyrite and relics of pyrite along the fracture surfaces. Dissolution of hematite and precipitation of pyrite requires chemically reducing conditions, which are typically found at depth, rather than in the near surface (weathering) environment. The field and microscopic data indicate that the fractures were loci of repeated events of flow of reducing fluids.

The interfaces we studied are between the Navajo Sandstone (reservoir lithology) and the Carmel Formation (caprock lithology) and between the Slickrock Member (reservoir lithology) and Earthy Member (caprock lithology) of the Entrada Formation along the eastern flank of the San Rafael Swell in Utah. We assessed the impact of these interface features on flow by characterizing the geology and permeability characteristics of selected sites in detail, creating conceptual permeability models of the sites, and for a representative site using numerical methods to model fluid flow in the systems. We also performed modeling at larger scales to assess the impact of these features on interformational flow and transport. For the small-scale study we collected 63 permeability measurements from the Entrada Formation. Permeability measurements were made within the relatively high-permeability Slick Rock Member and the relatively low-permeability Earthy Member, using an air permeameter. The average reservoir permeability is about 3.5×10^{-12} m^2 (3500 mD). The measured deformation band permeability within the reservoir facies is about three orders of magnitude lower (2.0×10^{-15} m^2; 2.0 mD). The average permeability of the caprock facies is about seven orders of

magnitude lower ($5.0x10^{-19}$ m^2; $5.0x10^{-4}$ mD) than the reservoir. Permeability estimates based on a parallel plate model for the caprock fractures are very high ($3.3x10^{-7}$ m^2; $3.3x10^{8}$ mD). Hydrologic models of relatively small (5m x 5m) and large-scale (150m x 150m) of the reservoir-caprock interface were constructed, which incorporated this permeability data. We varied the fault properties at the reservoir-caprock interface between open fractures and deformation bands as part of a sensitivity study. The single-phase model results were driven by a relatively low lateral head gradient of 5% and are intended to represent far-field hydrologic conditions away from a CO_2 injection well (~600 m). The multi-phase models considered much higher lateral head gradients (about 500%) and are intended to represent near-field hydrologic conditions (~6 m from the CO_2 injection well). In all scenarios, relatively large calculated head and pressure gradients developed in the reservoir across relatively low permeability deformation bands. Significant transport of miscible solutes and supercritical CO_2 was predicted when the caprock fracture was present at the reservoir-caprock interface. Vertical velocities in the fracture zone for this scenario were about $3x10^{-4}$ m/s. When the deformation band was present at the reservoir-caprock interface, the vertical velocity in the fracture was about two orders of magnitude lower ($3.0x10^{-6}$ m/s). Significant leakage of supercritical CO_2 and solutes into the more permeable facies of the caprock, was observed when the permeable fracture did not penetrate the whole thickness of the caprock. Lateral flow velocities into a permeable caprock facies were $1.2x10^{-7}$ m/s for the single-phase results and $1.4x10^{-6}$ m/s for the multi-phase results. Solute exiting the reservoir via the sub-vertical fracture was about 60% and 100% of the solute mass entering the reservoir across the left boundary, for simulations that considered a fracture extending 100% and 70% across the caprock, respectively. Less pressure compartmentalization was observed in the large-scale models. The most important findings of this study are that differences in permeability at the reservoir-caprock interface have a large impact on fluid flow in the system and that seals have the capacity to store large quantities of CO_2 if permeable fractures terminate below the top of the seal.

We also assessed the relationship of these observed interface features to the larger geological structural setting in order to determine whether it is possible to predict the likelihood of their occurrence at a given subsurface site. This involved collecting detailed data on fracture orientations and fracture density at multiple sites along the Navajo Sandstone/Carmel Formation contact. Fracture density data acquired from scan-line measurements shows that fracture density is highest in fracture clusters, in the syncline hinge where curvature is highest, and near faults. Fracture swarms also are concentrated in regions at sites where the along-strike curvature of the fold exhibits the most rapid variation. The fracture distributions are related to the structural settings in which transmissive fractures have predictable orientations.

We also examined interface features between the Mount Simon Sandstone and overlying Eau Claire Formation. The Mount Simon Sandstone is being evaluated as a

possible long-term carbon storage reservoir unit, with the Eau Claire Formation as the caprock. We did not observe interface features such as those noted at the Utah study sites in core and outcrop of the interface. We did, however, observe gypsum filled fractures in the Mount Simon core. Previous workers have described deformation bands in some Mount Simon core from the Illinois basin, so it is possible that interface features similar to those described in our outcrop analogues exist. Although not directly related to our interface study, petrographic and petrophysical analysis of samples of Mount Simon Sandstone and Eau Claire Formation core indicate that the porosity networks in the Mount Simon are unusually heterogeneous. This is a potentially beneficial attribute, since such heterogeneity will promote residual trapping of supercritical CO_2, thus enhancing the likelihood of successful long-term storage.

REPORT DETAILS

A. Introduction

A critical challenge for the core R&D focus area of geological sequestration of CO_2 is in developing well-designed containment systems that have effective seals or caprocks capable of preventing upward migration of CO_2 for 100's to 1000's of years. Principal scientific and technical challenges include predicting likely effectiveness and constraining uncertainties associated with a caprock's ability to impede upward migration of CO_2. This is especially important with regard to storage in saline formations, as little subsurface information may be available. Previous work in the arena of geologic sequestration of CO_2 has focused on investigating reservoir rock properties, quality of potential caprock, and on caprock matrix permeability in attempts to determine the nature of fracture networks within the caprock.

One aspect of the reservoir-seal system that has received little attention is the nature of the reservoir-seal interface. Typically a sedimentological contact, the interface (contact) between reservoir and seal is usually assumed to be discrete (sharp), with simple flow conditions. It is often assumed to be a no-flow boundary in numerical simulations. However, mesoscale characteristics of the interface, such as localized cementation and deformation features, have the potential to significantly influence the degree of fluid connectivity between reservoir and seal.

The character of the reservoir/seal interface is fundamentally controlled by stratigraphic, structural, and diagenetic processes that have affected the contact region between the reservoir and the seal (Fig. 1). Stratigraphic aspects of the interface include whether or not the contact is sharp (an abrupt change in grain size and bedding thickness), gradational (gradual change in grain size, porosity, permeability), or erosional (strata removed by a period of erosion). These characteristics are controlled by the depositional history of the strata, and if conformable, often reflect the lateral migration of environments of differing energy during deposition (i.e., Walther's Law). Structural

aspects result from a modification of the original stratigraphically controlled interface by deformation processes, such as faulting, folding and fracturing. Diagenetically modified interfaces result from post-depositional processes such as cementation. The primary stratigraphic character of such interfaces is typically described in fieldwork performed by sedimentologists, and recorded in stratigraphic sections and field photographs. However, structural and diagenetic features, such as fractures and zones of preferential cementation (Fig. 2), are usually overlooked, and few studies have described such features.

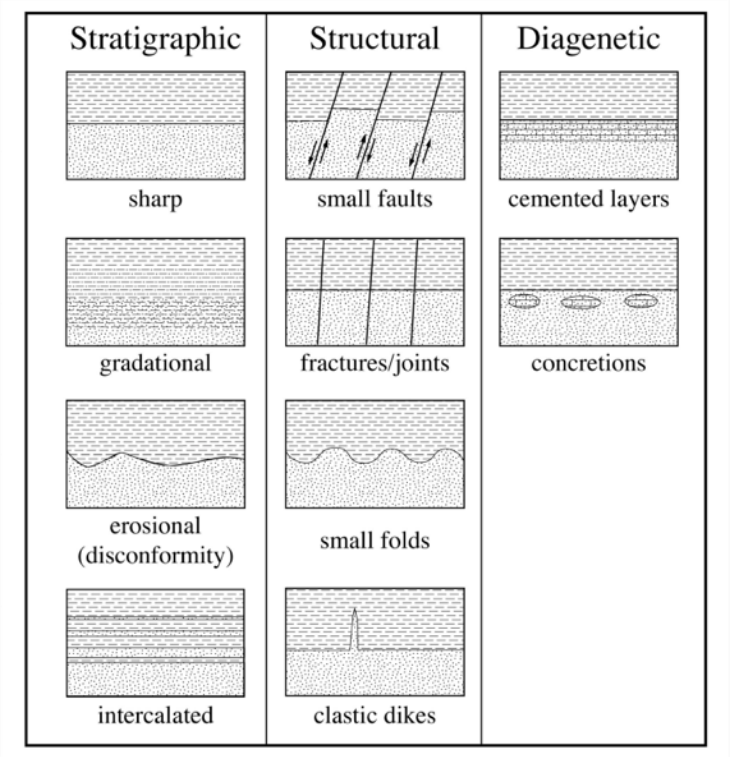

Figure 1. Examples of possible reservoir/caprock interfaces resulting from stratigraphic, structural, and diagenetic processes.

Although not frequently discussed in the literature, sandstone/mudrock interfaces are commonly modified by diagenetic process, particularly preferential cementation by carbonates and other minerals (Fig. 2). Preferential cementation typically occurs mainly within the reservoir lithology near the contact with the mudrock (Fothergill, 1955; Moraes and Surdam 1993; Klein et al., 1999; Hall et al., 2004), but also occurs in the mudrock near the interface. The cementation can either be located in discontinuous pods or present as cemented layers that can extend for kilometers (Klein et al., 1999). A variety of explanations have been proposed for preferential carbonate cementation associated with such interfaces, including elevated carbonate alkalinity in the sand adjacent to the mud due to microbial degradation of organic matter present in the mud, cation exchange of H^+ for K^+ at clay mineral surfaces resulting in locally elevated pH, and cation exchange reactions with Ca-smectite (Boles and Johnson, 1984; Birkeland,

1984; Hall et al., 2004). Preferential cementation at sandstone/mudrock interfaces has also been related to changes in the rate of deposition. For example, laterally extensive cemented zones in the Blackhawk Formation (Book Cliffs, Utah) and Prairie Canyon Member of the Mancos Shale occur preferentially in sandstones at the top of coarsening upwards parasequences. The mudrock immediately above the top of the parasequence was deposited much more slowly than the underlying sandstone, allowing more time for cementation processes occurring near the sediment-water interface to occur (Taylor et al., 1995, 2000; Klein et al., 1999). Complex S- or U-related mineralization is also commonly observed in sandstone –mudrock interfaces on the Colorado Plateau in Utah and the mineralized zones may be 10's m thick. Cementation can influence rock petrophysical properties, filling void spaces and reducing storage capacity and permeability. In many cases cements fill all available pore space, forming a nearly impermeable barrier to fluid flow. Cementation also increases the shear strength of the sediment, which can result in more brittle behavior of the cemented zones, reduced compaction, and elevated seismic velocities.

Figure 2. Outcrop photograph showing strong preferential cementation at a conglomerate/ mudrock interface in the Santa Fe Group, NM. Such preferential cementation is also observed where underlying sands and conglomerates contact overlying mudrocks, however these contact are usually covered by a debris apron produced by preferential weathering of the mudrock.

Structural modification of reservoir-seal interfaces is common at the mesoscale, even in very slightly deformed regions. In the case of many potential sequestration sites in the western US, four-way structural closure with a top seal-reservoir contact that may dip 0-25° is likely, and in such cases, the contact will very likely be deformed. Examples of this deformation include small-displacement faults, which, although too small to show up on geologic maps, or in most geophysical investigations, commonly cut the interface, and may exhibit a change in character (hydrologic and mechanical) from the underlying

rocks to the finer-grained seals. Of particular interest is the character of any fractures in the seal as they approach the interface. In some cases fractures may be well developed in the stiffer, more brittle reservoir rock, whereas fractures may terminate at contacts with mudrocks. This is typically interpreted to be due to the higher fracture toughness of thin bedded, fine-grained rocks. However, we also often observe large, through-going fracture swarms that can create fracture connections between reservoirs and seals. This behavior can be observed in outcrop, and has been inferred in gas-bearing systems on the basis of geochemical analyses of the gas in upper portions of reservoirs. Large-scale (100's m long, 10's m high) fracture swarms also are observed to cut across interfaces, but the controls on the nature of propagation of the fracture systems are poorly known and there are few constraints that we can place on hydro-mechanical models of pressurized fluids in the reservoir (see for example, Olson et al. 1993). Leakage through fracture networks (including sub-seismic faults) can be a dominant leakage mechanism, either through existing open networks (Ingram and Urai, 1999; Hegland, 2005; Rutqvist et al., 2008), reactivation of preferably oriented fracture systems (Reynolds et al., 2005), or inducing new fracture systems through hydro- or gas- driven fracturing (Caillet, 1993; Hawkes et al., 2004). Fracture systems are significant hydraulic conductors or barriers, and in either case dominate fluid flow behavior in some rock types (National Research Council, 1996).

Modeling the upward transmission of CO_2 from subsurface sequestration sites is a critical component of predicting containment system effectiveness for 10's to 100's of years. The principal objective of our research is to determine the influence of diagenetic and structural features of the reservoir/caprock interface on transmission of CO_2 into and through the caprock. Our approach to addressing this issue was as follows: (1) Initial field reconnaissance to inventory common structural an diagenetic features of outcrop analogues of reservoir/caprock interfaces; (2) detailed geologic and petrophysical description of selected interfaces in outcrop; (3) using the outcrop data as a basis, creation of conceptual permeability models of the described interfaces; (4) single and multiphase flow modeling using the conceptual permeability models as a framework, in order to quantitatively assess the impact of such features on subsurface fluid moment; and (5) collection of regional structural data on outcrop analogues to determine geologic controls on the spatial distribution of the investigated features. In addition to this outcrop based work, we also examined core that cuts the reservoir/caprock interface of a system that is actively be used for carbon storage as part of a DOE funded pilot project.

The majority of the findings of our study are detailed in three MS theses. Raduaha (2013) focused on the geology and conceptual permeability models of the detailed study sites, Butler (2014) the results of our numerical modeling efforts, and Flores (2014) the relationship of the interface features to the larger structural setting of the eastern limb of the San Rafael Swell. In addition, several current MS students continue to pursue aspects of this study. In this report we present key data and results

collected during the course of the project. Detailed methods, as well as additional data and interpretations can be found in the theses.

B. Methods

Field Reconnaissance

During the reconnaissance stage of the study we examined outcrop analogues of reservoir/caprock interfaces in New Mexico and Utah. Most of our work ultimately focused on beautifully exposed contact between the Navajo Sandstone (reservoir) and Carmel Formation (caprock), and the Slickrock Member (reservoir) and Earthy Member (caprock) or the Entrada Formation in Utah. We focused on these outcrops because of their near continuous exposure and the well defined (abrupt) nature of the contact. After inventorying relevant structural and diagenetic features we decided to focus on interface features resulting from the intersection of deformation bands and deformation band faults in the reservoir lithology with the caprock.

Description of Detailed Study Sites

Upon selection of a study site the sedimentary and structural features were mapped and sampled for lab analysis. Maps showing the spatial relationships among the various features were made on photomosaics of each site. Stratigraphic sections were measured at each of the main study areas to determine unit thicknesses and produce stratigraphic columns. This data was used to produce conceptual geologic models of the sites. Key data recorded includes lithofacies and the geometry of structural elements, such as fractures and deformation bands. These models were modified to create permeability models using minipermeameter, fracture aperture, laboratory and literature data. We collected data from seven detailed study sites in two principal areas; one located along the Navajo/Carmel contact, the other along the Slickrock/Earth contact (Fig. 3).

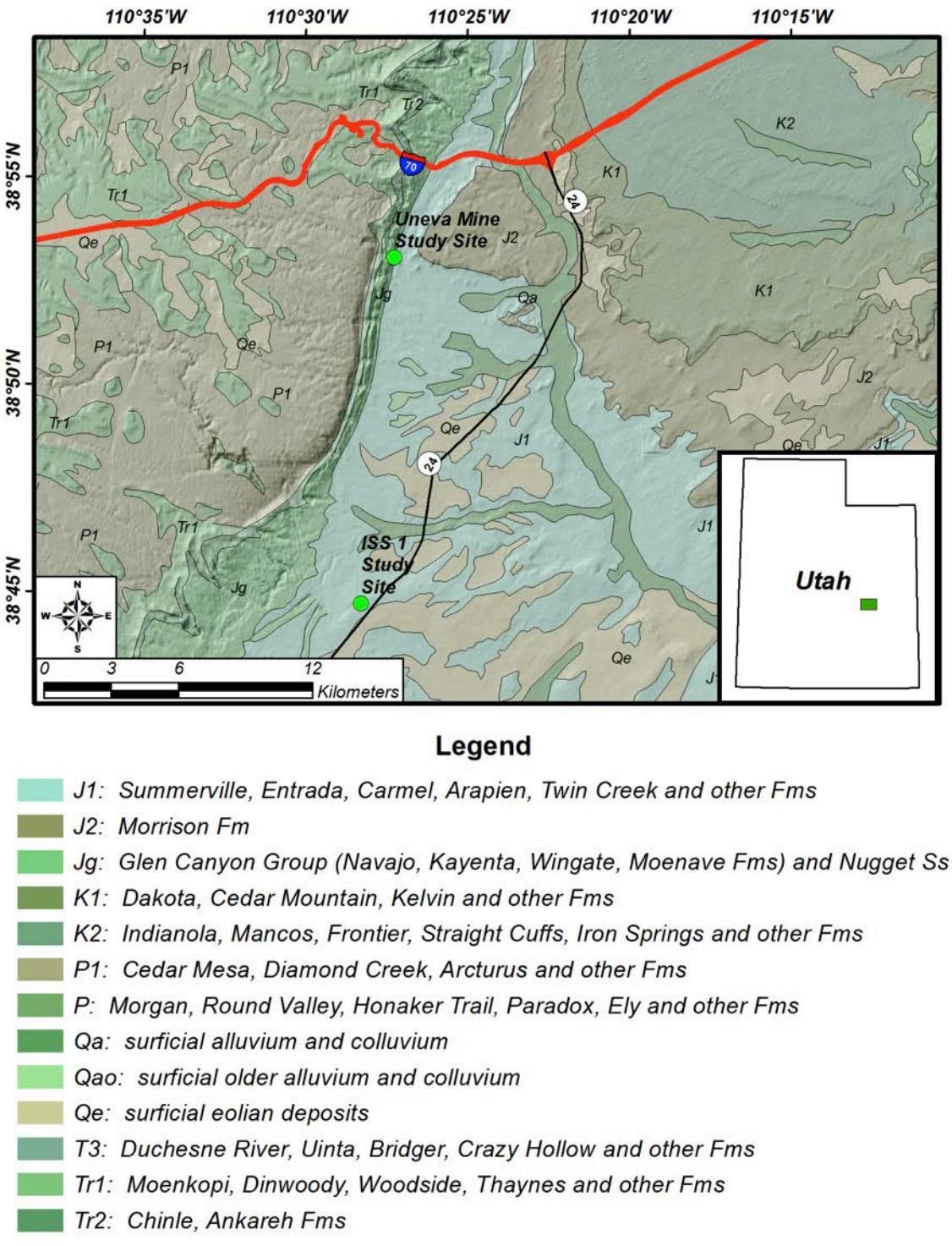

Figure 3. A general site overview map, including the surface geology and major roads in the area. The principal study sites are marked with green dots. A total of seven sites were described within these two areas. (Geologic data from Hintze et al., 2000)

Petrophysical data collected for the outcrops included air permeability and mercury injection capillary pressure (MICP) data. The permeability of the different

lithologies was measured using a New England Research, Inc TinyPerm II Portable Air Permeameter. This device has an operating range from approximately 10 millidarcys to 10 darcys (TinyPerm II Portable Air Permeameter User's Manual, New England Research, Inc). MICP analysis involves injecting mercury into a plug while measuring the pressure necessary to do so. This provides data on pore-throat size distribution and porosity. This analysis was carried out on zones of deformation bands, allowing for the calculation of the permeability and breakthrough pressure of a non-wetting phase. The latter is necessary in calculating the maximum column of CO_2, oil, or gas zones of deformation bands can contain. Samples were cut into plugs that were no larger than 0.75 inches in diameter and 0.75 inches thick. The plugs were then sent to Poro-Technology where they were jacketed with epoxy and underwent MICP analysis.

In order to understand the evolution of porosity and permeability in the outcrop analogue sites we examined the petrography and diagenetic history of the sites using a variety of techniques. Selected samples were cut into billets using a diamond coated rock saw and sent to Wagner Petrographic © to make 24x46 mm thin sections. Two types of thin sections were prepared, standard thin sections meant for only optical analysis and polished thin sections meant for both optical and microprobe analysis. All thin sections were impregnated with epoxy containing a red Rhodamine dye to allow differentiation of real porosity from apparent porosity produced during thin-section preparation. Optical petrography was performed on a standard petrographic microscope equipped with a digital camera. Photomicrographs were used to document mineralogy and textural properties. The modal abundance of constituents was determined for siliciclastic samples using a 300-point count. An additional 100-point (pores only) count was also performed to document the types of porosity present. For samples that do not contain abundant porosity, the types of porosity were estimated visually. Point counting was not performed on limestones, samples that were too small (< 2 cm^2), or samples of poor thin-section quality (thin sections made from billets damaged during transport). Polished thin sections were analyzed using a CAMECA ® SX-100 electron microprobe equipped with back-scattered and secondary electron detectors, and three WDS spectrometers for quantitative chemical analysis. Prior to analysis, each polished thin section was coated with carbon. Because results of the quantitative analysis of carbonate cements are given in Wt% oxide recalculated as carbonate, the data were converted to mol% using dimensional analysis and then normalized to 100%. Wt% oxide totals were used to exclude bad data; specifically, carbonate analyses differing more than 2% from a sum of 100% were considered inaccurate and not reported. All quantitative analyses were performed using a 15 kV beam. The beam diameter used for the majority of the analyses was 20 μm, although a beam diameter of 10 μm was used on some locations too small for 20 μm. Iron oxide cement was analyzed using a PANalytical X'Pert PRO X-ray diffractometer. Heavily iron oxide cemented whole rock and fracture-fill samples were ground to a fine powder using a mortar and pestle. The powder was analyzed on the X-

ray diffractometer from 6 to 70 °2θ. Mineral peaks were identified using X'Pert High Score plus. Stable isotope (oxygen and carbon) analysis of fracture-filling calcite was performed using a Thermo Finnigan Delta Plus XP mass spectrometer. Analysis was performed under continuous flow conditions with a helium carrier gas. The samples were first extracted from the veins using a Dremel® Tool with ~1 mm drill bit. Roughly 0.25 mg of the sample was then weighed and placed in a small vial. The vials were closed with a cap and septum to prevent leakage. Next each vial was injected with helium gas for two minutes; this was done using a specifically designed needle that contains one hole for injecting helium and another for removing air. Ten drops of phosphoric acid was then placed inside each the vial. Next the vials were put into a heating block and given time to equilibrate to 50º C. Once at 50º C, each sample was run ten times on the mass spectrometer. Standards were run to check for accuracy and to correct the raw data. CO_2 lab standards (blanks) were run every five samples to check for accuracy and machine drift during the sample run. Duplicate samples were run to check for variability in isotopic signatures among veins. The $\delta^{18}O$ of the duplicates were within 0.03 to 2.11‰ of each other, while the $\delta^{13}C$ were within 0.36 to 1.79‰ of each other. All duplicate samples were averaged. Calcite from the same vein but from a slightly different location were also run to check for isotopic variability. The $\delta^{18}O$ of calcite from the same vein but from a slightly different location were within 0.45 to 0.54‰ of each other, while the $\delta^{13}C$ were within 0.31 to 1.48‰ of each other.

Regional Mapping and Description of Structural Features

We used Google Earth®, previous analyses of the area from Barton (2011), and on-the-ground reconnaissance to determine field site locations in various structural settings along the east flank of the San Rafael Swell with the appropriate stratigraphic exposures. Reconnaissance sites were chosen where the two units are identified at structural positions of interest.

Scan line surveys ranging from 5 m to 12 m long were used to describe fracture properties at outcrop. Fracture mineralization, alteration, and orientation were recorded for each fracture with a height of more than 10 cm. Scan line surveys in the Carmel Formation were conducted on a purple fossiliferous limestone marker bed. The bed is present in the entire field area and has a uniform thickness allowing fracture interpretations to be made based on structural setting without the influence of lithology or bed thickness.

Three-dimensional (3D) outcrop models were created using offset overlapping outcrop images. The models are used for vertical outcrops at which traditional scan line measurements are not possible. Using Sirovision®, 3D photogrammetry software, we created oriented and scaled outcrop models. Fracture spacing and orientation data can be determined from the entire height of the model. Fracture data from each bed can be compared to stratigraphic column data such as lithology and bed thickness.

We used a Schmidt hammer to measure the relative elastic strength of the stratigraphic units in outcrop. The Schmidt hammer values are a measure of the rebound magnitude of a spring-loaded hammer impacting a geologic material (Aydin and Basu, 2005). The relative elastic strength for each unit (Schmidt hammer values of 0-70 units) is compared to lithology and fracture spacing (Petrie et al., 2014) in coordination with a stratigraphic column. Three measurements were recorded for each bed in which Schmidt hammer was used. The greatest range for an individual bed was 15 units, and the average range was 5.5 units.

Fracture orientations were plotted using Open Stereo®, open-source structural analysis software. Great circles are plotted on lower hemisphere equal-area stereonets. Density contours were calculated using the Fisher Distribution counting method. High density contours are used to indicate horizontal least principal stress orientations as fracture orientations are attributed to regional and local stress states. 180° rose diagrams are used to display and compare fracture strike data at each station.

Fracture spacing and fracture density are determined from the scan line data. Fracture spacing is the length between two fractures that intersect the measuring tape and is described by meters per fracture. Fracture density is the inverse of fracture spacing and is described as fractures per meter. The median is used as the primary fracture spacing descriptor because the data has a right-skewed non-normal distribution. Fracture density is calculated by dividing the total number of fractures by the length of the scan line.

The key sedimentary interface is approximated by the top of the Navajo Sandstone or the top of Page Sandstone. The structural contour map of the interface was created in ArcGIS. Surface elevation control points were obtains with a hand-held GPS and Google Earth®. Two borehole logs, API 4301530009 and 4301511183, were obtained from the Utah Department of Oil, Gas, and Mining (DOGM) and serve as subsurface control points. The logs contain spatial data and formation top depths. All of the control points were imported into ArcGIS and used to create a raster image.

Description of Core

As part of a DOE Office of Electricity Project on compressed air energy storage, we obtained excellent core of the Mt. Simon Sandstone - Eau Claire shale/carbonate caprock interface (Fig. 4). We described the core in detail, measured grain size attributes using visual comparators, and measured the orientation of fractures. Petrography and MICP analysis of selected samples followed the same techniques described above for "description of detailed field sites".

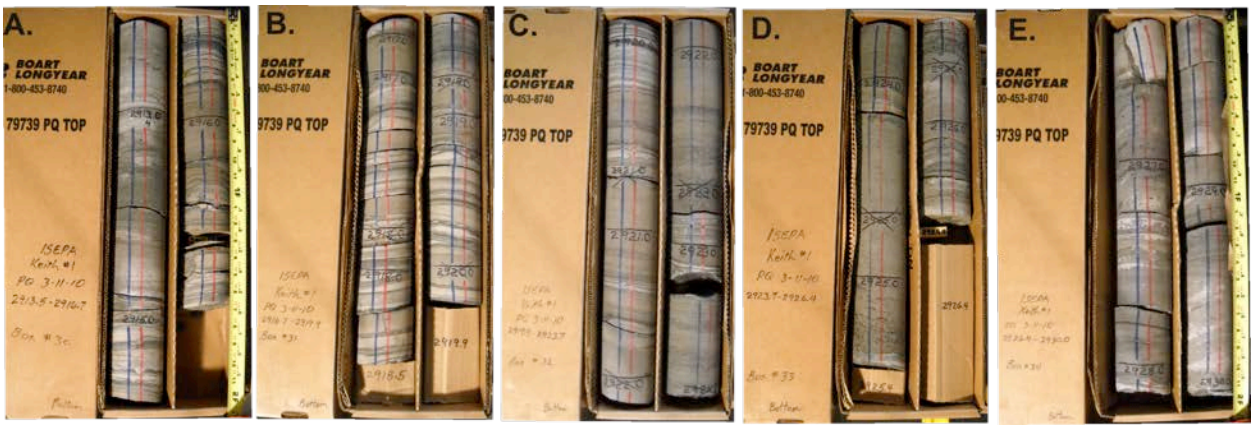

Figure 4. Photograph of core from the Mt. Simon Sandstone, from just below the Mt. Simon – Eau Claire contact at ~2913.5' bgs to 2930.0' bgs.

Numerical Modeling

In order to quantify the effects of fault zone meso-scale features on fluid flow at the study site, a number of numerical flow models were developed and modified. These models were developed for, and run, using two codes: Finite Element Method of Characteristics (FEMOC) a single-phase finite element code (Person et al., 2008) and Finite Element Heat and Mass Transfer (FEHM) a multi-phase finite element code from Los Alamos National Laboratory (LANL) (Zyvoloski, 2007). Utilizing these two codes allowed us to consider both single-phase solute transport (FEMOC) and multi-phase groundwater and supercritical CO_2 transport (FEHM). We chose one of our detailed study sites, ISS-1 as the focus for our small-scale modeling efforts. This site is described in detail in the results section, however, the conceptual permeability model generated based upon the site description work is presented in the methods section.

FEMOC

FEMOC was used to represent single-phase constant-density groundwater flow and brine transport at the reservoir-caprock interface. FEMOC solves the following partial differential equation for groundwater flow.

$$\frac{\partial}{\partial x}\left[\boldsymbol{K}_{xx}\frac{\partial \boldsymbol{h}}{\partial x}\right]+\frac{\partial}{\partial x}\left[\boldsymbol{K}_{xz}\frac{\partial \boldsymbol{h}}{\partial z}\right]+\frac{\partial}{\partial z}\left[\boldsymbol{K}_{zx}\frac{\partial \boldsymbol{h}}{\partial x}\right]+\frac{\partial}{\partial z}\left[\boldsymbol{K}_{zz}\frac{\partial \boldsymbol{h}}{\partial z}\right]=\mathrm{Ss}\frac{\partial \boldsymbol{h}}{\partial t}\quad (Eqn.2)$$

where h is the hydraulic head (m), t is time (s), Ss is specific storage, and K_{xx}, K_{zx}, K_{xz}, and K_{zz} are the components of the hydraulic conductivity tensor (m/s) given by:

$$\boldsymbol{K}_{xx}=\boldsymbol{K}_{max}\cos^2\theta+\boldsymbol{K}_{min}\sin^2\theta\quad (Eqn.3)$$

$$\boldsymbol{K}_{zz}=\boldsymbol{K}_{min}\cos^2\theta+\boldsymbol{K}_{max}\sin^2\theta\quad (Eqn.4)$$

$$\boldsymbol{K}_{xz}=\boldsymbol{K}_{zx}=[K_{max}-K_{min}]\sin\theta\cos\theta\quad (Eqn.5)$$

where θ is the angle between the fault or formation and the x axis, K_{max} is the maximum hydraulic conductivity (m/s) in the direction of the fault plane (or bedding for

sedimentary units), and K_{min} is the minimum hydraulic conductivity (m/s) perpendicular to the fault plane (or bedding for a sedimentary unit).
Groundwater flow rates are calculated using Darcy's Law:

$$\boldsymbol{q}_x = -\boldsymbol{K}_{xx}\frac{\partial \boldsymbol{h}}{\partial x} - \boldsymbol{K}_{xz}\frac{\partial \boldsymbol{h}}{\partial z} \quad (Eqn.6)$$

$$\boldsymbol{q}_z = -\boldsymbol{K}_{zx}\frac{\partial \boldsymbol{h}}{\partial x} - \boldsymbol{K}_{zz}\frac{\partial \boldsymbol{h}}{\partial z} \quad (Eqn.7)$$

where q_x and q_z are the x and z components of the Darcy flux (m/s).
Solute transport is solved in FEMOC using the advection-dispersion equation:

$$\frac{\partial}{\partial x}\left[\phi \boldsymbol{D}_{xx}\frac{\partial \boldsymbol{C}}{\partial x}\right] + \frac{\partial}{\partial x}\left[\phi \boldsymbol{D}_{xz}\frac{\partial \boldsymbol{C}}{\partial z}\right] - \boldsymbol{q}_x\frac{\partial \boldsymbol{C}}{\partial x} + \frac{\partial}{\partial z}\left[\phi \boldsymbol{D}_{zx}\frac{\partial \boldsymbol{C}}{\partial x}\right] + \frac{\partial}{\partial z}\left[\phi \boldsymbol{D}_{zz}\frac{\partial \boldsymbol{C}}{\partial z}\right] - \boldsymbol{q}_z\frac{\partial \boldsymbol{C}}{\partial z} = \phi\frac{\partial \boldsymbol{C}}{\partial t} \quad (Eqn.8)$$

where C is solute concentration (normalized), ϕ is porosity, q_x and q_z are the x and z components of the Darcy flux (m/s), and D_{xx}, D_{zx}, D_{xz}, and D_{zz} are the components of the solute diffusion-dispersion tensor (m^2/s).
The components of the diffusion-dispersion tensor in equation 8 are calculated as follows:

$$\boldsymbol{D}_{xx} = \frac{\boldsymbol{q}_x^2}{|\boldsymbol{q}|}\alpha_L + \frac{\boldsymbol{q}_z^2}{|\boldsymbol{q}|}\alpha_T + \boldsymbol{D}_d \quad (Eqn.9)$$

$$\boldsymbol{D}_{zz} = \frac{\boldsymbol{q}_z^2}{|\boldsymbol{q}|}\alpha_L + \frac{\boldsymbol{q}_x^2}{|\boldsymbol{q}|}\alpha_T + \boldsymbol{D}_d \quad (Eqn.10)$$

$$\boldsymbol{D}_{xz} = \boldsymbol{D}_{zx} = [\alpha_L - \alpha_T]\frac{\boldsymbol{q}_x\boldsymbol{q}_z}{|\boldsymbol{q}|} \quad (Eqn.11)$$

where $|q|$ is the magnitude of Darcy flux ($\boldsymbol{q} = \sqrt{\boldsymbol{q}_x^2 + \boldsymbol{q}_z^2}$) (m/s), α_L is the longitudinal dispersivity (m), and α_T is the transverse dispersivity (m).

FEHM

FEHM was originally developed at LANL to simulate geothermal systems including boiling and phase separation (Zyvoloski, 2007). FEHM was recently modified to include two-phase CO_2 / brine migration (Zyvoloski, 2007). The governing flow equations solved by FEHM is presented in (Zyvoloski et al., 1999).
Darcy's Law for water and CO_2, solved in FEHM are given by:

$$\vec{\boldsymbol{q}}_{H2O} = -\frac{kR_{H2O}}{\mu_{H2O}}\boldsymbol{\nabla}(P_{H2O} - \rho_{H2O}\mathrm{z}) \quad (Eqn.12)$$

$$\vec{\boldsymbol{q}}_{CO2} = -\frac{kR_{CO2}}{\mu_{CO2}}\boldsymbol{\nabla}(P_{CO2} - \rho_{CO2}\mathrm{z}) \quad (Eqn.13)$$

where k is the intrinsic permeability (m^2), R_{H2O} and R_{CO2} are the relative permeabilities, μ_{H2O} and μ_{CO2} are viscosities (Pa·s), P_{H2O} and P_{CO2} the phase pressures (Pa), ρ_{H2O} and ρ_{CO2} the densities (kg/m^3), and z is the gravitational acceleration (m/s^2).
The mass balance equations for water and CO_2 solved in FEHM are given by:

$$\frac{\partial}{\partial t}(\phi\rho_{H2O}S_{H2O}) - \boldsymbol{\nabla}\cdot(D_{mH2O}\boldsymbol{\nabla}P_{H2O}) + \frac{\partial}{\partial z}g(D_{mH2O}\rho_{H2O}) = 0 \quad (Eqn.14)$$

$$\frac{\partial}{\partial t}(\phi\rho_{CO2}S_{CO2}) - \boldsymbol{\nabla}\cdot(D_{mCO2}\boldsymbol{\nabla}P_{CO2}) + \frac{\partial}{\partial z}g(D_{mCO2}\rho_{CO2}) = 0 \quad (Eqn.15)$$

where ϕ is the porosity, S_{H2O} and S_{CO2} are the saturations (volume fraction), ρ_{H2O} and ρ_{CO2} the densities (kg/m^3), D_{mH2O} and D_{mCO2} the mass transmissibilities (s), P_{H2O} and P_{CO2} the pressures (Pa), and g the gravitational acceleration (m/s^2). The mass transmissibilites are analogous to relative hydraulic conductivity, but without gravitational acceleration included.

The mass transmissibilities for equations 14 and 15 are given by:

$$D_{mCO2} = \frac{kR_{CO2}\rho_{CO2}}{\mu_{CO2}} \quad (Eqn.16)$$

$$D_{mH2O} = \frac{kR_{H2O}\rho_{H2O}}{\mu_{H2O}} \quad (Eqn.17)$$

where k is the intrinsic permeability (m^2), R_{H2O} and R_{CO2} are the relative permeabilities, μ_{H2O} and μ_{CO2} are viscosities (Pa·s), and ρ_{H2O} and ρ_{CO2} are the densities (kg/m^3).

Mass conservation requires that the saturation of the two fluid phases sum to one:

$$S_{H2O} + S_{CO2} = 1 \quad (Eqn.18)$$

where S_{H2O} and S_{CO2} are the saturation (volume fraction) of water and CO_2, respectively.

To account for relative permeability effects in the model, we adopted the methodology used by Pruess and Garcia (2002). The relative permeability for water is calculated using the van Genuchten (1980) equation and the relative permeability for CO_2 is calculated using the Corey (1954) equation (Fig. 5a). These equations are given by:

$$k_{rH2O} = \sqrt{S^*}\left\{1 - \left(1 - [S^*]^{\frac{1}{\lambda}}\right)^{\lambda}\right\}^2 \quad (Eqn.19)$$

$$S^* = \frac{S_{H2O} - S_{H2Or}}{1 - S_{H2Or}} \quad (Eqn.20)$$

$$k_{rCO2} = \left(1 - \hat{S}\right)^2\left(1 - \hat{S}^2\right) \quad (Eqn.21)$$

$$\hat{S} = \frac{(S_{H2O} - S_{H2Or})}{(1 - S_{H2Or} - S_{CO2r})} \quad (Eqn.22)$$

where λ is an empirical coefficient, S_{H2O} the water saturation (volume fraction), S_{H2Or} the irreducible water saturation (volume fraction), and S_{CO2r} the irreducible CO_2 saturation (volume fraction).

The capillary pressure-saturation equation is the van Genuchten (1980) equation (Fig. 5b) and is given by:

$$P_{cap} = -P_0\left([S^*]^{-\frac{1}{\lambda}} - 1\right)^{1-\lambda} \quad (Eqn.23)$$

where P_0 is the strength coefficient (Pa), S^* is given by Equation 20, and λ is an empirical coefficient.

Capillary pressure is related to water pressure and CO_2 pressure by:

$$P_{CO2} = P_{H2O} + P_{cap} \quad (Eqn. 24)$$

where P_{CO2} is the pressure of CO_2 (Pa) and P_{H2O} is the pressure of water (Pa).
The calculation of the critical pressure at which the rock will fail was calculated in this study using the failure criteria proposed by (Nicholson and Wesson, 1990):

$$P_{crit} = \frac{\sigma_v}{2}(3\alpha - 1) \quad (Eqn. 25)$$

where σ_v is the vertical stress and α is the ratio of the minimum to maximum principal horizontal stress (σ_3/σ_1) (Jaeger and Cook, 1979).

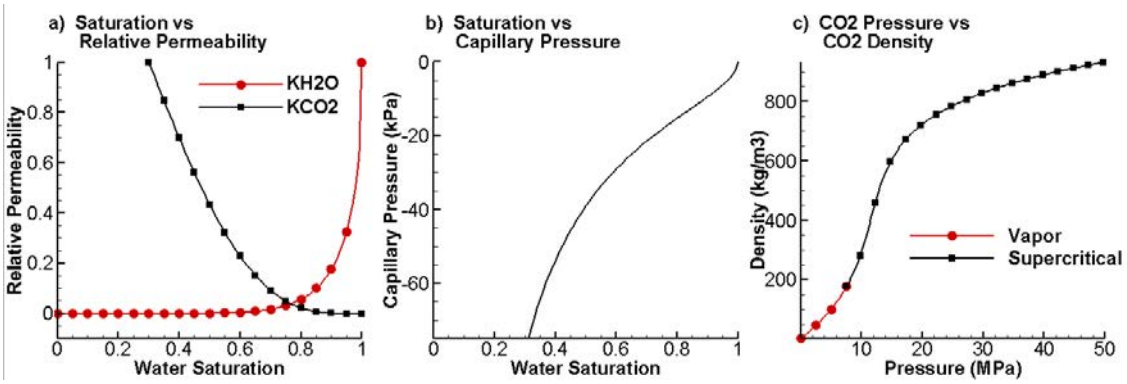

Figure 5. Three figures illustrating multi-phase relationships used in FEHM. a) The saturation plotted against relative permeability for the two phases modeled in FEHM. b) The saturation plotted against capillary pressure. c) The CO_2 pressure plotted against CO_2 density (Span and Wagner, 1996).

Boundary Conditions

The single-phase models represent "far field" conditions, while the multi-phase models represent "near field" conditions (Fig. 6). The single-phase models represent solute transport and flow far (~600 m) from a hypothetical injection well, where supercritical CO_2 is absent and lateral head gradients are small ($\Delta h/\Delta x = 0.05$). The normalized solute species concentration is meant to represent a dissolved solute species, such as HCO_3^- mixed with Ca^{2+}, which may have formed due to the presence of the CO_2 plume lowering the pH and dissolving calcium carbonate cements. However, this model assumes that the solute is behaving as a conservative tracer. The multi-phase models represent supercritical CO_2 transport and flow near (~6 m) to the well, where lateral head gradients are high ($\Delta h/\Delta x = 5$).

The imposed head gradients used in this study are shown in Figure 6. These were calculated with the Theis solution (Theis, 1935) using a permeability of 3.5×10^{-12} m^2 (3500 mD), a reservoir thickness of 2 m, an injection rate of 1.2×10^{-2} m^3/s (200 gpm), a storage coefficient of 1.0×10^{-5}, and a time of 365 days.

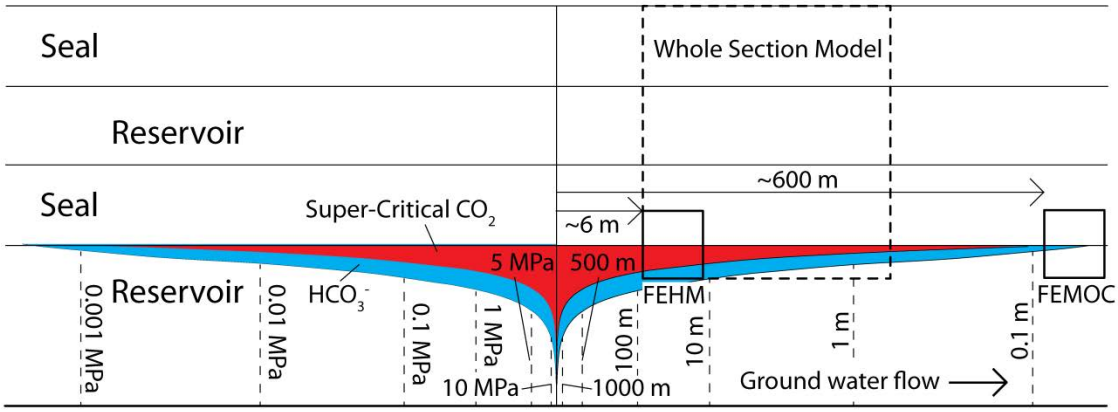

Figure 6. The estimated location/setting of the single- and multi-phase models with respect to an injection well. The red shaded area denotes the region containing super-critical CO_2 while the blue region denotes the region who's groundwater chemistry has been modified by the presence of the supercritical CO_2 plume.

The 5% and 500% head gradients used in this study are more or less consistent with the range of pressure gradients observed at demonstration carbon capture and storage sites around the world. At the Sliepner site in the North Sea, for example, pressure variations over the injection period have been small, from 6.2 MPa to 6.4 MPa (Verdon et al., 2013). Pressure changes at Weyburn, Canada and In Salah, Algeria have been much greater, ranging from 15 MPa to 21 MPa and from 18 MPa to 30 MPa, respectively (Verdon et al., 2013).

The boundary conditions selected for the FEMOC model of ISS 1 (Fig. 7a) were chosen to approximate far-field flow conditions imposed by a CO_2 injection well. A 5% lateral head gradient was imposed across the reservoir portion of the domain; the direction of flow is left-to-right. A 5% lateral hydraulic head gradient is higher than most natural systems, but much lower than head gradients near the injection well, where two-phase flow cannot be neglected. A constant-head boundary was also imposed along the top of the domain, to allow for outflow. The remaining parts of the sides of the model domain (the bottom and seal portion of the sides) were designated as no-flow boundaries. Mathematically, no-flow boundaries are specified as $dh/dx = 0$ for lateral flow (the sides in our model) and $dh/dz=0$ for vertical flow (the bottom in our model). For solute transport, normalized concentration was fixed at 1.0 along the top left edge of the injection reservoir. All other boundaries were no-flux. Mathematically, no-flux boundaries are given as $dC/dx = 0$ (no solute flows across the boundary). The initial normalized solute concentration was set at zero.

The boundary conditions imposed in the FEHM ISS 1 (Fig. 8a) model are analogous to the conditions imposed for the FEMOC ISS 1 model. However, because of the assumed close proximity to the injection well, a lateral 500% head gradient was imposed from left to right in both models. The head gradient was converted to pressures for FEHM. The remaining parts of the sides of the domain (the bottom and seal portion

of the sides) were designated as no-flow boundaries. In addition, CO_2 was introduced directly beneath the caprock at a saturation of 0.2 (volume fraction). All other boundaries, at the sides of the caprock and at the bottom of the domain, were no flux.

In addition to the site scale ISS 1 model, numerical models of the whole stratigraphic section measured in the study area were constructed. These models represents all of the units considered in this study: the Navajo Sandstone, Carmel Formation, Entrada Slick Rock Member, and Entrada Earthy Member. This "Whole Section" model was developed to investigate the effects of more idealized meso-scale features on fluid flow across multiple reservoir-caprock sequences. In the Whole Section model (Fig. 9a), a lateral 500% head gradient was imposed across the lower reservoir, while the upper reservoir was assigned to be hydrostatic. The remaining parts of the domain (the bottom, top, and seal portion of the sides) were designated as no-flow boundaries. CO_2 was introduced into the lower reservoir directly beneath the caprock at a saturation of 0.2 (volume fraction). All other boundaries were no flux.

Numerical Solutions

Equation 2 was solved using the Galerkin finite-element method (Reddy, 1984). The stratigraphic units and fault zones were discretized using triangular elements. The resulting matrix equation was solved using a reduced bandwidth Gaussian elimination scheme.

The solute transport equation was solved using a Lagrangian-based modified method of characteristics (Person et al., 2008). In the modified method of characteristics, particles (Cp) are introduced at each cell. The particle is moved upwind back through the flow field (Huyakorn, 1983). Neighboring nodal concentrations (Cn) are then used to compute the upwind solute concentration. The total derivative is approximated using a finite-difference scheme in time, using the upwind particle concentration (Zheng and Wang, 1999):

$$\frac{Dc}{Dt} \cong \frac{C_n^{k+1} - Cp_n^k}{\Delta t} \quad (Eqn. 26)$$

where Cp_n^k is the upwind particle concentration at the old time level (k) and C_n^{k+1} is the solute concentration at the node at the new time level. FEHM solves equations 12 and 13 using the Newton-Raphson method, an iterative solver, and variable time step size (Zyvoloski, 2007). FEHM uses a variably spaced lookup table to represent CO_2 in all phase states (Zyvoloski, 2007). This table allows FEHM to focus resources in areas where properties change rapidly. This table was derived from the NIST CO_2 pressure and density data (Stauffer, Personal communication, 01/27/14).

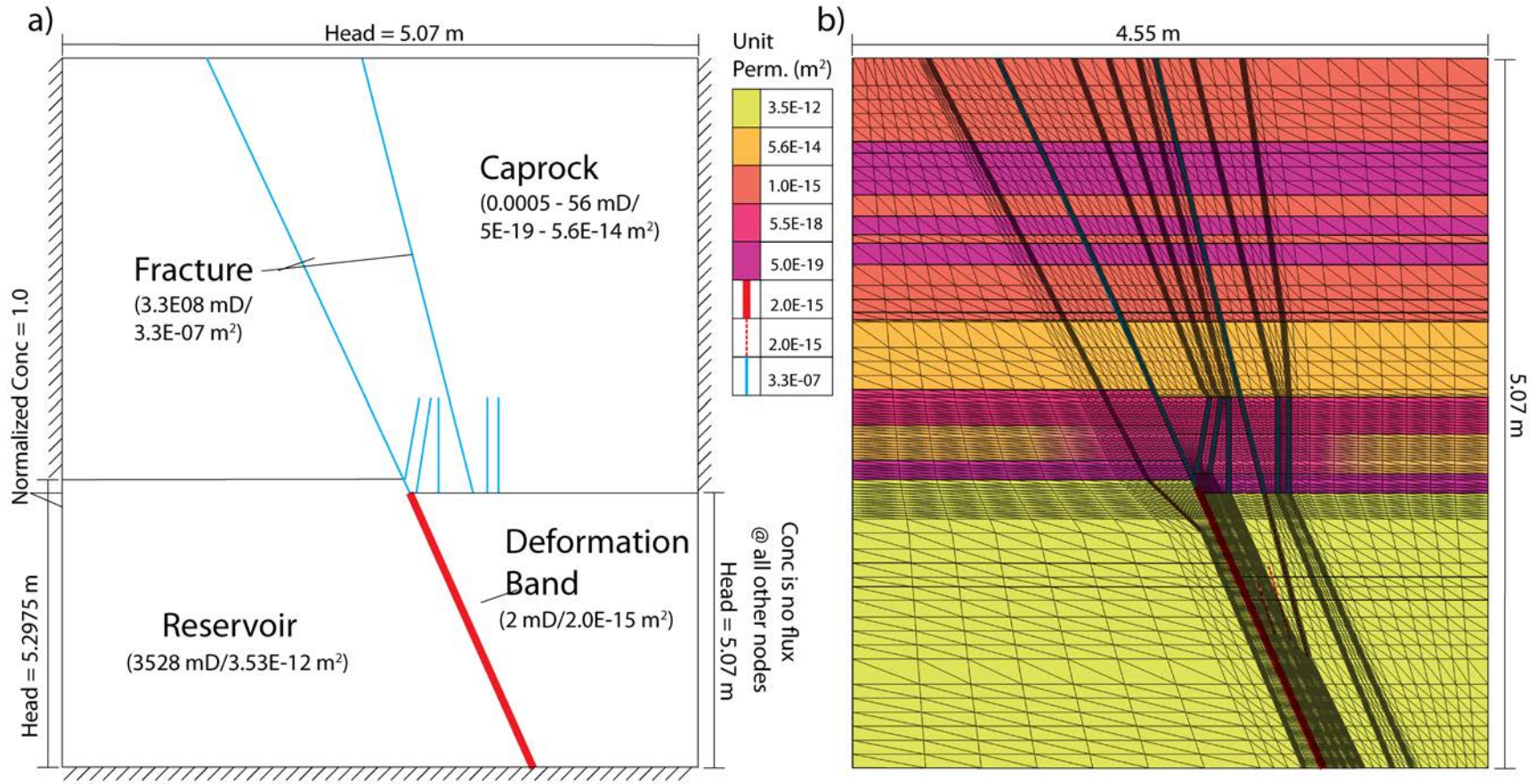

Figure 7. a) A simple conceptualization of the FEMOC ISS 1 model's basic geometry and boundary conditions. The hashmarks along the sides indicate a no-flow/flux boundary. b) The ISS 1 permeability conceptual model, overlain with the mesh created by the MATLAB script.

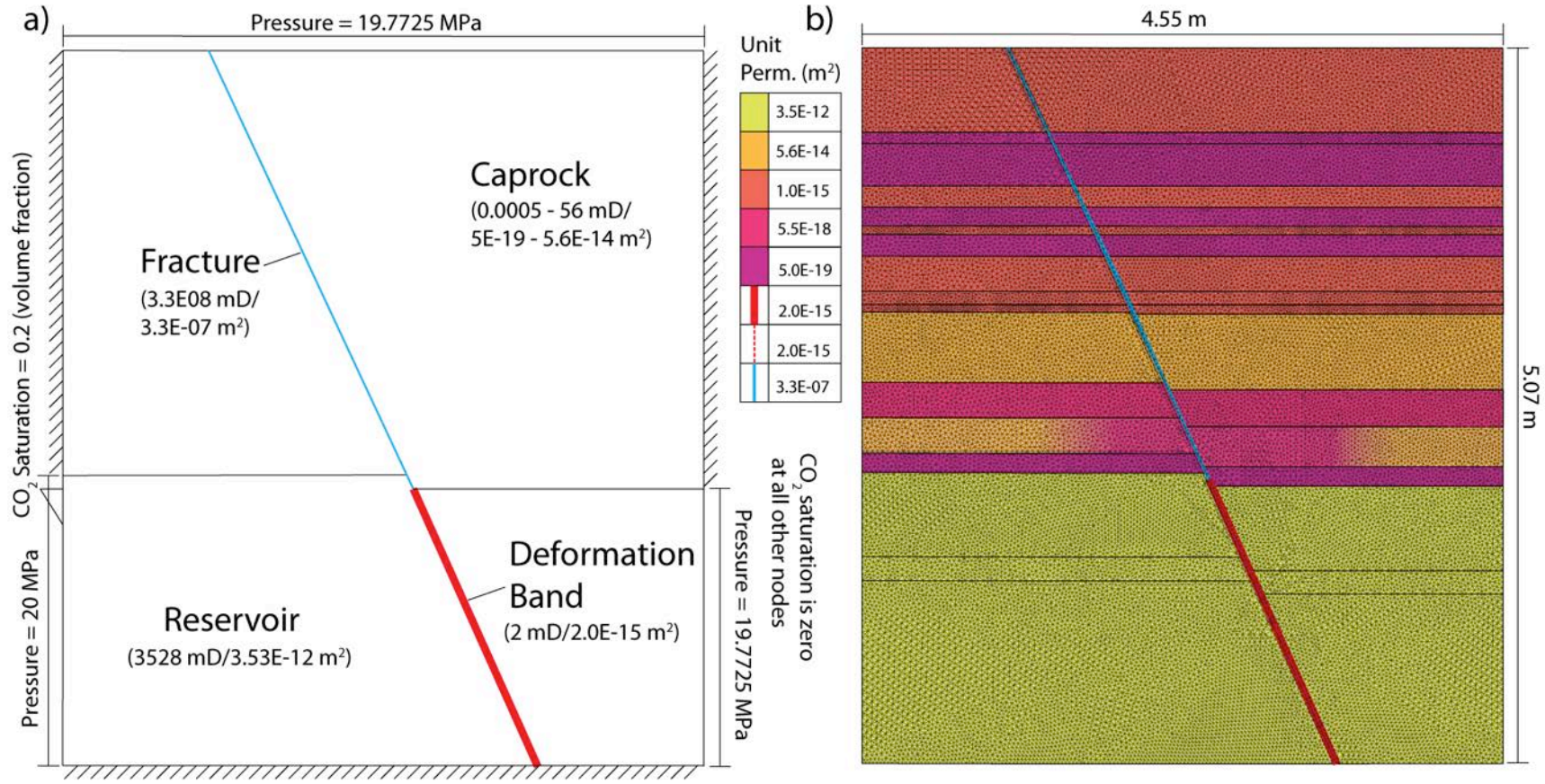

Figure 8. a) A simple conceptualization of the FEHM ISS 1 model's basic geometry and boundary conditions. The hashmarks along the sides indicate a no-flow/flux boundary. b) The ISS 1 permeability conceptual model, overlain with the FEHM Voronoi grid.

Hydrostratigraphic Framework Models and Grid Generation

A hydrostratigraphic framework model of ISS 1 was created that included meso-scale outcrop features (described in Results section). The permeability assigned to different lithostratigraphic units was an average value, based on multiple measurements obtained using TinyPerm II and MICP (Raduha, 2013). The ISS 1 hydrostratigraphic framework and permeability model is shown in Figure 7b. In this model, the lower reservoir unit (yellow) is about 1.3 m thick. All of the layers above it make up the caprock, but were found to be of variable permeability and have been broken into separate hydrostratigraphic units. In total, the thickness of the caprock units is about 3.77 m. The main deformation-band fault (Fig. 7b, solid red line) is about 4 cm thick. The smaller deformation bands (dashed red lines) range from 2 mm to 30 mm thick. The fractures (blue lines) are all about 2 mm thick. At the reservoir-caprock interface there is approximately 12 cm of offset, which tapers to no offset after the fracture penetrates about 1.5 m into the caprock.

The finite-element grid created for FEMOC, from the ISS 1 conceptual model, was a structured triangular grid (overlain on Fig. 7b). The geometry of the lithologic units and faults was digitized from the conceptual model. These points were then input into a MATLAB-based mesh generation program. The elements in this mesh range from about 0.001 m to 0.5 m in width (Δx), from about 0.02 m to 0.2 m in height (Δz), and from about 1:2 to 1:100 in aspect ratio.

FEHM uses control-volume Voronoi elements. Voronoi elements represent the bisector lines formed from a triangular finite-element mesh. All Voronoi elements are created by drawing a normal vector halfway between the vertices of a triangular element. The grid generation software "Los Alamos Grid Toolbox (LaGriT)" (Bower et al., 2005) creates Voronoi elements and was employed in this study. The LaGriT software can generate grids that honor the complex geometries of fault zones and hydrostratigraphic units. We constructed Voronoi grids for the ISS 1 (Fig. 8b) and "Whole Section" (Fig. 9b) hydrostratigraphic framework models.

We conducted a sensitivity study to investigate the impact that these meso-scale features have on flow and transport in the system, by altering properties at the reservoir-caprock interface along the fault offset (the "interface offset") (Fig. 10a-b). We also consider how the degree of fracture penetration into the caprock affects flow (Fig. 10c-d). A 70% caprock penetration was arbitrarily selected to represent partial fracture penetration through a majority of the caprock thickness.

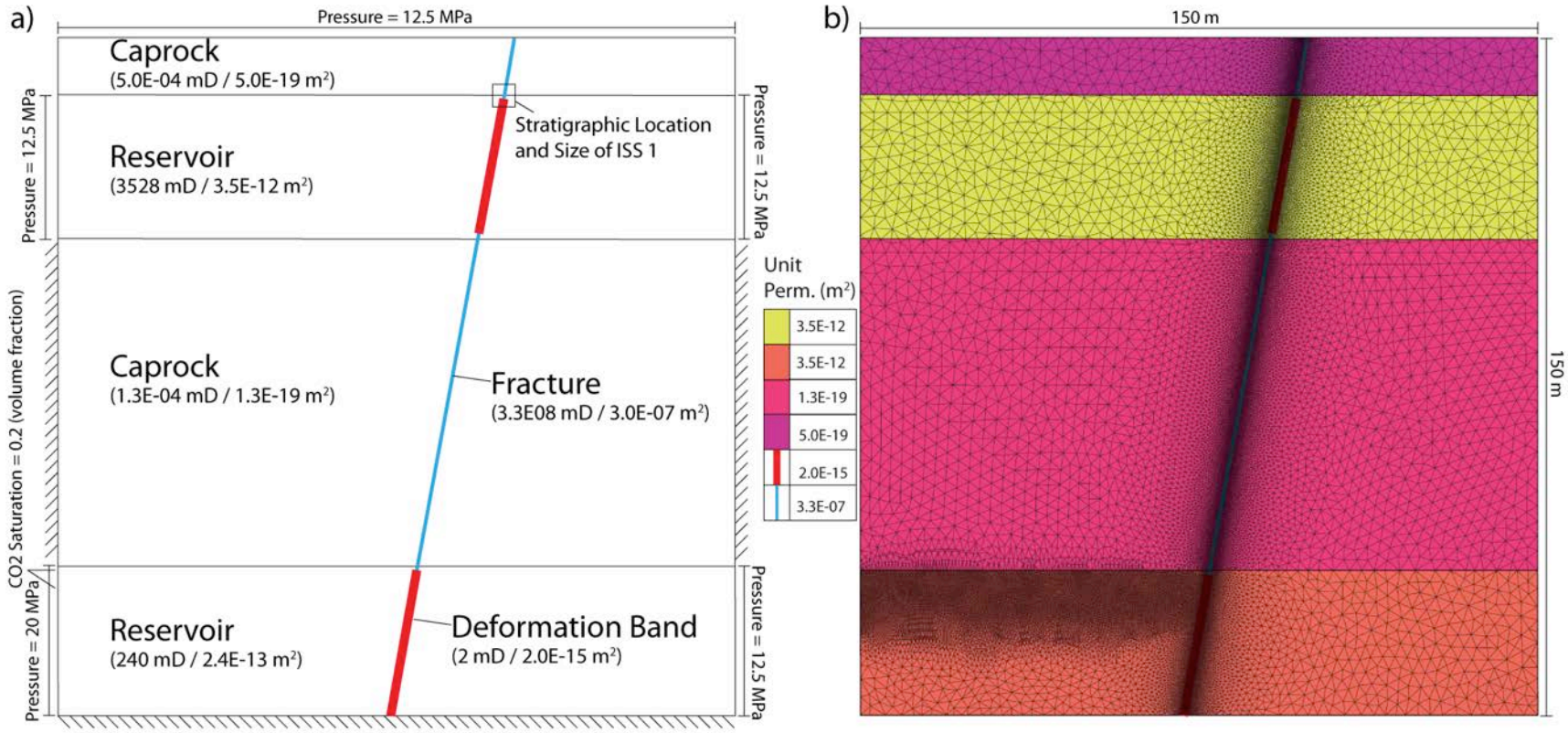

Figure 9. a) A simple conceptual model and boundary conditions for the Whole Section model. The hashmarks along the sides indicate a no-flow/flux boundary. b) The Whole Section permeability conceptual model, overlain with the FEHM Voronoi grid.

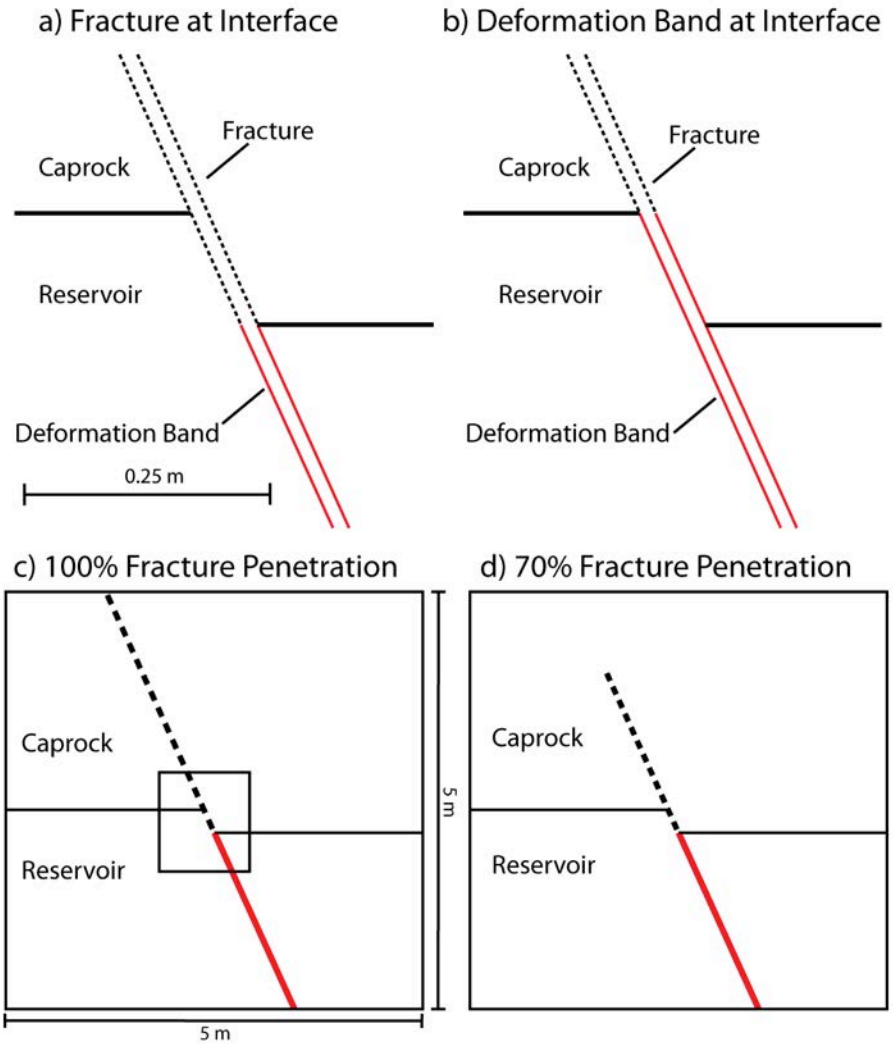

Figure 10. A comparison of the changes in geometry at the interface offset. a) Fracture is at the offset. b) Deformation-band fault is at the offset. c) 100% fracture penetration through the caprock. Inset shows region depicted in a and b. d) 70% fracture penetration through the caprock.

C. Results

Field Reconnaissance

During our initial field reconnaissance we cataloged structural and diagenetic features of outcrop analogues of the reservoir/caprock interface, and formulated hypotheses related to these features. We also formulated hypotheses related to these features, some of which are described below. As noted above, most of this work focused on exceptionally well exposed outcrops of the Navajo Sandstone/Carmel Formation contact, and outcrops of the Slickrock and Earthy Members of the Entrada Formation in Utah. The principal features that we noted during this reconnaissance phase were: (1)

Intrusions of reservoir lithology into caprock lithology that result from soft-sediment deformation (Fig. 11). We hypothesize that such asperities at the reservoir/caprock interface may form areas likely to produce focused flow of reservoir fluids into caprock, and/or zones more prone to hydrofracing. (2) Preferential cementation of reservoir rock adjacent to caprock lithology (Fig. 12). We hypothesize that such cementation may significantly decrease upward migration of CO_2 into the caprock, or if fractured, provided pathways for focused flow into the caprock. (3) Deformation bands, deformation band faults, and joints in the reservoir lithology that transition to fractures and joints in the caprock lithology (Fig. 13). We hypothesize that such faults and fracture systems may provide zones of focused fluid flow from reservoir into caprock. This is supported by patterns of bleaching (hematite dissolution) that document such flow in the past.

Description of detailed study sites

Two main study sites were examined during this project, the Uneva Mine Canyon study site (UMS) and the Iron Wash study site (ISS). Both are located within 20 km of each other (Fig. 3).

Uneva Mine Canyon Study Site (UMS)

Units found at this study site include the Navajo Sandstone and the Carmel Formation. All four members of the Carmel Formation are present at this site, although only the lowermost are described in detail because the reservoir-caprock interface is the main concern of this study. Two detailed study sites were selected for analysis at this location: Uneva Mine Canyon study site #1 (UMS-1) and Uneva Mine Canyon study site #3 (UMS-3). In the interest of brevity, we only report the details of one of the sites here. For information on the second site see Raduha (2013) and Flores (2014).

Navajo Lithofacies

The cross-bedded sandstone lithofacies contains 2.0 to 7.2 m thick beds of tan, medium upper (average) grained, well sorted, calcareous sandstone. Large-scale trough cross-bedding in this lithofacies is consistent with an eolian origin.

The deformed sandstone lithofacies contains 0.6 to 4.7 m thick beds of tan, medium lower (average) grained, moderately-well sorted sandstone. It is characterized by massive and convolute bedding. The massive sandstone beds may have formed from multiple conditions, including bioturbation, deposition of wind-blown sand into still water, post depositional liquefaction, or deposition by mass-flow events (Eschner and Kocurek, 1986).

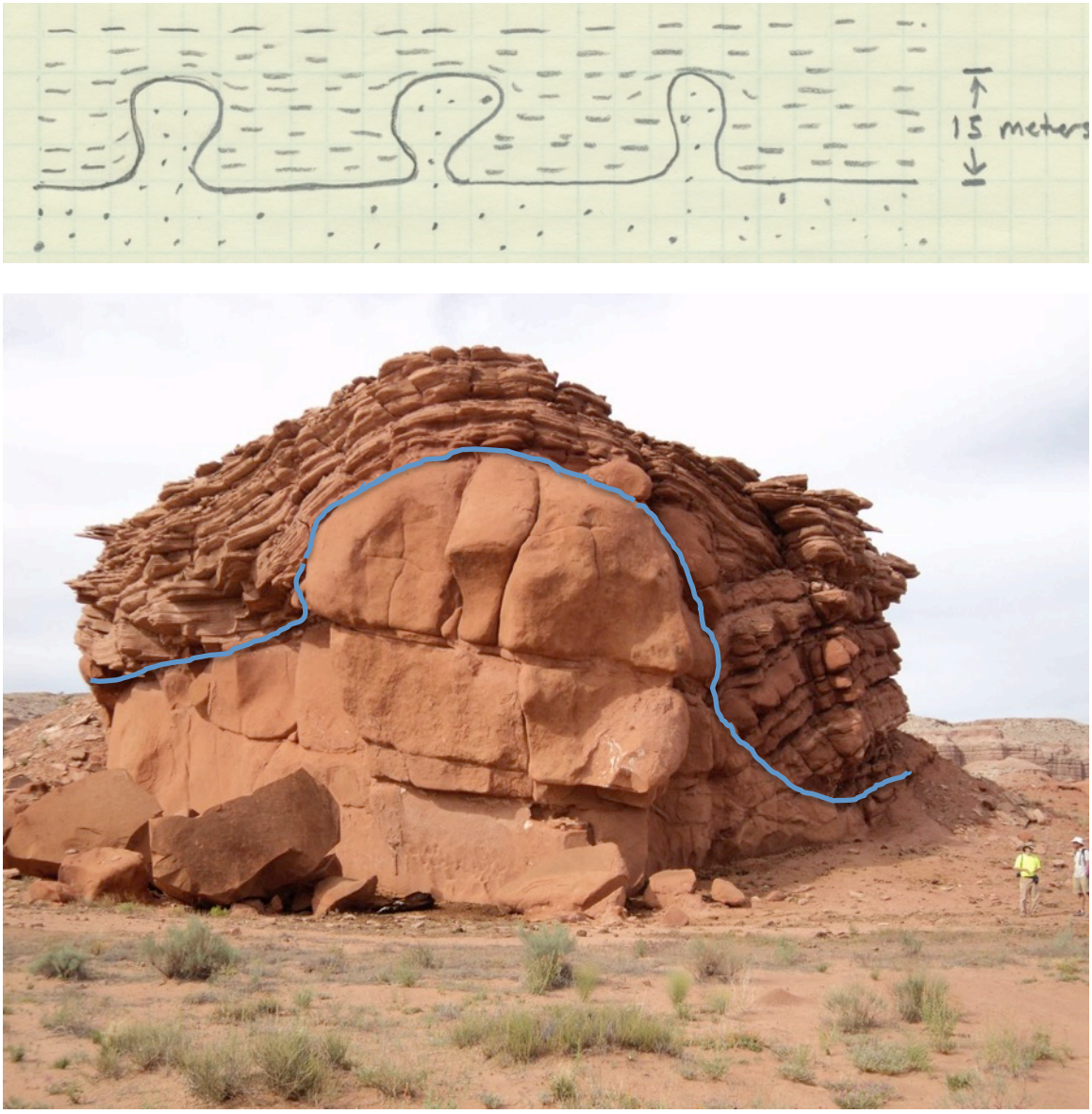

Figure 11. Asperities at reservoir/caprock interface caused by soft sediment intrusion. Large-scale geometry shown in sketch (top) and field example (bottom). Field example shows soft-sediment intrusion present at the contact between the Slickrock Member of the Entrada Formation (sandstone reservoir unit) and the overlying Earthy Member (sandstone/shale caprock unit).

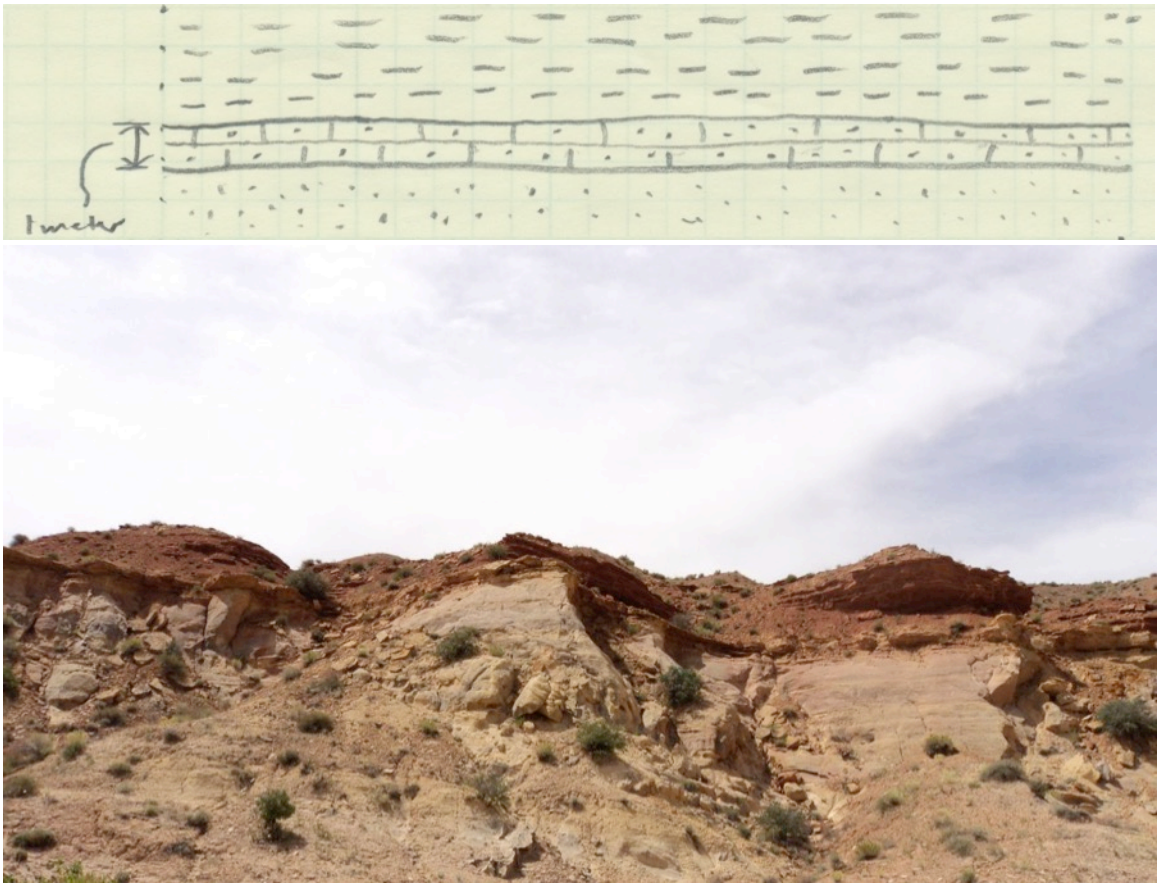

Figure 12. Zone of cemented reservoir rock at caprock/reservoir interface. Sketch illustrating preferential cementation of reservoir unit at interface (top). Field example (bottom) showing zone of cementation (resistant ledge) in the Slickrock Member of the Entrada Formation (reservoir unit) where it is in contact with the Earthy Member of the Entrada Formation (caprock unit).

Co-op Creek Member of the Carmel Formation Lithofacies

The micritic mudstone lithofacies contains 1 to 6.5 m thick beds of tan, sandy, micritic mudstone. Structures include asymmetrical ripple marks, parallel lamination, and cross lamination. Several zones have undergone dolomitization. Given the presence of micrite, this lithofacies likely formed in a low-energy marine environment. This is consistent with the interpretations of the three micritic lithofacies described by Blakey et al. (1983). Blakey et al. (1983) concluded the dolomicrite lithofacies formed along a low-energy carbonate shoreline, the pelmicrite lithofacies was deposited by near-shore marine processes on a protected shelf, and the biomicrite lithofacies formed on a low-energy basin slope.

The oolitic bivalve grainstone lithofacies contains 0.5 to 0.7 m thick beds of maroon oolitic bivalve grainstone. The unit contains abundant stylolites. Given the presence of ooids, this facies likely formed in a high-energy marine environment. Blakey

et al. (1983) interpreted this lithofacies as forming as offshore bars and tidal channel mouth bars along a shelf margin.

The sandstone lithofacies contains 0.2 to 1.3 m thick beds of tan to gray calcareous, silty, fine lower (average) grained, well sorted sandstone. Structures include asymmetrical ripple marks, symmetrical ripple marks, convolute bedding, and load casts. This unit's close proximity to the limestone units suggests a highly variable depositional environment, such as a tidal flat or beach environment. Blakey et al. (1983) interpreted this unit as reworked deposits from the underlying Navajo Sandstone. However, since the unit is present throughout the Co-op Creek Member and not just the base this is probably not the case.

The siltstone lithofacies contains 0.5 to 3.5 m thick beds of tan to red, calcareous, sandy siltstone. Structures include asymmetrical ripple marks, symmetrical ripple marks, parallel lamination, cross lamination, wave ripple lamination, convolute bedding, and load casts. Several zones of the lithofacies have undergone dolomitization. This unit's close proximity to the limestone units and the presence of various ripple structures suggests a low to moderate energy marginal marine depositional environment.

The shale lithofacies contains 0.1 to 2.0 m thick beds of red, calcareous shale. Structures include parallel lamination and sandstone lenses. This unit's close proximity to the limestone units and its parallel lamination likely indicates some sort of low energy marine to marginal marine depositional environment. This is consistent with Blakey et al. (1983) who interpreted the terrigenous mudstone lithofacies was deposited in a low-energy marine environment.

Uneva Mine Canyon Study Site #1 (UMS-1)

This study site is located just south of the entrance to Uneva Mine Canyon (12 S, 547208, 4303956, WGS 84 datum). The site has an excellent exposure of the interface between the Navajo Sandstone and the Carmel Formation (Fig. 13). This site was chosen based on the large amount of bleaching associated with fractures at and above the interface. Almost all of the Carmel Formation is exposed at this study site, except for the upper portion of the Winsor Member.

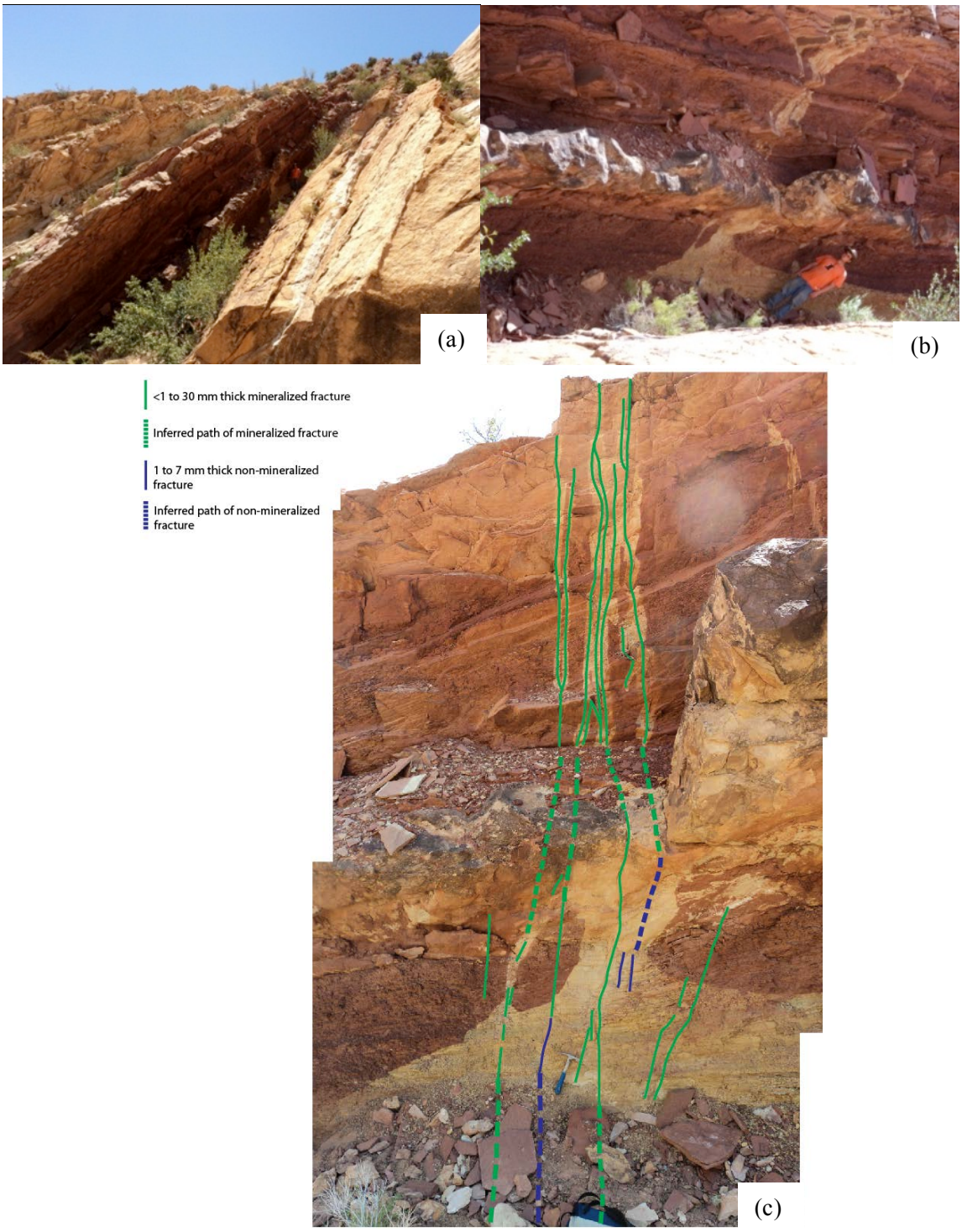

Figure 13. (a) Overview of UMS-1, 6 ft./1.83 m person for scale. On the right side of the image is the Navajo Sandstone, while to the left is the Co-op Creek Member of the Carmel Formation. The person wearing an orange t-shirt marks the location of the reservoir-caprock interface. (b) Overview of the bleached zone, 6 ft./1.83 m person for scale. (c) Bleached fracture network of UMS-1 with annotations, hammer for scale. Fractures cut through the Navajo Sandstone into the Carmel Formation. The bleached fractures make it easy to trace the fracture network.

Structural features of interest at UMS-1 are a set of fractures going from the Navajo Sandstone into the Carmel Formation (Fig. 14). Fractures of the Navajo Sandstone are opening-mode. The majority of the fractures in the Carmel Formation are opening-mode with minor amounts of sliding-mode fractures. Fracture thickness varies from <1 to 30 mm. The fracture network penetrates 17.7 m into the Carmel Formation before it can no longer be traced. Bleaching is associated with most fractures close to the interface, but bleaching is no longer visible on mineralized fractures farther away from the interface. The Navajo Sandstone and the base of the Carmel Formation are bleached, with an increased concentration of bleaching in close proximately to the fracture networks.

The permeability of the deformed sandstone lithofacies of the Navajo Sandstone and the sandstone lithofacies of the Carmel Formation at UMS-1 were assigned values using corrected TinyPerm II field measurements. The permeability of the deformed sandstone lithofacies, the average of three measurements taken at various locations within this lithofacies, is 237 mD (Fig. 15). The permeability of the sandstone lithofacies, based on one measurement, is 7 mD.

The permeability of the micritic mudstone and oolitic bivalve grainstone lithofacies of the Carmel Formation at UMS-1 were both assigned the value of 0.019 mD. This is average of two measurements obtained from Payne (2011) using mercury injection capillary pressure data to calculate the permeability of limestones from the Co-op Creek Member at a study area also located in the San Rafael Swell.

The permeability of the siltstone and shale lithofacies of the Carmel Formation at UMS-1 were both assigned the value of 0.000133 mD. This is the average of two measurements obtained from Payne (2011) using tight rock analysis to determine the permeability of shales and siltstones from the Co-op Creek Member at a study area also located in the San Rafael Swell.

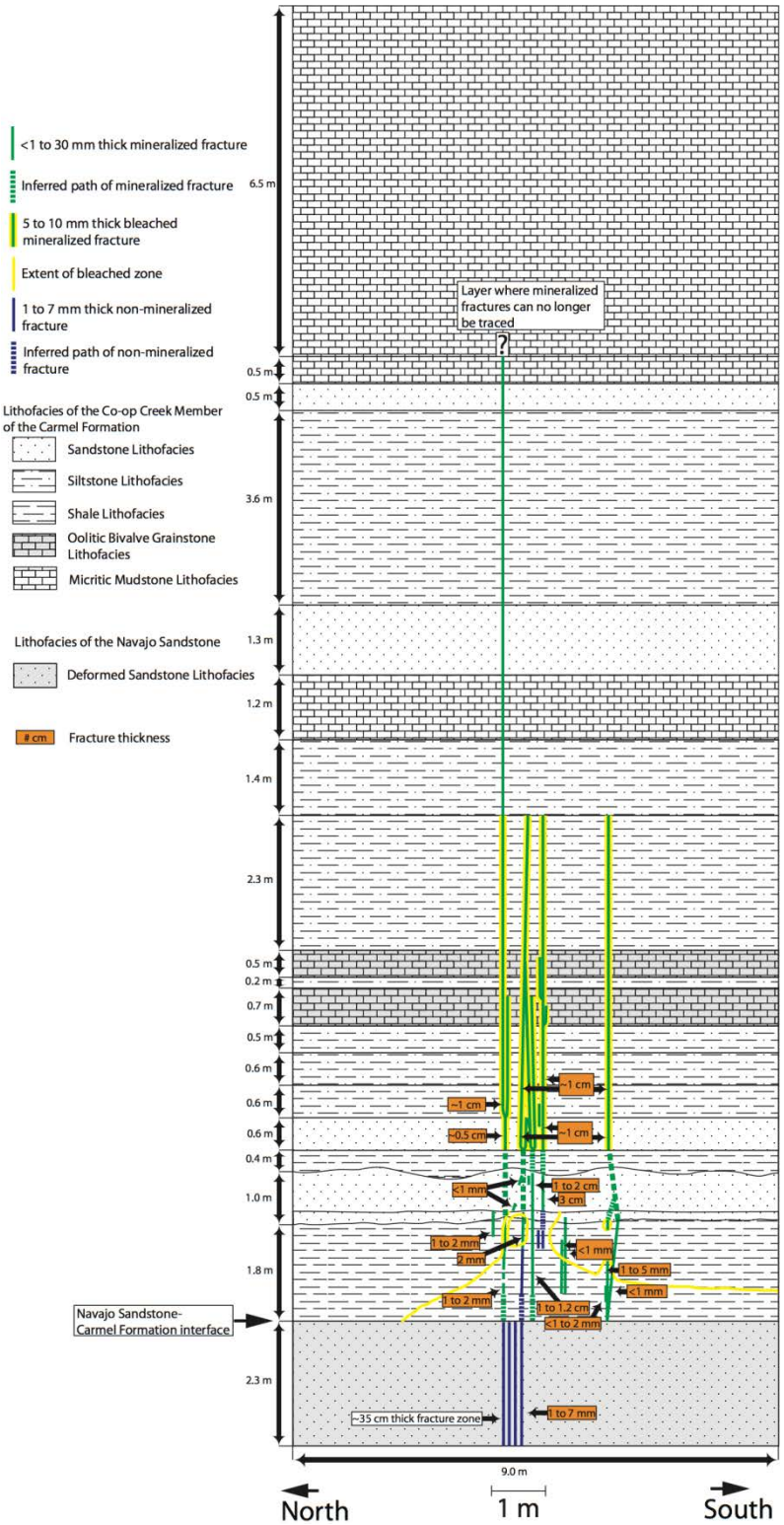

Figure 14. Geologic conceptual model of UMS-1. Fractures cut through the Navajo Sandstone into the Carmel Formation. Bleaching fluids from the Navajo Sandstone used the factures to penetrate the caprock, bleaching the fractures in the process. Fractures penetrate the Carmel Formation for 17.7 m until they can no longer be traced.

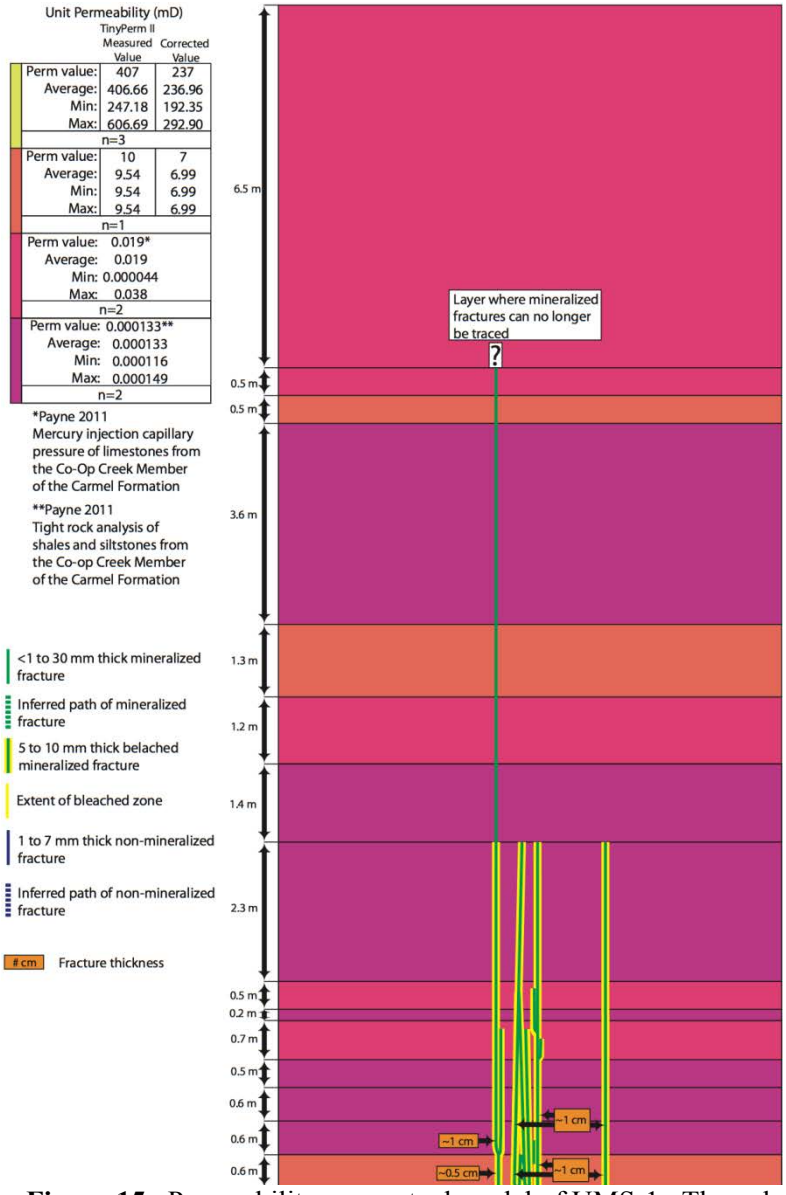

Figure 15. Permeability conceptual model of UMS-1. The color of each lithofacies corresponds to a different permeability, as listed above. Permeability was determined using a combination of TinyPerm II measurements and laboratory permeability measurements from existing authors.

Iron Wash Study Site

This study site is located west of mile marker 146 on Utah State Route 24. Units found at this study site include the Carmel Formation and the Entrada Sandstone. Only the uppermost member of the Carmel Formation is present at this study site. Four detailed study site were selected for analysis at this location: Iron Wash study site #1 (ISS-1), Iron Wash study site #3 (ISS-3), Iron Wash study site #4 (ISS-4), and Iron Wash study site #5 (ISS-5). In the interest of brevity, we only describe one of the sites here. See Raduha (2013) for details on the other sites.

Slick Rock Member of the Entrada Sandstone

Marino (1992) identified nine lithofacies in the Entrada Sandstone in the northern part of the San Rafael Swell. These lithofacies include green mudstone, oolitic sandstone, polydirectional dune sandstone, sigmoidal bundle sandstone, angular and fine-grained sandstone, "stone baby" silty sandstone, red silty mudstone, wavy sandstone, and cross-bedded sandstone. Within the Slick Rock Member the cross-bedded sandstone, wavy sandstone, and red silty mudstone lithofacies are present. To be consistent with the Navajo Sandstone, the wavy sandstone lithofacies shall be known as the deformed sandstone lithofacies.

The cross-bedded sandstone lithofacies contains 0.3 to 8.9 m thick beds of gray to yellow, medium lower (average) grained, moderate to well sorted, calcareous sandstone. Structures include trough and low-angle cross-bedding. The large-scale bedding of this facies likely indicates an eolian origin, as noted by Marino (1992).

The deformed sandstone lithofacies contains 0.2 to 1.5 m thick beds of gray to yellow, medium lower (average) grained, moderately-well sorted sandstone. Structures include massive and convolute bedding. As stated previously with the deformed sandstone lithofacies in the Navajo Sandstone, multiple conditions may be responsible for forming this lithofacies.

The red silty mudstone lithofacies contains 0.1 to 0.3 m thick beds of red shale and siltstone. Structures include parallel lamination. This unit is interbedded with the sandstone beds of the Slick Rock Member. Given this facies is interbedded with eolian sandstone, it likely formed during a wet interdune period.

Earthy Member Lithofacies

The majority of the nine lithofacies described by Marino (1992) for the Entrada Sandstone in the northern part of the San Rafael Swell are present in the Earthy Member. However, for the sake of simplicity I decided to combine several of his lithofacies into three main facies. The first lithofacies known as the sandstone lithofacies consists of the angular and fine-grained sandstone, polydirectional dune sandstone, sigmoidal bundle sandstone, and "stone baby" silty sandstone lithofacies. The second, known as the shale lithofacies consists of the green mudstone and red silty mudstone lithofacies. The third lithofacies, known as the siltstone lithofacies, is a combination of the silty components

associated with the red silty mudstone and "stone baby" silty sandstone lithofacies. The oolitic sandstone lithofacies was not observed at this study site.

The sandstone lithofacies contains 0.1 to 1.4 m thick beds of dark red, fine lower (average) grained, moderately sorted, calcareous, silty sandstone. Structures include convolute, massive, and low-angle cross-bedding. Marino (1992) interpreted eolian, tidal flat, foreshore, and shore face depositional environments for the lithofacies that make up this composite facies.

The siltstone lithofacies contains 0.6 to 4.0 m thick beds of brownish-red, sandy siltstone. Structures include parallel lamination. Marino (1992) interpreted the silty lithofacies formed from a tidal flat depositional environment

The shale lithofacies contains 0.1 to 0.2 m thick beds of red, gray, tan, and green shale with some layers of sandstone. Structures include parallel lamination. The different colored shales may represent different environments, with the greenish shale forming in reducing offshore marine conditions and the reddish shales oxidizing tidal flat conditions (Marino, 1992). Thin sections show that some portions of this lithofacies are litharenites made up of shale fragments and quartz grains (20). Marino (1992) interpreted this as a storm deposit resulting from the mixing of shoreline dunes and offshore mudstones.

Iron Wash Study Site #1 (ISS-1)

The UTM coordinates for the study site are 12 S 0546085, 4288762, WGS 84 datum. The site has an excellent exposure of the interface between the Slick Rock Member of the Entrada Sandstone and the Earthy Member of the Entrada Sandstone (Fig. 16ab). It was chosen because it contains a zone of deformation bands intersecting a reservoir-caprock interface.

Structural features of interest at ISS-1 are zones of deformation bands in the Slick Rock Member transitioning to a set of opening-mode fractures in the Earthy Member (Fig. 17). The main zone of deformation bands is 1 to 5 cm thick, becoming thinner as it approaches the interface. Smaller zones of deformation bands are also present at the interface ranging in thickness from 2 to 30 mm, also becoming thinner as they approach the interface.

The thickness of the Earthy Member fractures varies from <1 to 8 mm. The fracture network can be tracked for 3 m into the Earthy Member before it can no longer be traced due to erosion. Bleaching is associated with some of the fractures close to the interface. The Slick Rock Member and base of the Earthy Member is bleached, with an increased concentration of bleaching in close proximately to the fracture network.

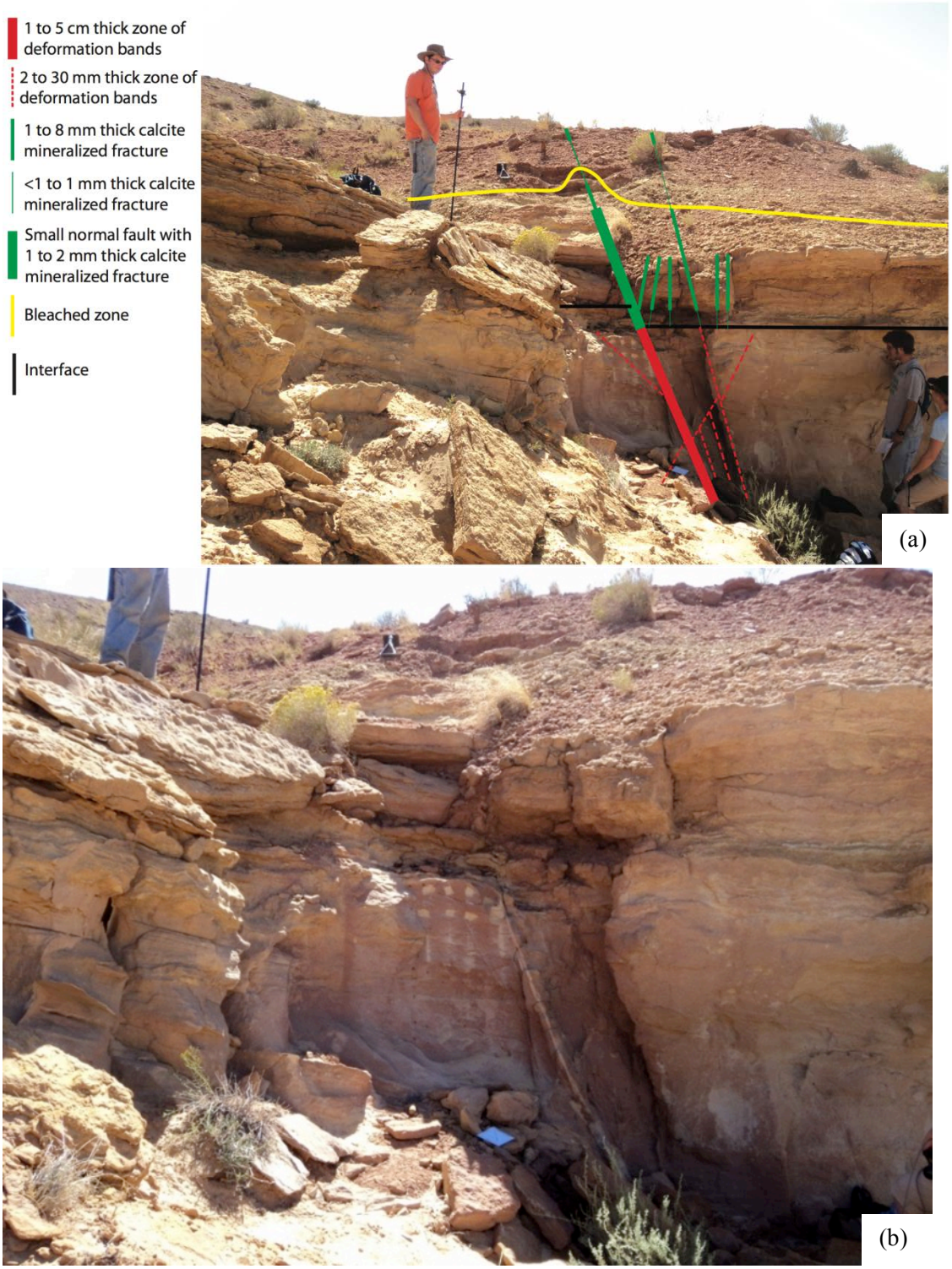

Figure 16. (a) Overview of ISS-1 with annotations, 6 ft./1.83 m person for scale. The black line marks the interface between the Slick Rock Member and Earthy Member. A zone of deformation bands in the Slick Rock Member transitions into a set of fractures in the Earthy Member. The fracture network and the base of the earthy Member is bleached. (b) Enlarged view of ISS-1 zone of deformation bands, 6 ft./1.83 m person for scale.

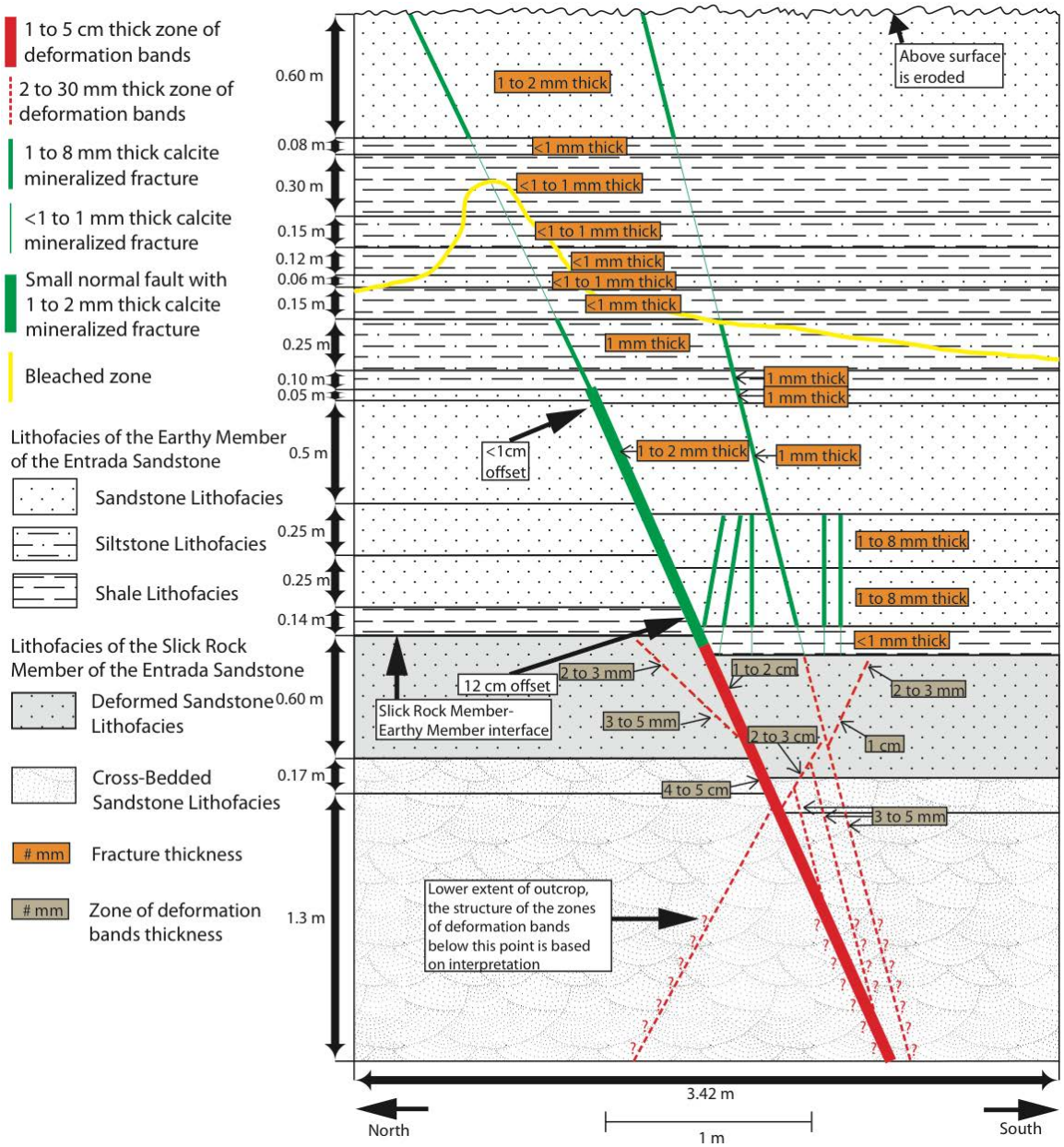

Figure 17. Geologic conceptual model of ISS-1. A zone of deformation bands in the Slick Rock Member transition into a set of fractures in the Earthy Member. Bleaching fluids from the Slick Rock Member used the factures to penetrate into the caprock, bleaching the fractures in the process. Fractures penetrate the Earthy Member for 3 m until they can no longer be traced.

The permeability of the deformed sandstone and the cross-bedded sandstone lithofacies of the Slick Rock Member and the sandstone lithofacies of the Earthy Member at ISS-1 was assigned using corrected TinyPerm II field measurements. The permeability of both the deformed sandstone lithofacies and the cross-bedded sandstone lithofacies, the average of 26 measurements taken at various locations within these lithofacies, is 3,528 mD (Fig. 18). The permeability of the sandstone lithofacies was assigned two different values based on their position. Based on one measurement, the lower sandstone

beds located next to the interface adjacent to the mineralized fractures were assigned the value of 1 mD. Based on the average of 12 measurements at various locations, all other sandstones were assigned the value of 56 mD. Field observations show an increased amount of cementation adjacent to the mineralized fractures in sandstone near the interface, likely contributing to the decrease in permeability at this location.

The permeability of the siltstone and shale lithofacies of the Earthy Member are below the lower measurement limit of TinyPerm II, so they were assigned a permeability of 0.0055 and 0.0005 mD, respectively. These values are the average permeability for siltstones and shales from Brace (1980). These values have a higher permeability than the siltstone and shale samples measured by Payne (2011) in the Carmel Formation using tight rock analysis, which ranged from 0.000116 mD to 0.000267 mD.

The permeability of the main zone of deformation bands at ISS-1 was calculated using mercury porosimetry data. Based on the average of two measurements, when moving parallel to a zone of deformation bands the permeability is 9 mD. Based on the average of two measurements, when moving perpendicular to the zone of deformation bands the permeability is 2 mD. These permeability measurements are consistent with measurements of previous authors working on cataclasis bands in the Entrada Sandstone, which range from 4 to 11 mD (Torabi et al., 2008).

Petrography and Diagenetic History of Caprock Fractures

We characterized the modal composition and diagenetic history of samples from the detailed study sites. Complete details on this material are presented in Raduha (2013) and Flores (2014). Here, for the sake of brevity, we present only paragenetic and mineralogical data necessary to characterize paleo fluid flow conditions that affected the interface sites. This is necessary to determine whether the features we investigate are "real" subsurface features or are the result of some sort of near surface weathering.

The rocks studied have undergone a complex diagenetic history that ranges from relatively early alterations, that probably began shortly after deposition, to late state alterations that occurred during uplift and exhumation (Fig. 19). Here we focus on alterations affecting the fracture networks in the caprock analogue lithologies as discussed above. Of particular relevance is the observation that the caprock fractures contain Fe-oxide pseudomorphs after pyrite, pyrite relics, and hydrocarbon fluid inclusions. (Fig. 20 and 21) indicates that upward migrating hydrocarbons passed through the fracture networks, likely also at depth. In addition, as noted previously, the fracture margins are "beached", which provided macroscopic evidence for hematite dissolution.

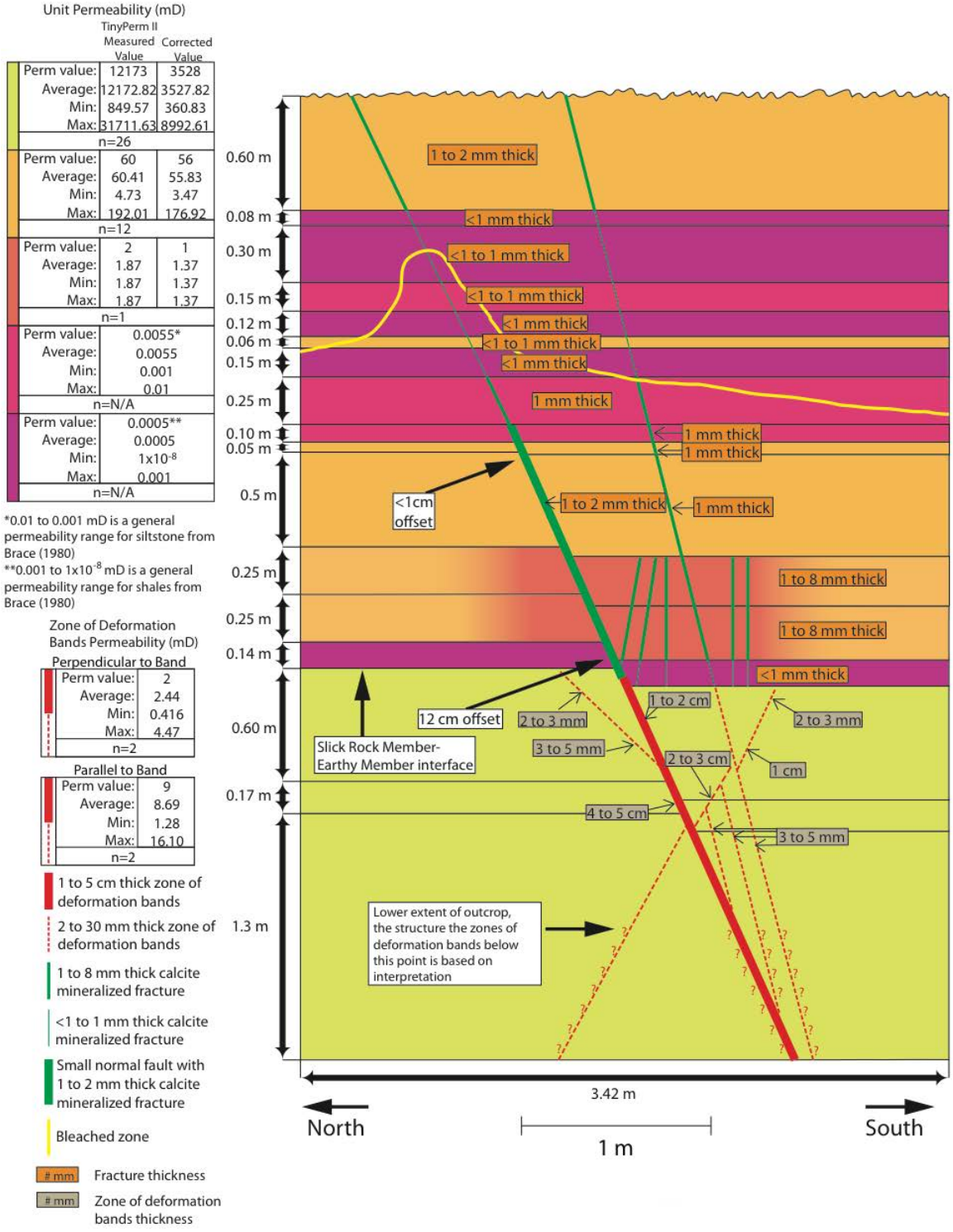

Figure 18. Permeability conceptual model of ISS-1. The color of each lithofacies corresponds to a different permeability, as noted in the legend. Permeability was determined using a combination of TinyPerm II measurements, laboratory permeability measurements, and laboratory permeability measurements from the literature.

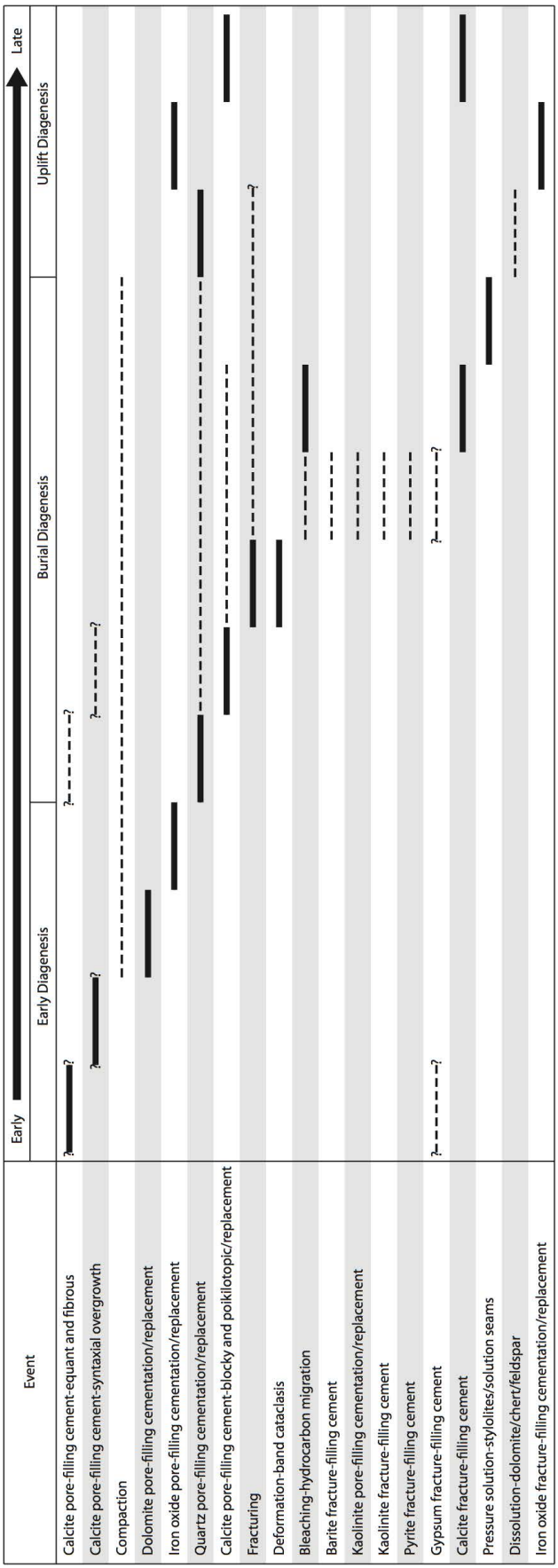

Figure 19. Summary of the relative timing of diagenetic alterations influencing the Navajo Sandstone, Carmel Formation, and Entrada Sandstone. Solid lines indicate the period during which an event occurred, dashed indicate a range of time over which the event may have occurred. Relatively early events are plotted towards the left, late towards the right. Question marks indicate uncertainty. Possible diagenetic environments are shown (see discussion section for justification).

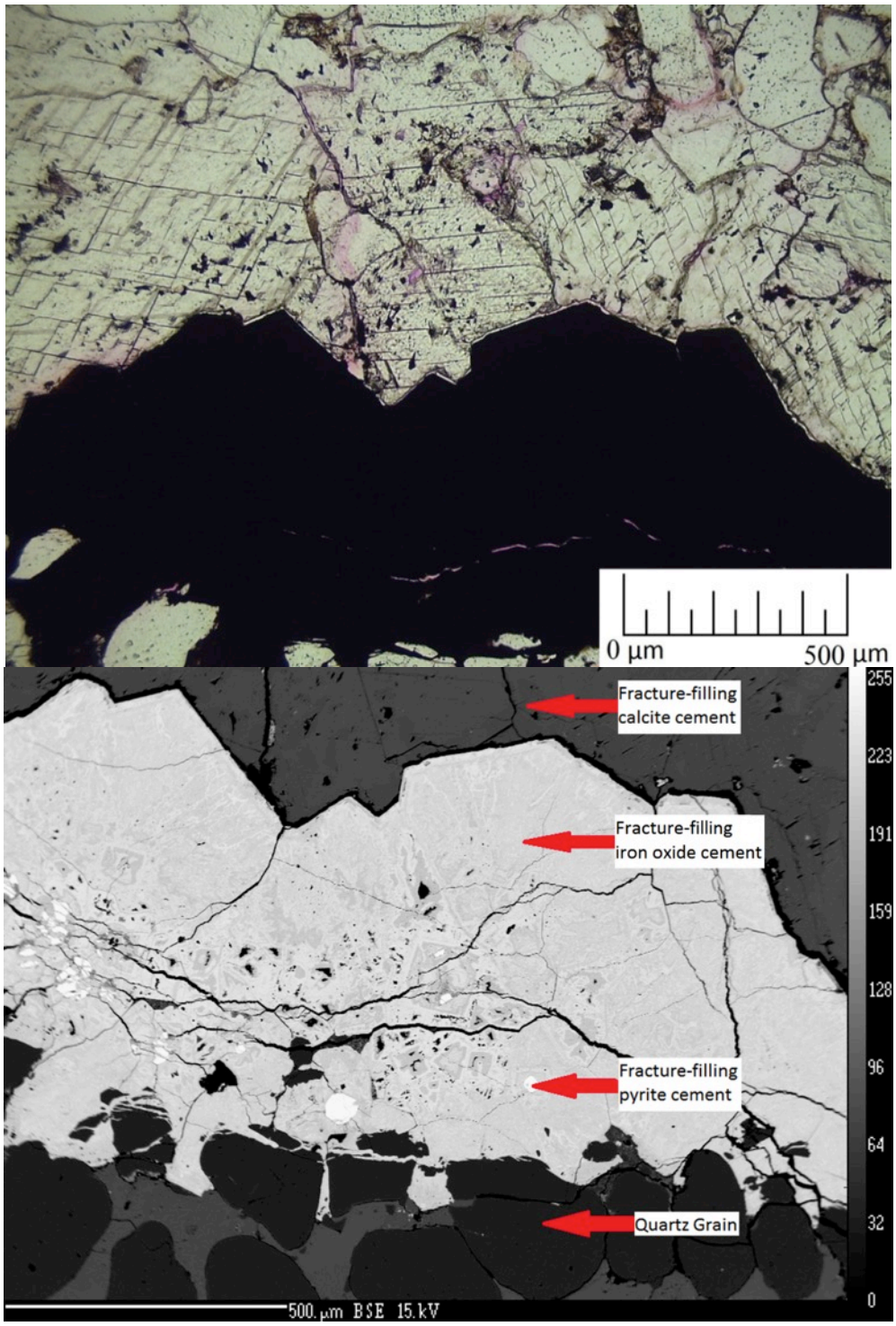

Figure 20. Thin-section photomicrograph (top) and back-scattered electron image (bottom) showing an opening-mode fracture filled by pyrite that was replaced by iron oxide. Calcite cement encases the iron oxide/pyrite, suggesting that calcite cement formed after both. Small relics of non-replaced pyrite are present inside the iron oxide. IW-31112-2A, Entrada Sandstone Earthy Member, plane polarized light above and backscattered electron image below.

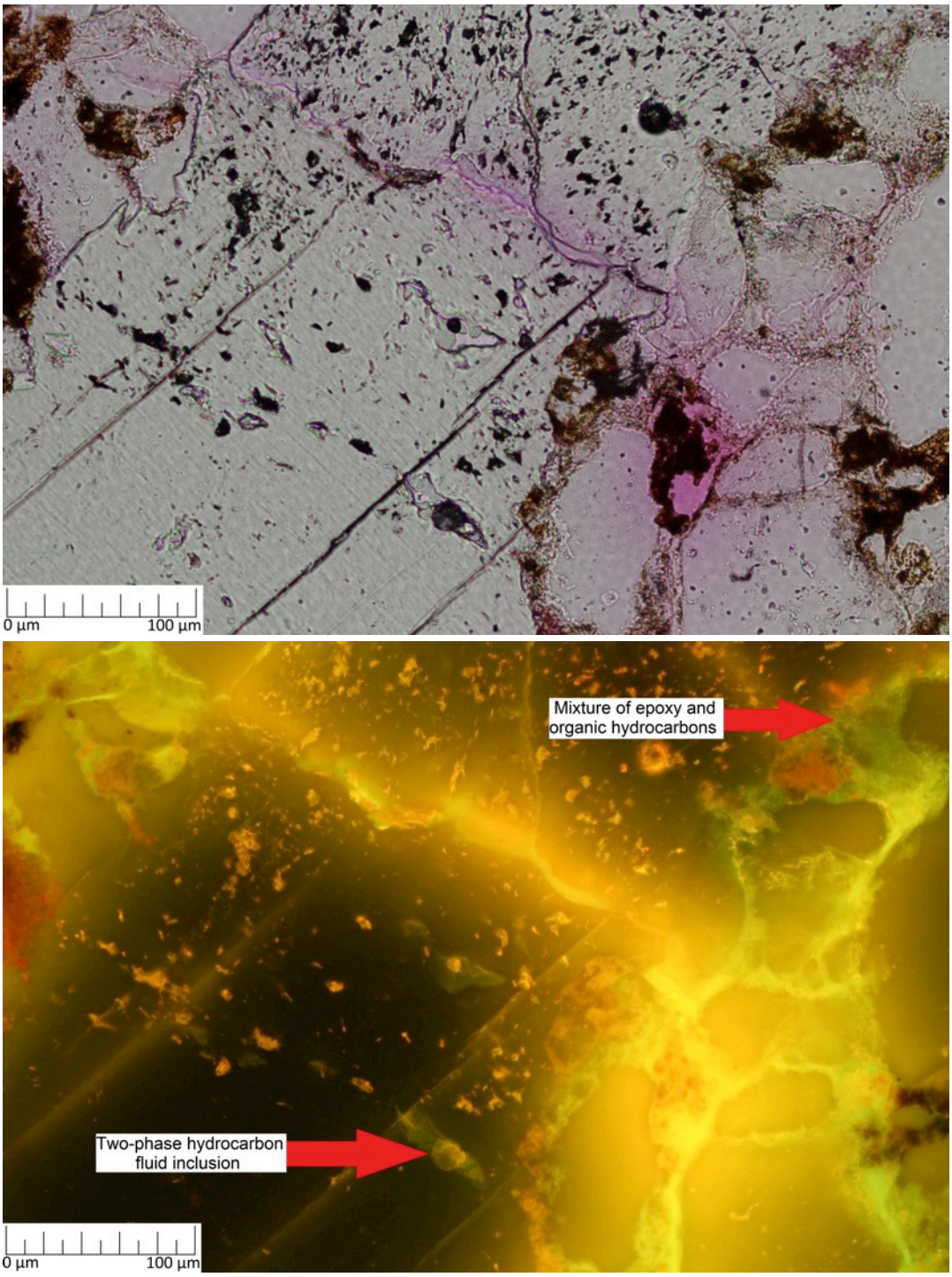

Figure 21. Thin-section photomicrograph showing two-phase hydrocarbon fluid inclusions inside calcite fracture-fill. The green inclusions are higher grade than the orange. This thin section is impregnated with fluorescent epoxy. The epoxy shows up red in plane polarized light and bright yellow in fluorescent light. Some of the fluorescence within the cracks between calcite fracture-filling cement is due to a mixture of organic hydrocarbons (green fluorescence) and epoxy (yellow fluorescence). UM-31312-16, Carmel Formation Co-op Creek Member, conoscopic plane polarized light above and fluorescent light below.

Regional mapping and description of structural features

We identify three sites that exhibit deformation related to folded and faulted structural settings. The sites are located in specific structural positions in which the Navajo Sandstone and Carmel Formation are exposed by uplift and erosion near the eastern margin of the San Rafael Swell (Fig. 22 and 23): 1) The steep east-dipping monoclinal fold limb, 2) The syncline hinge zone of changing curvature, and 3) Gently-dipping beds with small dip-slip separation faults conjugate to the Iron Wash Fault (Richey, 2013). These sites enable us to examine the influence of the structural setting for elements of fold geometry and faulting and the affect they have on seal competency.

The steeply-dipping monoclinal limb setting is located structurally between the anticline hinge and above the syncline hinge. The beds dip 60°-70° towards the east, and the bedding dip magnitude does not change in this setting, producing a curvature of 0.

Within the syncline hinge zone setting, the beds generally dip to the east, but the dip magnitude also decreases to the east. The changing dip magnitude presents a non-zero, negative, value of curvature. Additionally, the radius of curvature increases to the south.

East of the San Rafael Swell Monocline, the beds of the Navajo Sandstone and the Carmel Formation dip gently to the east (<10°). Faults with small separation values (10m and less) are located 1/4 mile northeast of the Iron Wash Fault.
The nature of fracture orientations and distributions were studied in outcrop where erosion has exposed the Navajo Sandstone (or Page Sandstone) and the Carmel Formation.

Uneva Site

The Uneva field site has 3 stations with n = 221 fracture orientation measurements in the lower Carmel Formation (Fig. 24). The site is located on the steeply-dipping beds (60-70°) of the San Rafael Swell monocline. Fracture orientations in the lower Carmel Formation are generally uniform, striking between 300/120az and 315/135az.

Uneva Station encompasses part of a relatively large fractures zone between 75-100 m wide. Exposure of the contact between the Navajo Sandstone and Carmel Formation is poor and is covered in 1-2 m of detritus, likely from preferential erosion of the fractured rock. Bleached detritus is visible where the fracture zone is expected to occur in the Carmel Formation. The best exposure of the Navajo Sandstone and the Carmel Formation are near the southern boundary of the fracture zone. Cataclasis deformation bands with positive relief (more erosion resistance) are present in the Navajo Sandstone. Along strike of the deformation bands and up section, opening-mode fractures in the Lower Carmel Formation limestone are bleached and mineralized. The fractures in

the limestone occur in clusters with low fracture spacing that are bleached with sharp bleached margins. The observations in the limited exposure may be a small scale representation of the features that are part of the larger fracture zone that is not exposed.

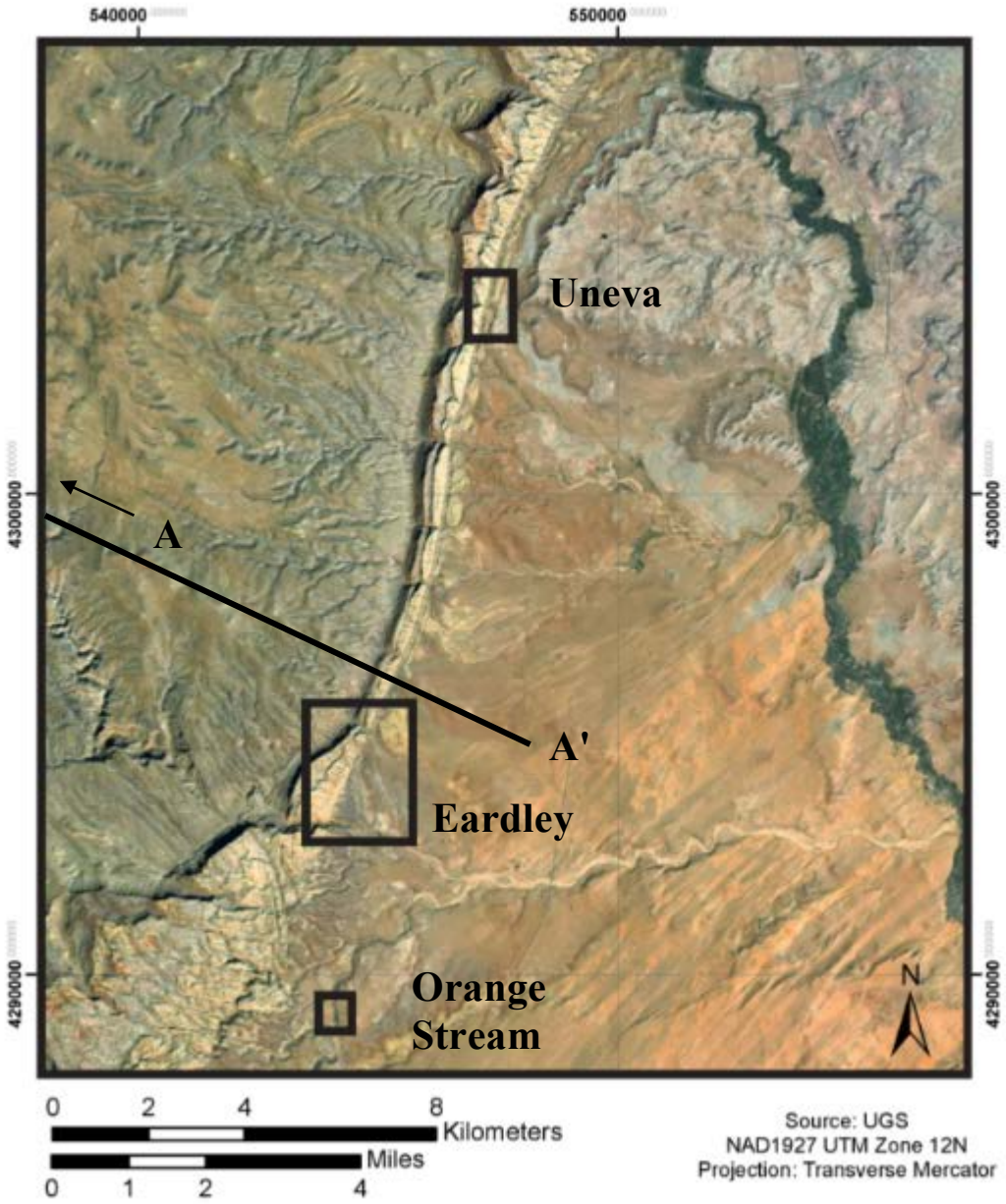

Figure 22. Field Sites for the San Rafael Swell Study Area. Each site represents a different structural position related to the monocline. Uneva is located on the steeply-dipping monoclinal limb. Eardley is located on the steeply-dipping fold limb but also contains the transition area to the gently-dipping beds. Orange Stream contains the faults with low normal separation values. The cross section line of Doelling (2002) and Figure 23 is also shown.

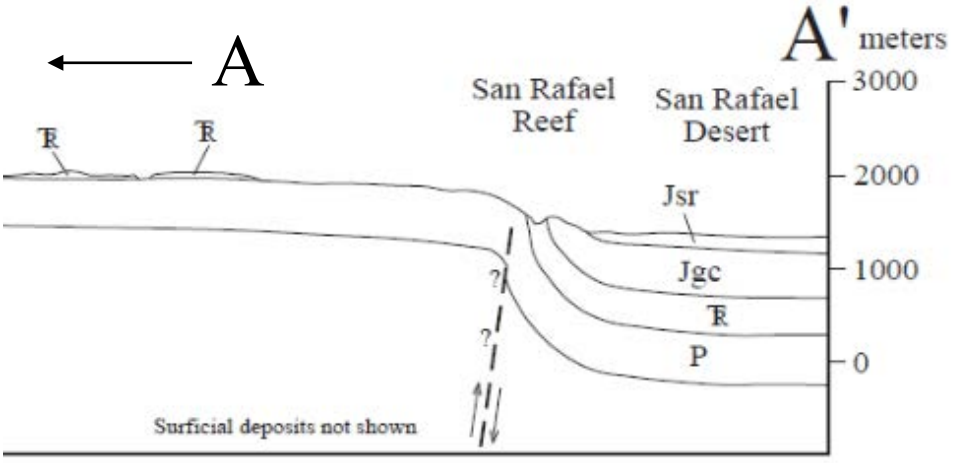

Figure 23. A portion of the cross section A - A' modified from Doelling (2002) that shows the steeply-dipping monocline limb of the San Rafael Swell. The cross section extents from WNW to ESE. The view is to the NNE.

The steeply-dipping monoclinal limb setting is located structurally between the anticline hinge and above the syncline hinge. The beds dip 60°-70° towards the east, and the bedding dip magnitude does not change in this setting, producing a curvature of 0.

Within the syncline hinge zone setting, the beds generally dip to the east, but the dip magnitude also decreases to the east. The changing dip magnitude presents a non-zero, negative, value of curvature. Additionally, the radius of curvature increases to the south.

East of the San Rafael Swell Monocline, the beds of the Navajo Sandstone and the Carmel Formation dip gently to the east (<10°). Faults with small separation values (10m and less) are located 1/4 mile northeast of the Iron Wash Fault.
The nature of fracture orientations and distributions were studied in outcrop where erosion has exposed the Navajo Sandstone (or Page Sandstone) and the Carmel Formation.

Uneva Station B has better exposure of deformation in the lower Carmel Formation; however, there is no exposure of the contact. Cataclasis bands are present in the Navajo Sandstone, but they exhibit negative relief (preferential weathering) in contrast to the deformation bands at station A. Along strike of the deformation bands, the red siltstone and mudstone of the lower Carmel Formation is fractured and bleached with sharp bleached margins on either side of the fracture zone.

Uneva Station C is located near the mouth of Uneva Canyon and is a good display of the reservoir-seal pair (Fig. 25). Exposure of deformation in the Navajo Sandstone and the Carmel Formation occurs in close proximity to the contact. Fractures in the lower Carmel Formation are bleached and mineralized . The bleached fractures in the Carmel Formation correspond to joints in the Navajo Sandstone. Though the jointing at station C

is a different style of deformation than that of stations A and B, the orientation of the structures are similar, and Carmel deformation observations is similar. The joints of station C intersect the walls of Uneva Canyon ~ 50 m from the entrance of the canyon. The multiple fractures near the contact become a single joint that cross-cuts deformation bands lower in the Navajo section.

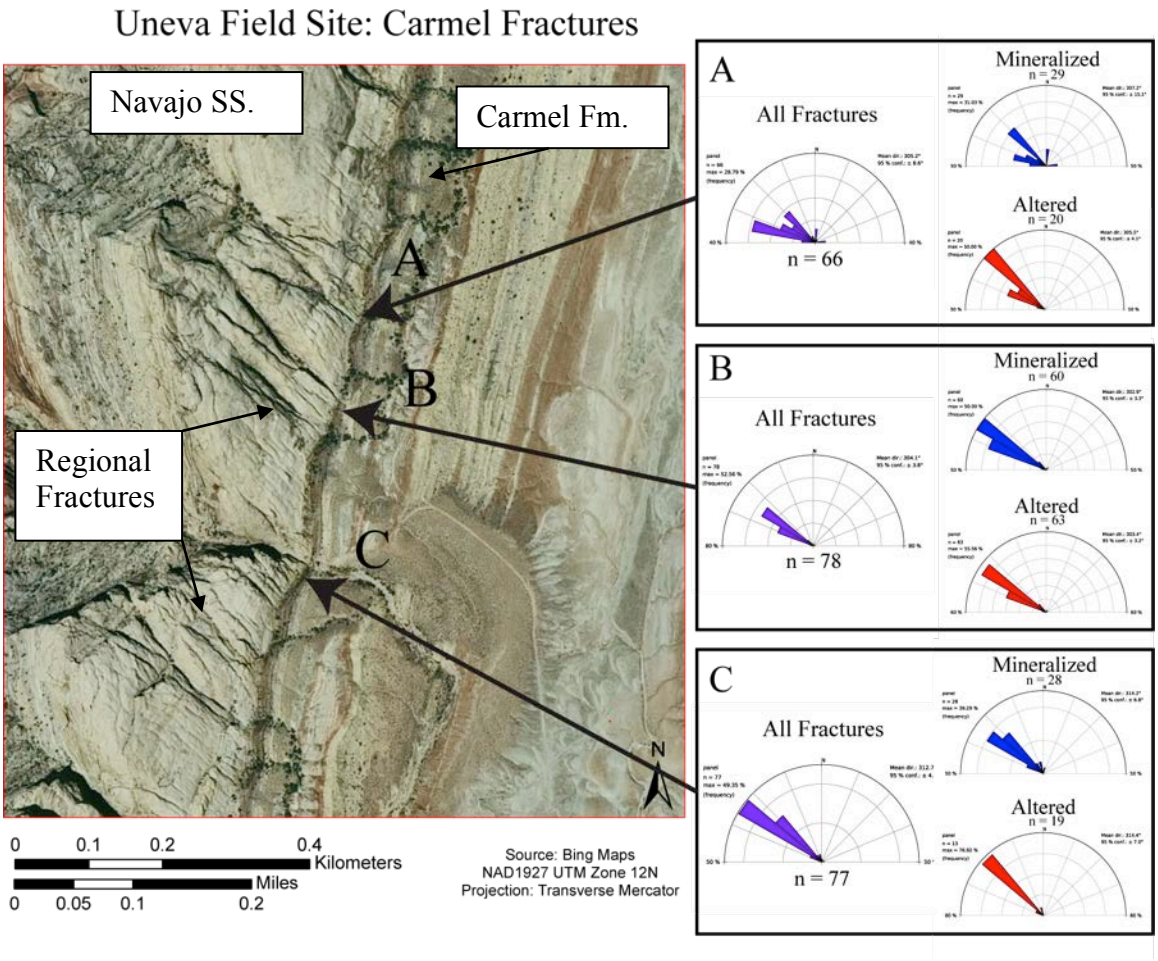

Figure 24. Aerial image of the Uneva field site with arrows pointing to stations A, B, and C. The half rose diagrams contain fracture orientations at each station for all fractures, mineralized fractures, and altered fractures. Fractures in the Navajo Sandstone visible and labeled.

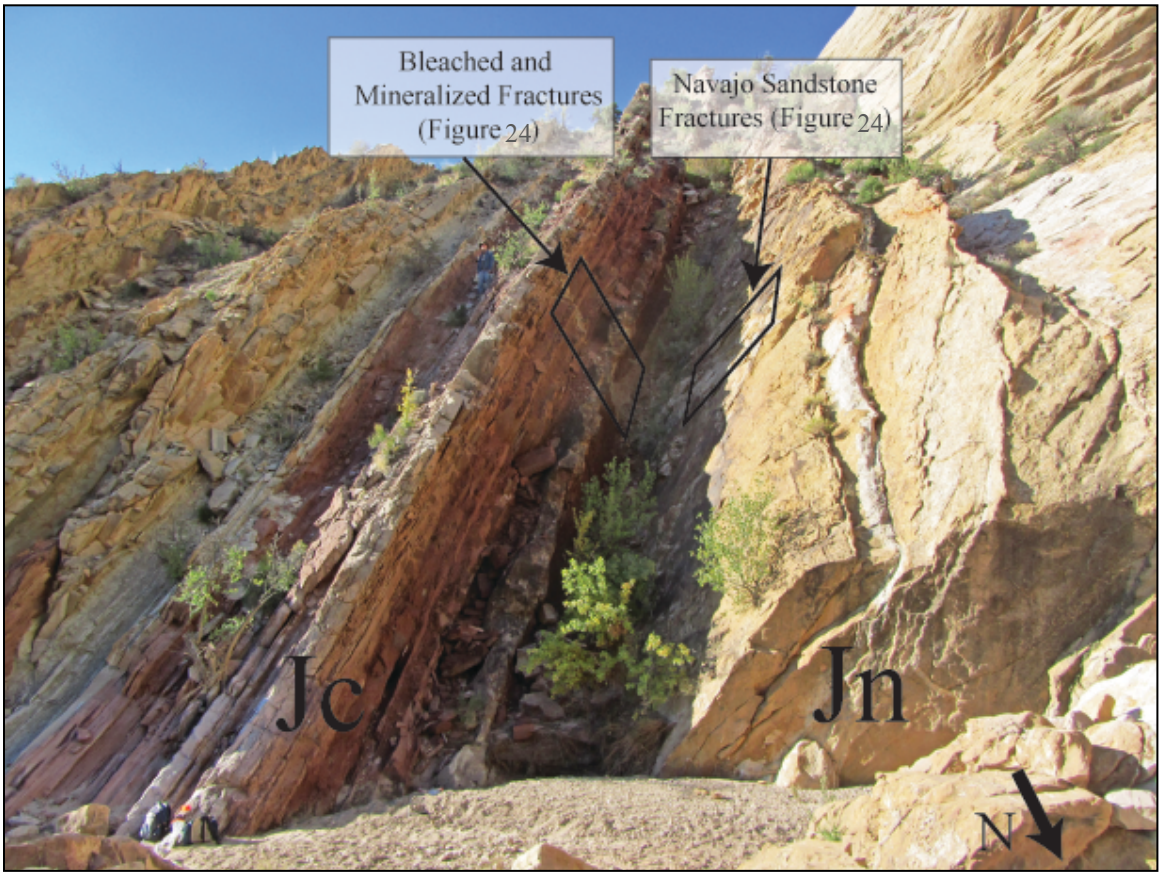

Figure 25. South-facing view of the contact between the Navajo Sandstone and the Carmel Formation taken near the mouth of Uneva Canyon. Bleached and mineralized fractures and fractures in the Navajo Sandstone are labeled with black boxes.

Eardley Site

The Eardley field site has 5 stations with n = 187 fracture orientation measurements in the lower Carmel Formation (Fig. 26). The stations are located within 2 structural positions. Stations A and B are located on the steeply-dipping monocline limb, similar to the Uneva Field Site, and stations C, D, and E are located near the hinge of the syncline.

The prominent fracture strike orientations for stations A and B are between 275/095az and 305/125az, nearly perpendicular to the bedding strike. Station B contains a fracture cluster in the Carmel Formation with sharp bleached margins and no shear. The corresponding structures in the Navajo Sandstone are joints. The limited exposure of the red rocks in the Carmel Formation shows bleaching similar to the Uneva Site.

Station A has a relative lack of structural complexity. Fracture spacing is high (low density) at station A and likely approximates background values for fracture spacing unassociated with features that compromise seal integrity. There are no bleached fractures and minimal fracture mineralization. The fractures at Station A may have formed during uplift, post-dating fluid migration.

Stations C, D, and E are near the hinge of the syncline of the San Rafael Swell monocline in zone of negative curvature. The fracture set of stations A and B (J1) are also present at stations C, D, and E, but an additional, possible younger, set of fractures is also present (J2). A N to N/NE striking fracture set is present near the hinge and is sub parallel to the syncline fold axis. Fractures in the Carmel Formation contain alteration halos and mineralization, but alteration and mineralization is generally confined to individual fractures, rather that clusters as seen on the steep monoclinal limb at the Uneva stations and Eardley station B. The Carmel Formation fractures transition into joints in the Navajo Sandstone. Fracture spacing is lower (fractures are closer to one another) where the radius of curvature of the syncline is smaller (greater curvature value). The density of mineralized and altered fractures appear greater where curvature values are greater. As the radius of curvature for the syncline increases to the south, the density of mineralized and altered fractures decreases.

The two fracture sets at Eardley stations C, D, and E occur at a high angle to one another. We assume that fractures open in the direction of least principal stress suggesting that local and regional paleostresses are responsible for the two fracture orientations (Fig. 28) if the fractures are similar ages.

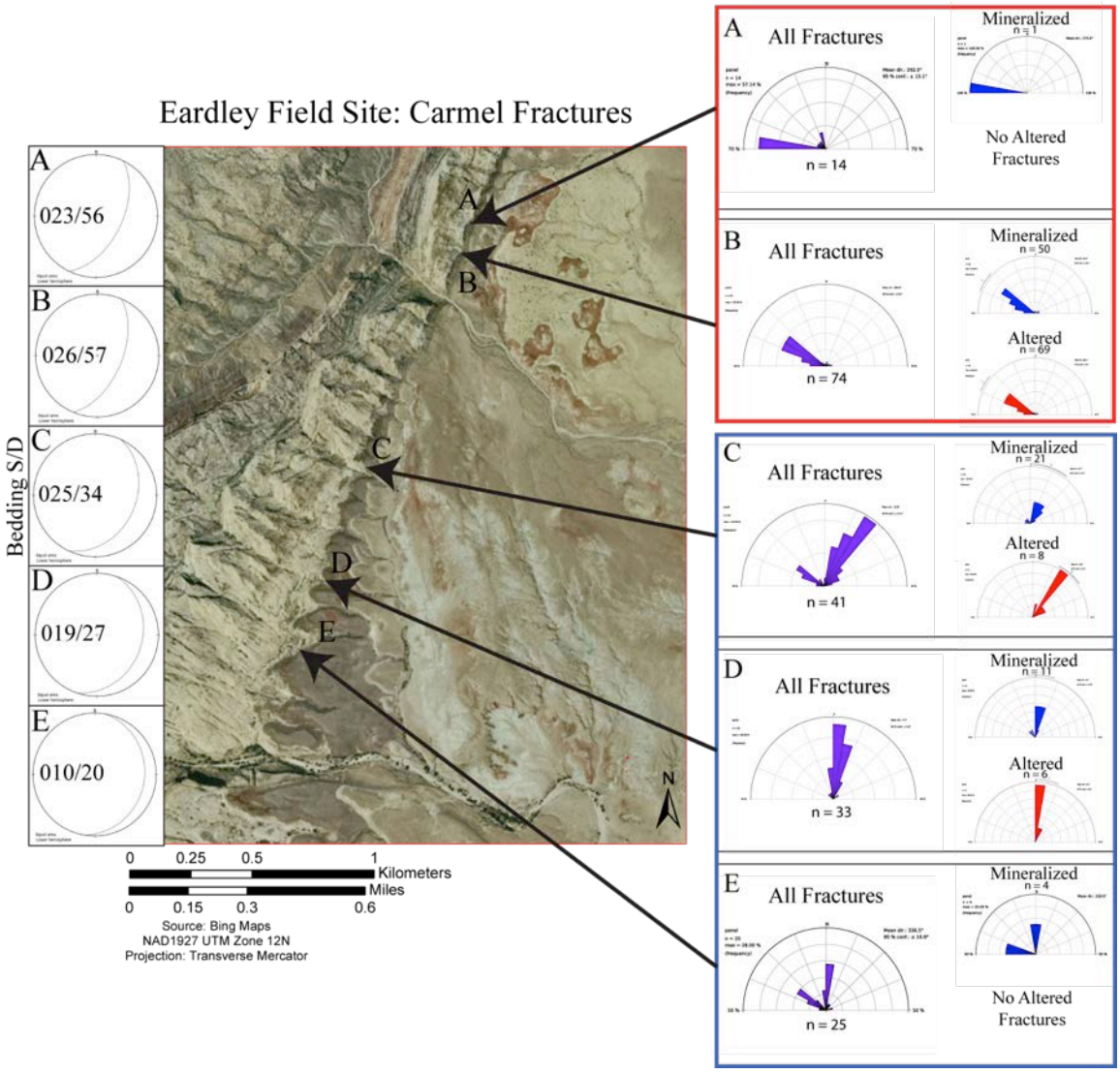

Figure 26. Aerial image of the Eardley field site with arrows pointing to stations A, B, C, D, and E. The half rose diagrams contain fracture orientations at each station for all fractures, mineralized fractures, and altered fractures. Two fold positions are distinguished by red and blue boxes. Bedding S/D shown on equal-area stereonets on the left.

Figure 27. South-facing photograph of the Eardley Field site. The Carmel Formation is the dark-colored formation in the foreground. The Navajo Sandstone is the in background. The dipping beds on the right side of the image are associated with high curvature values. The curvature at the hinge decreases to the south. Eardley stations C, D, and E located in black box.

Bleaching and mineralization appears to be directly related to fractures in the Carmel. The mineralization occurs in some of the fracture apertures, and when bleaching is present, it does not extend beyond 15 cm from the fracture. The timing of bleaching and mineralization with respect to the two fractures sets at the Eardley site is unclear. Iron-oxide veins are present in some of the joints as other joints appear to be bleached (iron-oxide removed). There does not appear to be a pattern to the distribution of bleaching and mineralization except that it appear more common at stations D, and E than at station A.

Fracture Sets

Three fracture sets exist within the field area. The most prominent set of fractures (J1) strike W/NW (Fig. 29) and are regional features that contain very little to no shear. Fractures in this set have long trace lengths and are visible in the Navajo Sandstone using aerial imagery. The second fracture (J2) set is considered local to the San Rafael Swell. The fractures do not appear to accommodate shear and are located within the hinge zone of the syncline. It is more common for J2 to terminate into J1, suggesting that J1 is slightly older, but many of the fractures cross-cut each other and form a mesh fracture network that may suggest the principal stress orientations were alternating within the syncline hinge.

The 3rd set of fractures is associated with the damage zones of the small separation faults and the Orange Stream field site. The faults strike orientations vary from 270°az to 296°az. Fractures near the faults tend to have similar orientations as the faults as described by Nelson (2001).

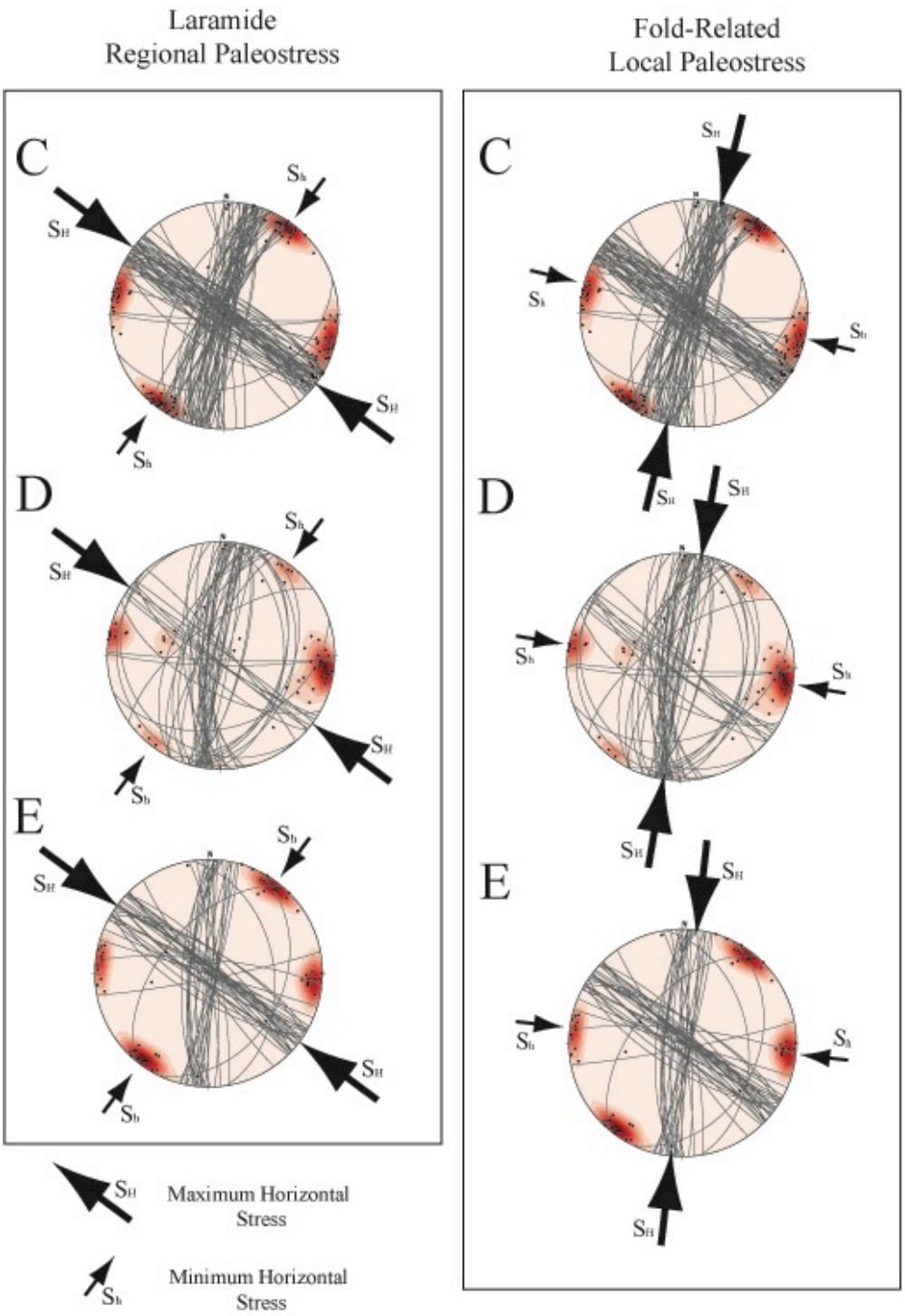

Figure 28. Equal area stereonets of joints in the Navajo Sandstone at the Eardley field site, Stations C, D, and E. Great circles of the joints are plotted with poles to those planes and contours. The large arrows show the maximum horizontal stress direction for both regional local stresses.

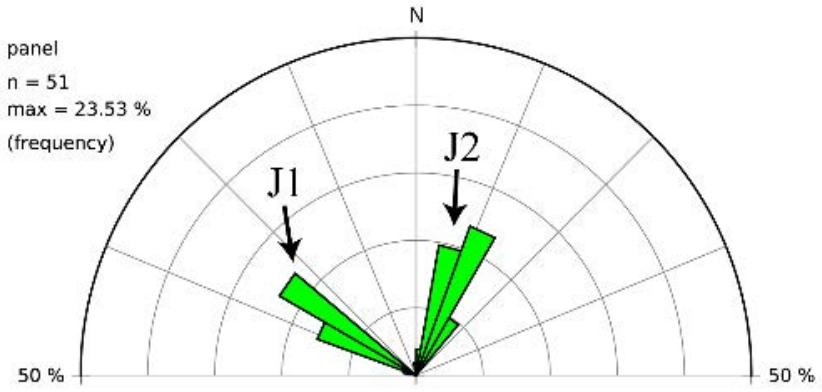

Figure 29. 180° Rose diagram displaying the two prominent fracture sets at the Eardley Field Site. Orientation data is from measurements made in the Navajo Sandstone.

The steeply-dipping fold limb primarily contains fractures from the J1 set. Eardley stations A and E (ES A and ES E) likely represents background values for fracture spacing/ density of the J1 fracture set. The rest of the stations listed in Table 1 have low spacing/high density related to fracture clusters that form at high angles to bedding. The fracture clusters have numerous bleached and mineralized fractures and occur within ~10m wide zones or less. Mineralization occurs within individual fracture apertures, but bleaching occurs for the entire cluster. The relative timing of the J1 joints may vary with respect to the formation of the San Rafael Swell. The J1 joints at Uneva station B crosscuts deformation bands that presumably formed during at the same time as the San Rafael Swell. The joints at the Eardly site seem to be slightly older to or the same age as the San Rafael Swell formation as seen by the crosscutting relationship with the J2 joints, features that formed during folding.

The third fracture set is associated with conjugate faults of the Iron Wash Fault system at the Orange Stream field site. Fractures that accommodate shear often form near faults. (Nelson, 2001). This group of fractures is grouped together as a single set, but fracture orientations reflect that of the nearby faults.

Table 1. Fracture Spacing (m/fracture) and fracture density (fractures/m) for the J1 fractures set in the Carmel Formation at the Uneva and Eardley field sites.

	J1 Median Spacing	J1 Density
ES A	0.38 ± 0.19	2.13
ES B	0.05 ± 0.09	8.53
ES C	0.06 ± 0.09	9.00
ES D	n/a	n/a
ES E	0.36 ± 0.18	2.29
UMS A	0.11 ± 0.10	6.60
UMS B	0.08 ± 0.08	7.80
UMS C	0.09 ± 0.09	7.70

Syncline Geometry and Curvature

Curvature is a proxy for strain in folded rocks and is defined as the inverse of the radius of curvature (Roberts, 2001; Chopra and Marfurt, 2007). Curvature in the study area range from zero on the steeply-dipping fold limb where dip does not change to negative values in the syncline. The syncline that is part of the San Rafael monocline is unique in that the sedimentary interface is exposed in a region where the curvature changes in the direction of the fold axis. A structural contour map (Fig. 30) shows the interface near each of the Eardley stations where scan line measurements were taken.

The structural contour map displays the geometry of the east-dipping beds of the area of interest at the Eardley field site. The steeply dipping beds on the northern portion of the map transition to less steeply dipping beds to the south. The dip of the eastern limb of the syncline is held relatively constant for the model. The dip magnitude of the western limb of the syncline, which also dips to the east, decreases causing the interlimb angle of the syncline to increase.

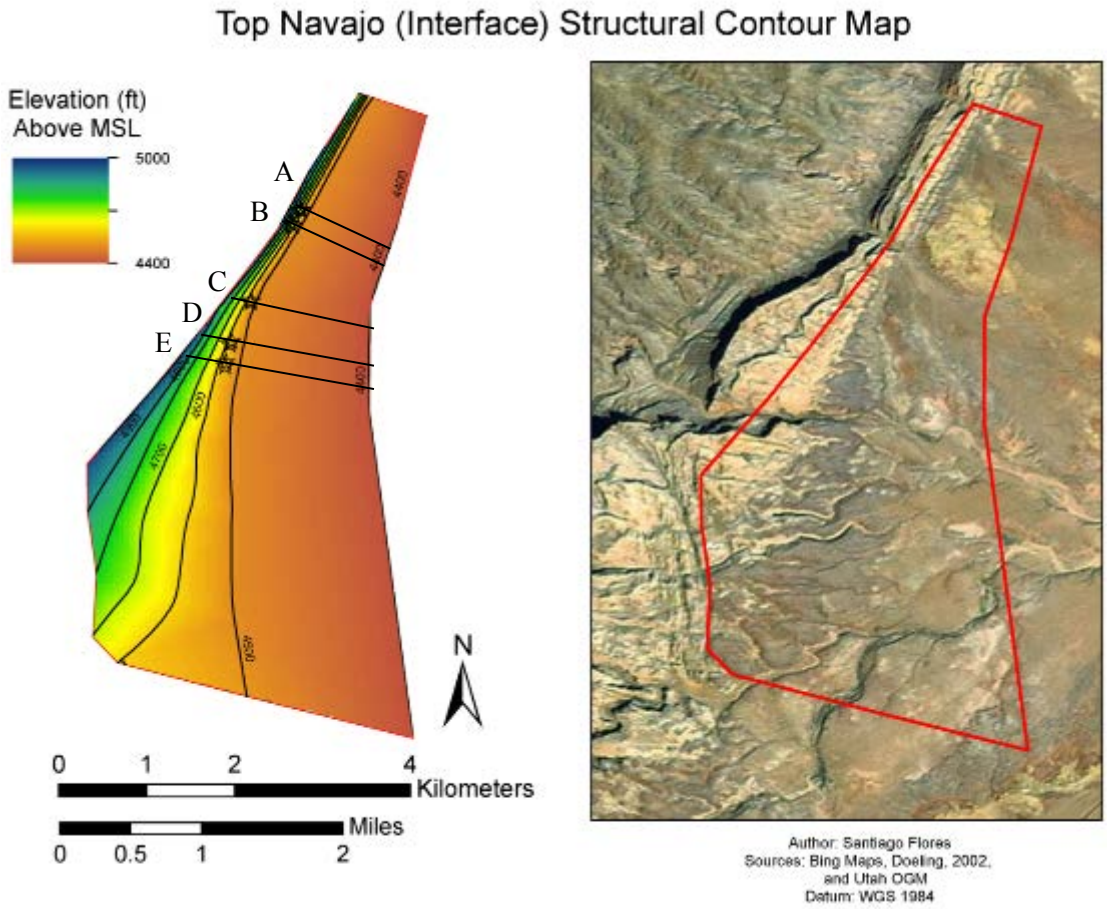

Figure 30. Structural contour map of the top of the Navajo Sandstone. Scan line station are labeled as stars. Cross-sections are displayed in Figure 31.

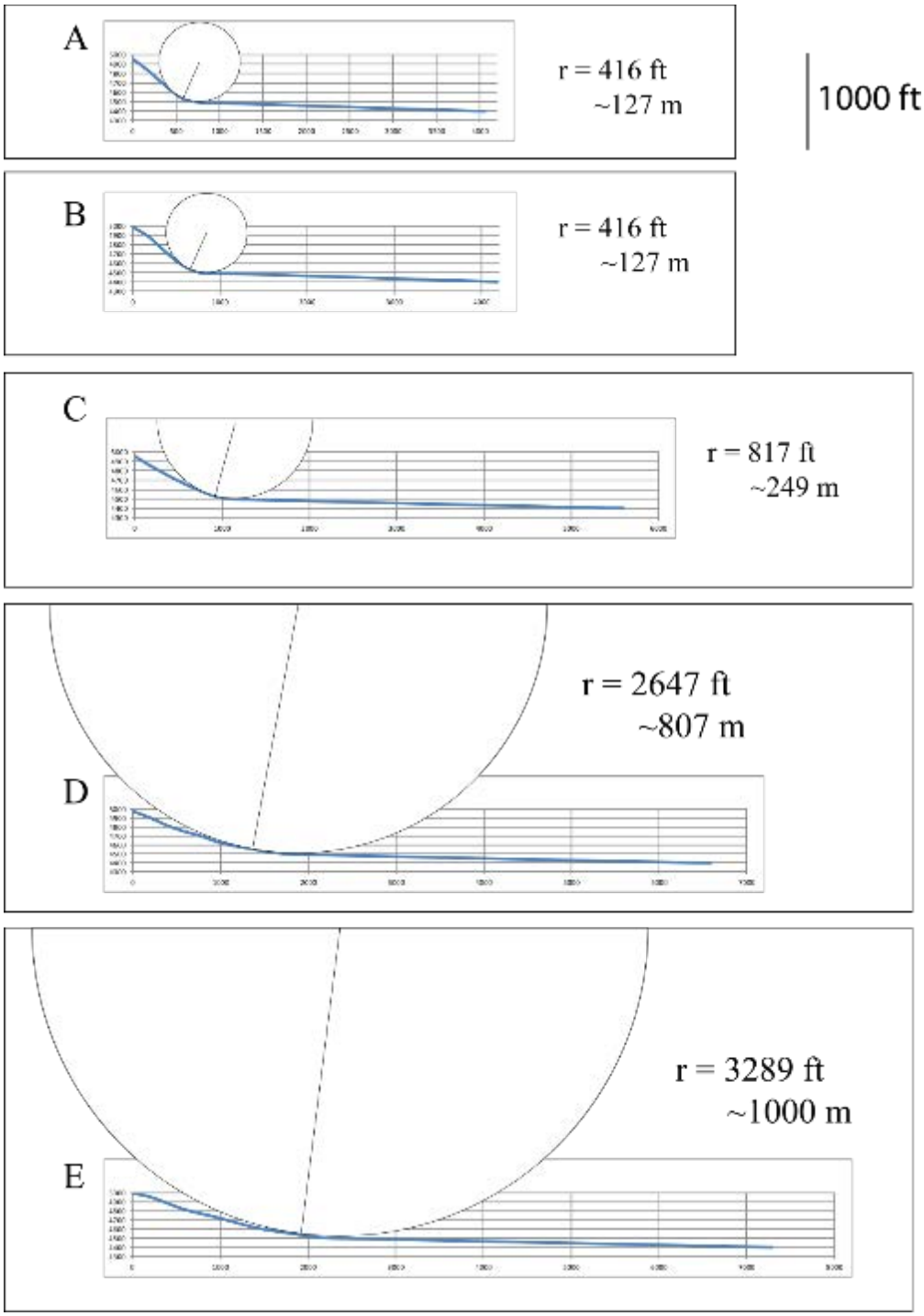

Figure 31. Cross-sections of the top of the Navajo Sandstone from lines labeled in Figure 30. The syncline hinge zone for each cross section is fit with a circle of radius (r) to quantify the curvature magnitudes.

The curvature also changes from north to south in the study area. The values for curvature are estimated by fitting a circle with radius of curvature (r) to the hinge zone of the syncline in cross section (Fig. 31). The radius of curvature for the northern portion of

the map is ~127 m and increases to ~1000 m near the southernmost cross section. The radius of curvature is determined from 2-Dimensional (2D) cross sections in a system we assume was folded isometrically (Lisle, 1992) for simplicity. The various ways of expressing the strain values for the syncline include the radius of curvature, curvature, and dip change (Table 2).

Table 2. Strain quantified by radius of curvature, curvature, and dip change for the syncline hinge of the cross sections of Figure 31.

	Radius of Curvature (r)	Curvature (1/r)	Dip Change (90°/r)
ES A	127 m	7.8 E-03 /m	0.71°/m
ES B	127 m	7.8 E-03 /m	0.71°/m
ES C	249 m	4.0 E-03 /m	0.36°/m
ES D	807 m	1.2 E-03 /m	0.11°/m
ES E	1000 m	1.0 E-04 /m	0.09°/m

The radius of curvature is much lower near Eardley stations A and B than at stations C, D, and E. These stations lie along the steepest-dipping portion of the monocline where strain is interpreted to be higher (Bump and Davis, 2003; Fischer and Christensen, 2004). With curvature acting as a proxy for strain, these results supplement the interpretations of strain distribution of the San Rafael Swell monocline.

South of the steeply-dipping beds, strain presumably decreases as curvature values for the syncline decrease. Eardley Station C, D, and E, ordered north to south, show syncline geometry with an increasing radius of curvature to the south.

Orange Stream Site

The Orange Stream field site is located on gentle (<10˚) east-dipping beds a quarter mile northeast of the Iron Wash Fault (Fig. 32). The stations are located near faults which have dip-slip separation ranging from 0.01m to 10 m. The Orange Stream field site has 3 stations located near faults with n = 160 fracture orientations in the Carmel Formation. The 3 faults strike between 270°az and 300°az. The faults are part of a larger system of faults conjugate to the Iron Wash Fault (Richey, 2013). The interface at this field site separates the Carmel Formation from the Page Sandstone (Fig. 33).

The ~10 m vertical wall and gently-dipping beds of the lower Carmel Formation at the Orange Stream site is a combination of mixed siliciclastics and carbonates. The outcrop is an ideal candidate for mapping using 3D photogrammetry in Sirovision® (Fig. 34). Outcrops of the lower Carmel Formation display lithologic and mechanical variability that likely exhibit a strong control on fracture density and connectivity (Laubach et al., 2009; Petrie et al., 2014).

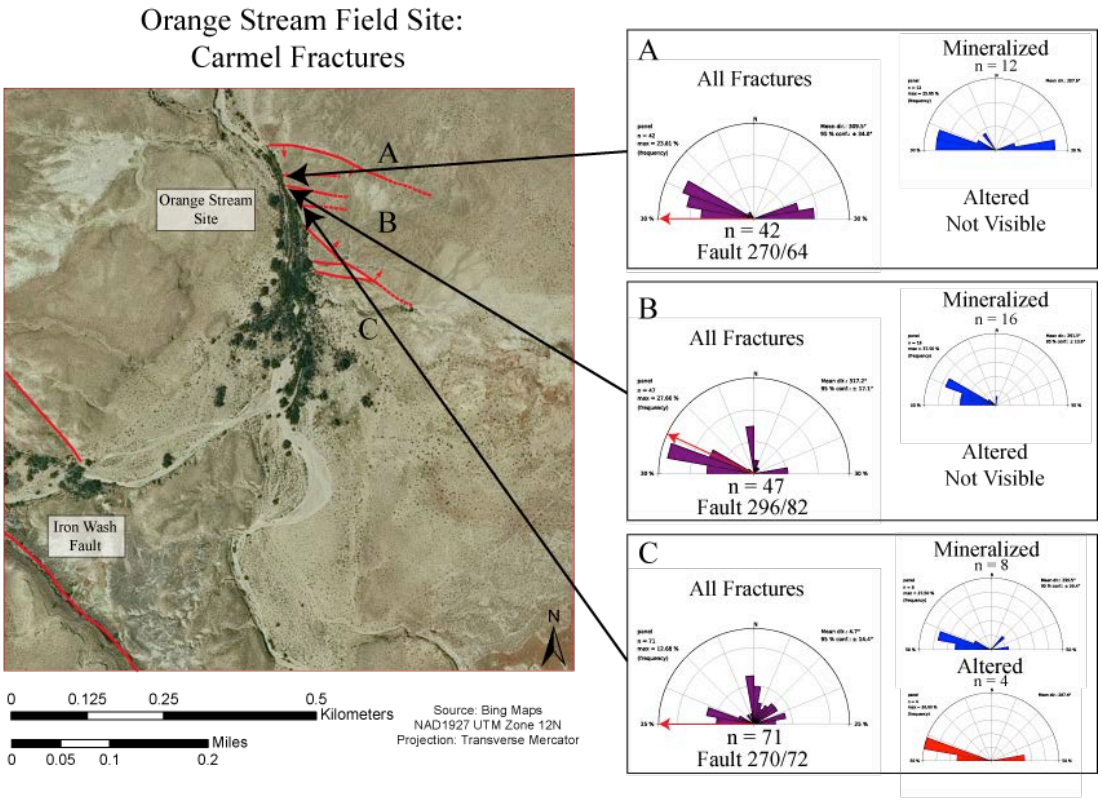

Figure 32. Aerial image of the Orange Stream field site with arrows pointing to stations A, B, and C. The half rose diagrams contain fracture orientations at each station for all fractures (purple), mineralized fractures (blue), and altered fractures (red). Iron Wash fault shown in red in the bottom-left corner of the image.

The largest alteration halos appear near the faults at the Orange Stream field site. Fractures surrounding the faults are mineralized and sometimes bleached, but to a lesser degree than the faults. The faults have calcite cores that have been damaged from faulting. The mineralized fault cores can be as large as 10cm. The faults appear as deformation band faults in the underlying Page Sandstone. hydrocarbon staining appears to follow the deformation band fault up to the contact with the caprock (Fig. 35), likely following fluid migration pathways.

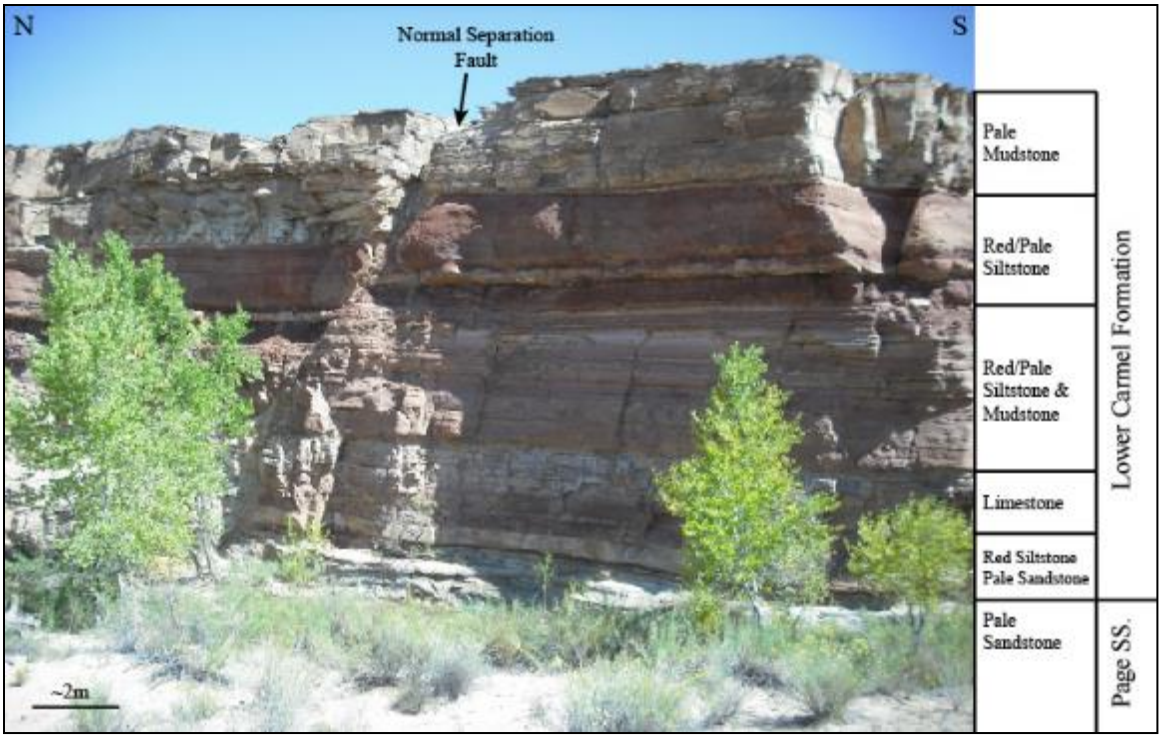

Figure 33. East facing view of the Orange Stream Field Site, Station A. 10 - 12 meters of the heterolithic lower Carmel Formation is exposed above the Page Sandstone.

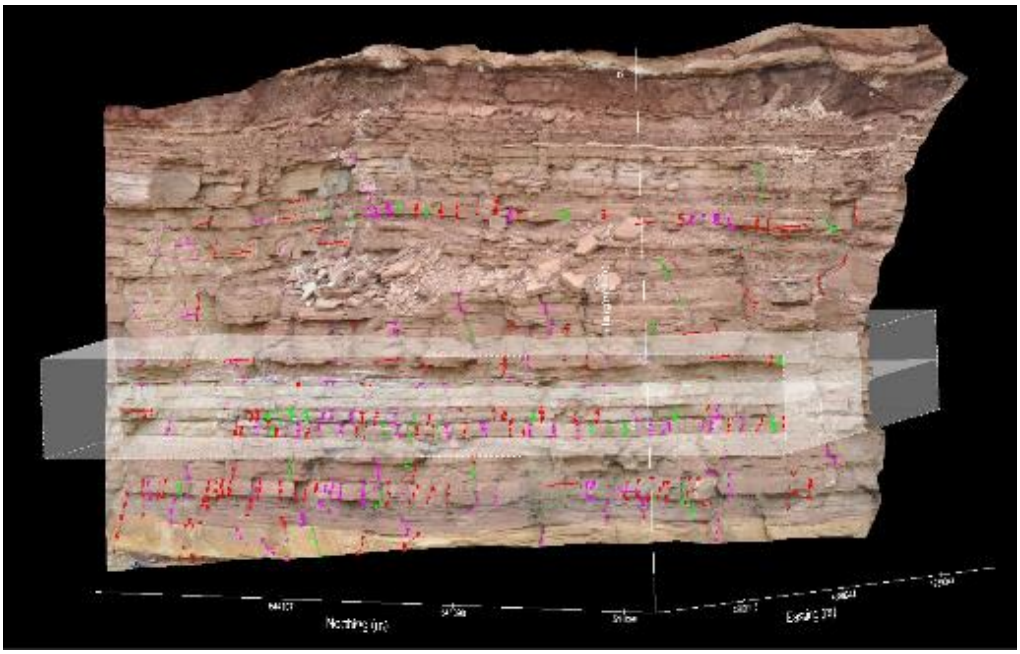

Figure 34. Fracture map and scan line example on a Sirovision 3D model of the lower Carmel Formation near Orange Stream station B. The fractures are color coded to the orientations, and the white box highlights the location of the selected scanline.

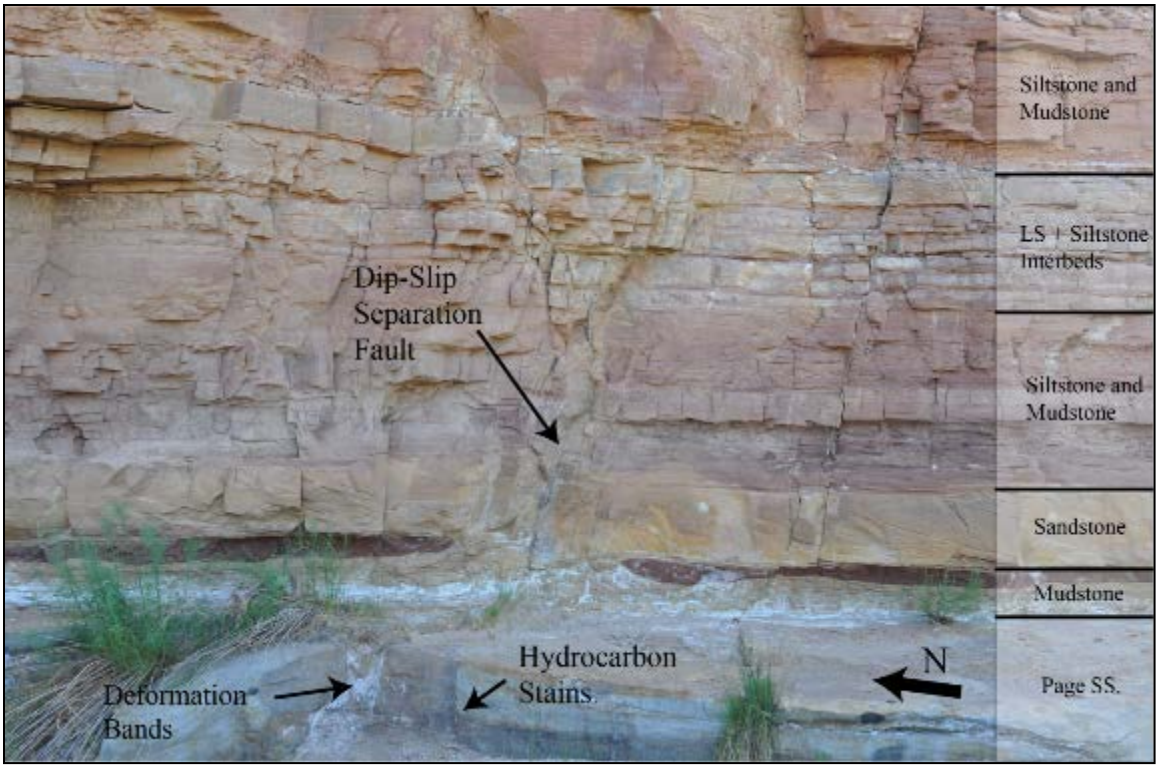

Figure 35. Orange Stream Station B. A deformation band fault in the Page Sandstone transition into a normal separation fault in the overlying Carmel Formation with J3 fractures present in the area.

Fracture control analysis

Fracture Density Controls

The fracture density data from the scan line measurements at each station is compared to dip change values from the curvature results (Fig. 36). Visual comparisons of the various locations in the syncline hinge zone suggest a relationship between fracture density and degree of alteration of axis parallel fractures (J2). The syncline in the northern portion of the Eardley field site exhibits high fracture density in the Navajo Sandstone with many fractures cemented with iron-oxide. The fracture density decreases to the south and may have less iron-oxide cementation. The fracture density may be related to the curvature of the syncline (Fig. 37).

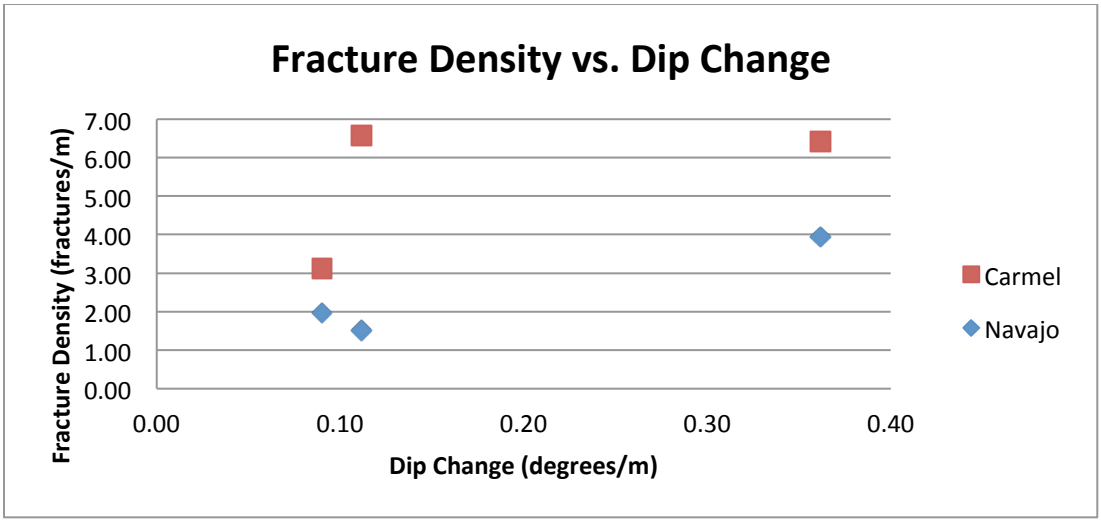

Figure 36. Plot of J2 fracture density vs. dip change. Data points taken from Eardley stations C, D, and E. Blue diamonds show data from the Navajo Sandstone and Red Squares show data for the Carmel Formation.

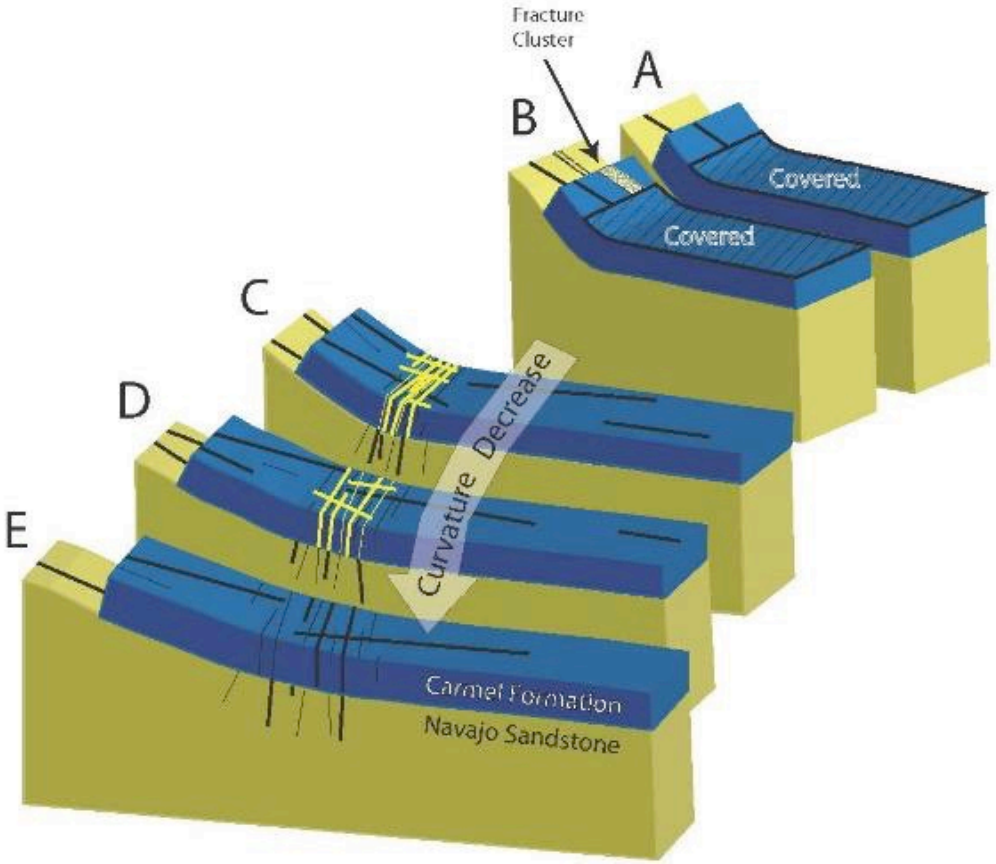

Figure 37. Block diagrams showing the geometry of the syncline near the Eardley Stations. The Carmel Formation is shown in blue and the Navajo Sandstone is shown in yellow. Bleached fractures are yellow, and a fractures cluster is displayed near station B. The view is to the N/NW.

The relationship between fracture density and curvature is recognized (Lisle et al., 1992, 1994; Fischer and Wilkersen, 2000; Hennings et al., 2000; Roberts, 2001; and Suo et al., 2012). A comparison of fracture density and dip change of the beds to fracture density may suggest a relationship between dip change and the fractures in the Navajo Sandstone, but the relationship is less clear in the Carmel Formation (Fig. 36). The plots were created using the three stations that contain J2 fracture data within the syncline hinge zone (Eardley Stations C, D, and E). The interface at the syncline hinge near Eardley Stations A and B is not exposed.

The total fracture density from the scan line data likely overestimates the subsurface fracture density as it includes fractures from uplift, possibly explaining the wide spread in fracture densities in the Carmel Formation (Fig. 38). To remove the fractures from decompression we use the bleached and mineralized fractures to explore relationships. There is a weak relationship between dip change and the bleached and mineralized fractures. The bleached and mineralized fracture densities from the Carmel Formation will provide a minimum for subsurface fracture densities because not all of the fractures that formed in the subsurface transmitted fluids. However, we interpret all of the bleached and mineralized fractures to be subsurface features. The relationships between fracture density and dip change are weak, but prediction models are often too simple and likely overlook some controlling factors. The coefficient of determination (R^2) for similar fracture and dip change data analyzed by Hennings et al., (2000) at Oil Mountain anticline produce R^2 values of 0.57. With more data acquisition for this study, a similar R^2 value is expected.

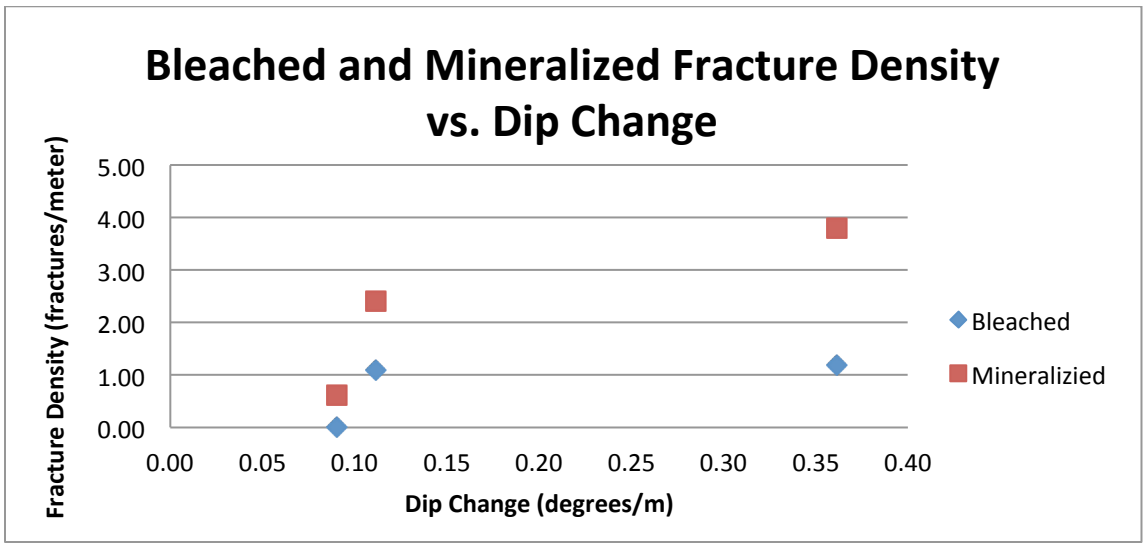

Figure 38. Plot of J2 mineralized and bleached fracture densities vs. dip change in the Carmel Formation. Data points taken from Eardley stations C, D, and E. Red squares show the mineralized fracture data and, blue diamonds show the bleached fracture data.

Fracture Deformation Styles

The deformation bands of the reservoir transition into opening-mode fractures in the caprock, capable of compromising the seal. The nature of the transition from deformation bands to opening-mode fractures is an important aspect of reservoir-seal modeling for CCUS applications. The different deformation styles stem from the properties of porous sandstone which deform by grain reorganization and comminution for compaction bands (Fossen et al., 2007 and references therein) while the fine-grained caprocks lack the porosity necessary for deformation band formation and, instead, form opening-mode fractures that may accommodate shear. Shear in deformation bands occurs throughout the band and only accommodates millimeters to centimeters of strain (Fossen et al., 2007 and references therein). The strain in the caprock does not occur on a discrete plane and may be distributed throughout a fracture network of increased permeability. Furthermore, clay-rich layers in the caprock may distribute the strain through ductile deformation. The change in deformation style may also be explained from a rock mechanics perspective. Petrie et al. (in press) show that mechanical properties, specific to lithology, affect the rock's response to stress and failure mode in Mohr-Coulomb space (i.e. different rocks with the same burial/tectonic history deform differently).

Orange Stream Site Synthesis

A stratigraphic column was used to record and display the lithologic variation in the exposures of the lower Carmel Formation at the Orange Stream site (Fig. 39). We combine the relative elastic strength from Schmidt hammer of each bed exposed to the fracture density modeled in Sirovision®. The schematic stratigraphic column with relative elastic strength and fractures density provides an examination of the properties described as they exist in outcrop.

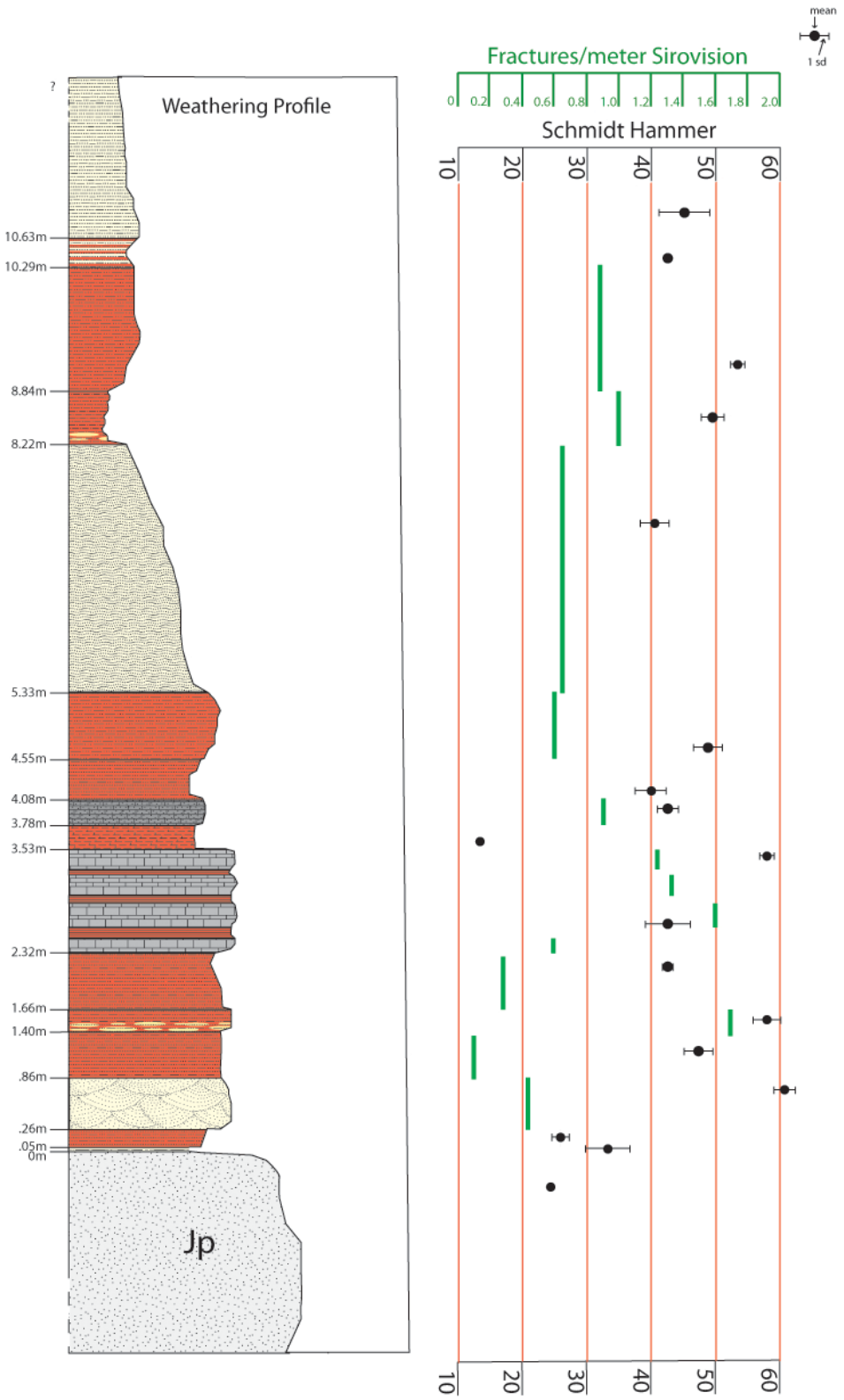

Figure 39. Stratigraphic column of the lower Carmel Formation at the Orange stream field site. Sirovision fracture densities are plotted alongside Schmidt hammer relative elasticity data for the major bed units.

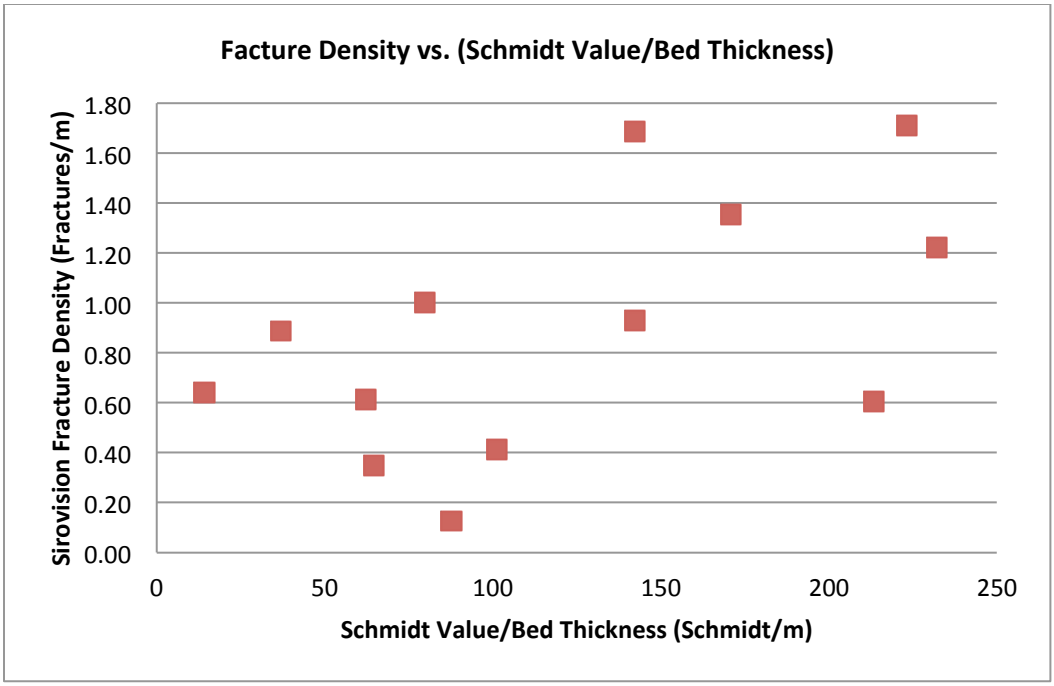

Figure 40. Plot of fracture density vs Schmidt Value/Bed thickness. The trend shows an increase in fracture density for thin strong beds.

The complicated interplay between lithology, bed thickness, strength, and fracture properties is apparent in analysis of the lower Carmel Formation. A relationship between bed thickness and fracture density is difficult to determine in the lower Carmel Formation (Fig. 40). This may be from incorporating four different broadly defined lithologies: siltstone, mudstone, sandstone, and limestone. The relationship may be further obscured by the resolution of the model as a result of the distance of the images from the face of the outcrop. The relative elastic strength, form Schmidt hammer, and fracture density also does not appear to have a direct relationship suggesting multiple factors contribute to fracture stratigraphy. Furthermore, mechanical properties may change after the fractures form (e.g., previously weak beds may become stronger following fracture formation and structural diagenesis).

The strongest relationship between bed thickness, elastic strength, and fractures density comes from comparing the fractures density to the ratio between relative elastic strength and bed thickness. The Schmidt values from outcrop were combined with scan line data from the 3D Sirovision model and stratigraphic column data. The Schmidt values for each bed is divided by its thickness. This provides high values of Schmidt value per thickness for thin, relatively strong, beds and low values for thick, relatively weak beds. This ratio is compared to fracture density in the Carmel Formation and displays a trend of increased fracture density for the thin/strong beds. The plot may contain subpopulations that are related to lithology.

Numerical Modeling

We ran a series of models varying the geometry of the meso-scale features at the reservoir-caprock interface (Table 3). A very large contrast in permeability was represented between the fractures ($3.3x10^{-7}$ m^2; $3.3x10^8$ mD) and the caprock ($5.0x10^{-19}$ m^2; $5.0x10^{-4}$ mD). The deformation-band fault permeability was about 3 orders of magnitude lower than the reservoir permeability. In addition, we varied the amount of fracture penetration through the caprock; both 70% and 100% fracture penetration through the caprock thickness were simulated (Fig. 41c-d).
Table 3 lists the hydrologic parameters used in the single- and multi-phase models. Table 4 lists the primary differences between the various model scenarios.

Table 3: Hydrologic parameters used in the FEMOC and FEHM models

	FEMOC ISS 1	FEHM ISS 1	FEHM WS
Reservoir Permeability (m^2)	3.5E-12	3.5E-12	3.5E-12 to 2.4E-13
Seal Permeability (m^2)	5.0E-19	5.0E-19	1.3E-19 to 5.0E-19
Deformation-Band Permeability (m^2)	2.0E-15	2.0E-15	2.0E-15
Fracture Permeability (m^2)	3.3E-07	3.3E-07	3.3E-07
Reservoir Porosity	0.23	0.23	0.23
Seal Porosity	0.10	0.10	0.10
Deformation-Band Porosity	0.04	0.04	0.04
Fracture Porosity	1.00	1.00	1.00

Table 4: Primary differences between the versions of the models

Hydro-stratigraphic Framework Model	Model Type	Reservoir-Caprock Interface Fault Properties	Fracture Penetration into Caprock	Lateral Head Gradient across Reservoir ($\Delta h/\Delta x$)
ISS 1	FEMOC	Fracture	100%	0.05
ISS 1	FEMOC	Deformation Band	100%	0.05
ISS 1	FEMOC	Fracture	70%	0.05
ISS 1	FEHM	Fracture	100%	5.10
ISS 1	FEHM	Deformation Band	100%	5.10
ISS 1	FEHM	Fracture	70%	5.10
Whole Section	FEHM	Fracture	100%	5.10
Whole Section	FEHM	Deformation Band	100%	5.10
Whole Section	FEHM	Fracture	70%	5.10

Single-phase Flow and Solute Transport

We first consider a series of single-phase FEMOC model results for the ISS 1 scenario, in which the geometry of the fault at the reservoir-caprock interface as well as the extent of fracture penetration through the caprock was varied (Fig. 41).

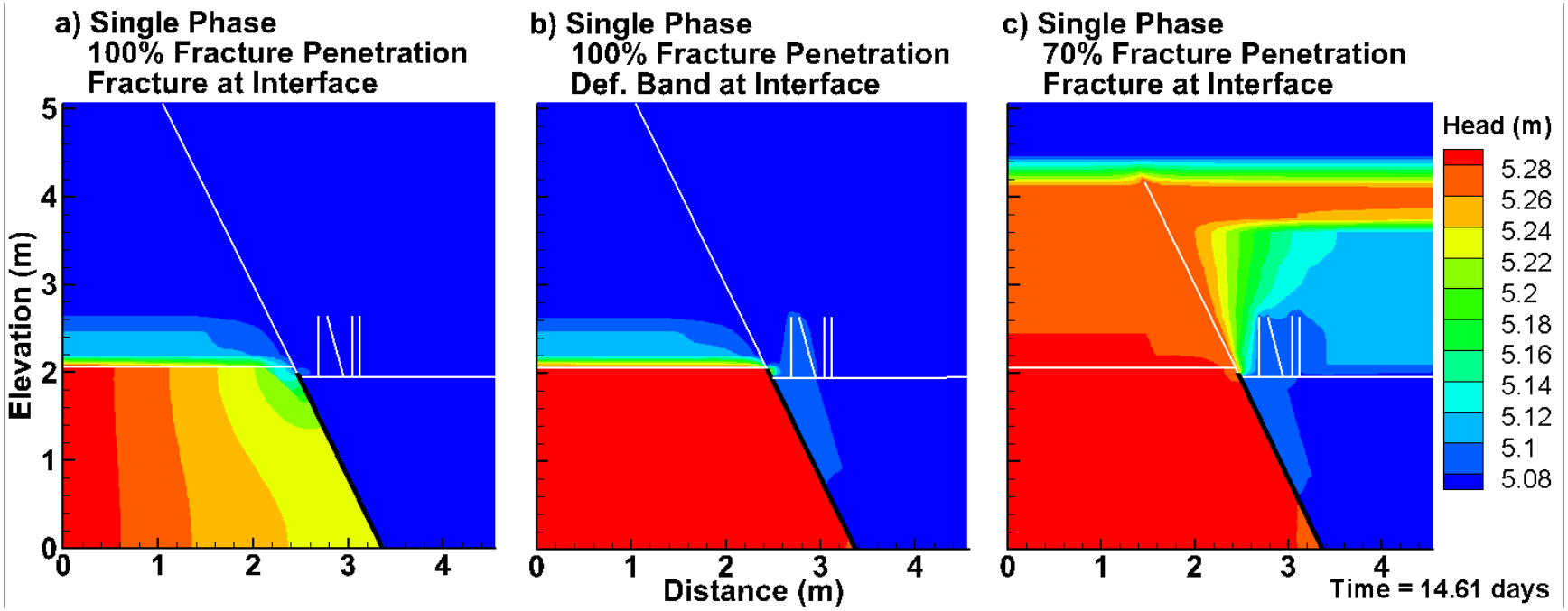

Figure 41. Calculated hydraulic head in meters, for the ISS 1 single-phase models. The horizontal solid white lines represent the reservoir-caprock interface and the sub-vertical black and white lines represent the deformation-band faults and fractures, respectively. Note the compartmentalization and flow focusing to the left of the deformation-band fault when the fracture is at the interface offset (a). Greater compartmentalization is simulated when the deformation-band fault is at the interface offset (b). Greater vertical head propagation is simulated when the fracture penetrates 70% of the caprock thickness (c).

In Figure 41a, the fracture fully penetrates the caprock and a permeable fracture is at the interface offset. The computed heads vary laterally from about 5.28 m to about 5.22 m up to the deformation-band fault. There is a large head drop across the deformation-band fault. Within the downstream portion of the reservoir, the head gradient is low. The hydraulic gradient to the left of the deformation-band fault is 3%, while the gradient to the right is only 0.54%. To the left of the deformation-band fault, the horizontal velocity (v_x) is $1.1x10^{-6}$ m/s, while right of the deformation-band fault the velocity (v_x) is $8.5x10^{-8}$ m/s. The upward velocity (v_z) into the caprock is $6.0x10^{-12}$ m/s. Within the main caprock fracture, the hydraulic head is 5.07 m and the vertical velocity (v_z) is $3.0x10^{-4}$ m/s.

Removing the permeable fracture at the reservoir-caprock interface has a profound effect on the computed head patterns (Fig. 41b). In Figure 41b, the deformation-band fault is at the interface offset. This simulation shows significant pressure compartmentalization. Almost all of the head change occurs across the deformation-band fault. The lateral head gradient across the deformation-band fault is 227%. The hydraulic gradient to the left of the deformation-band fault is 0.53%, while the gradient to the right is 0.82%. To the left of the deformation-band fault the horizontal velocity (v_x) is $1.8x10^{-7}$ m/s, while right of the deformation-band fault the velocity (v_x) is $1.6x10^{-7}$ m/s. This difference is likely due to small amounts of vertical leakage into the caprock. The upward velocity (v_z) into the caprock is $6.3x10^{-12}$ m/s, which is nearly the same as the case where fracture is at the interface (Fig. 41a) Within the main caprock fracture, the hydraulic head is 5.07 m and the vertical velocity (v_z) has decreased by two orders of magnitude to $3.0x10^{-6}$ m/s.

Reducing the caprock fracture penetration to 70% of the caprock thickness creates a bottleneck for flow (Fig. 41c). The top of the fracture is encased in relatively low permeability caprock facies. The geometry of the fracture at the reservoir-caprock interface is the same as in Figure 41a. This simulation also shows significant head compartmentalization within the reservoir. Most of the head now dissipates across the caprock facies (Fig. 41c). The vertical hydraulic gradient in the caprock is 8.1%. The hydraulic gradient to the left of the deformation-band fault is 0.58%, while the gradient to the right is 0.97%. Left of the deformation-band fault the horizontal velocity (v_x) is $2x10^{-7}$ m/s, while right of the deformation-band fault the velocity (v_x) is $1.3x10^{-7}$ m/s. The upward velocity (v_z) into the caprock is $3.8x10^{-12}$ m/s. Within the main caprock fracture, the hydraulic head is 5.28 m and the vertical velocity (v_z) is $6.5x10^{-7}$ m/s. The lateral flow velocity (v_x) into the permeable caprock facies is $1.2x10^{-7}$ m/s.

Next, we consider the effects of these three different fault-zone scenarios on solute transport (Fig. 42). We selected a common simulation time of 14.6 days. This time was selected to allow bypass comparisons. At 14.6 days the solute has fully bypassed the caprock, when the fracture is at the interface offset (Fig. 42a). Thus, the impacts of geometry variations in the other scenarios are easily determined. Solute was

introduced (specified concentration) at the upper two nodes of the reservoir unit, along the up-gradient side of the solution domain. These boundaries simulated solutes developing in the presence of the CO_2 plume and migrating into the system.
The geometry variations in Figure 42 are the same as the variations described for Figure 41. In all simulations, the solute is restricted to the top of the reservoir. This is likely due to the focusing effects of the deformation-band fault and the hydrostatic head assigned to the top of the fracture. In Figure 42a, the solute flows towards and then up into the main fracture. Within the main caprock fracture, the normalized concentration is 0.08 after 14.6 days.

When the deformation-band fault is present at the interface, no solute has entered the caprock fracture after 14.6 days (Fig. 42b). In this scenario, the solute flows towards the main fracture, but due to the low permeability of the deformation-band fault at the interface offset it does not flow into the fracture. Within the main caprock fracture, the normalized concentration is 0.0.

When the top of the fracture is encased in relatively low permeability caprock facies, solutes begin to invade the more permeable facies within the caprock. In **Figure** 42c (70% fracture penetration), the solute flows towards and then up into the main fracture, but the solute is diverted into a relatively high permeability layer in the caprock. Solute only flows to the right in this simulation as a result of the small subsidiary fractures present in this model. These subsidiary fractures contact the reservoir, thereby providing a connection to the lower head boundary on the right side of the reservoir. Within the main caprock fracture, the normalized concentration is higher than all previous model scenarios at 0.12. This is likely due to solutes accumulating within the fracture, since they cannot exit at the system at the top of the fracture.

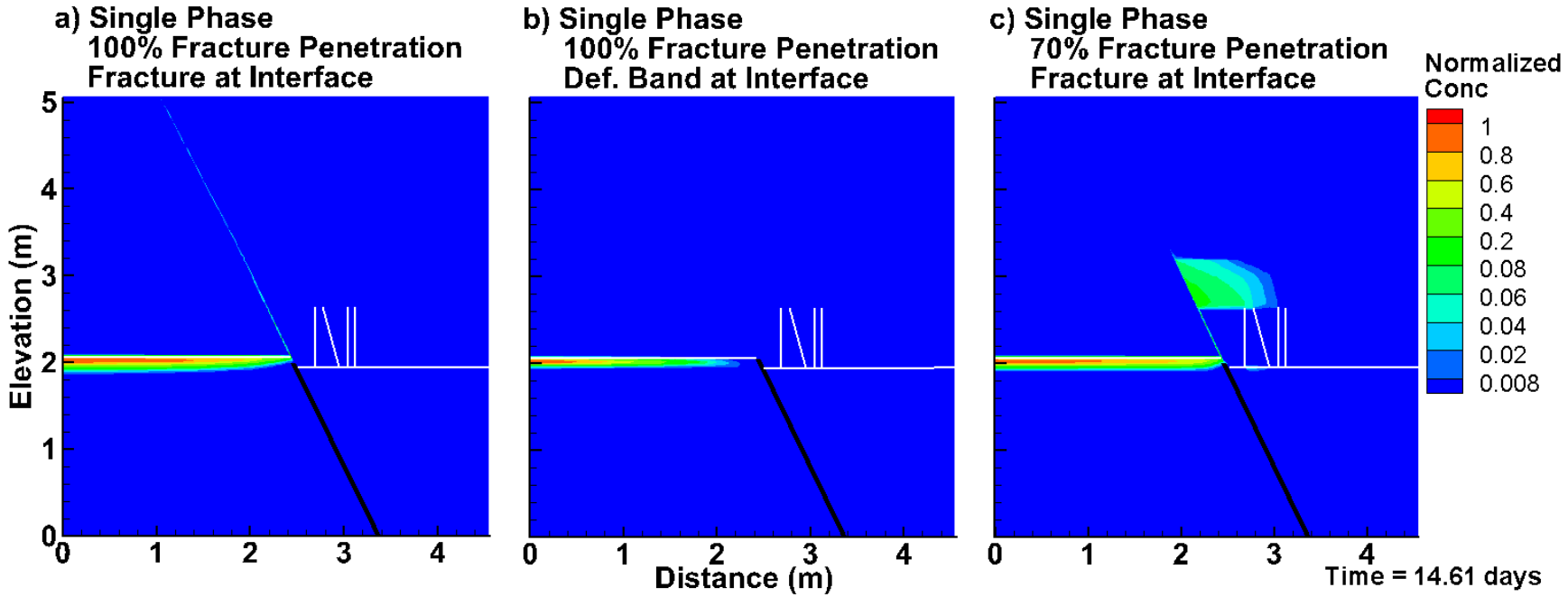

Figure 42. Calculated normalized solute concentration, for the ISS 1 single-phase models. The horizontal white lines represent the reservoir-caprock interface and the sub-vertical black line represents the deformation-band fault. The solute bypasses the caprock when the fracture is at the interface offset (a). The solute does not enter the fracture when the deformation-band fault is at the interface offset (b). The solute migrates laterally into a relatively high permeability caprock facies when the fracture penetrates 70% of the caprock thickness (c).

Multi-Phase Supercritical CO_2 Transport

Next we consider the effects of the three meso-scale fault zone scenarios, for a two-phase flow system. In this set of model runs, the pressure gradients are higher as we are closer to the injection well. The lateral pressure gradient is about 100 times greater. As a result, CO_2 flow rates are higher and we chose to present results for three simulations of ISS 1 at 0.13 days, with one simulation presented at 18.17 days, and at 4.11 and 29.50 days for all Whole Section simulations.

ISS 1

In Figures 43 and 44 the fluid pressure and the supercritical CO_2 saturation calculated by FEHM are presented, respectively. To some degree, these plots are analogous to the head and normalized concentration results from FEMOC. It should be noted that the pressure patterns, in Figure 43, are influenced by the presence of supercritical CO_2 and its effect on relative permeability. The slight horizontal shift in the contours, observed between 1 and 2 m in elevation, is the result of changes in fluid saturation and relative permeability. Specifically, the presence of CO_2 alters the capillary pressures in the system which then alters the total fluid pressure.

The region where a critically stressed fault might fail (i.e. the failure envelope) is indicated with a dashed white line for each model scenario. This failure envelope was calculated using equation 25. We calculated the critical pressure assuming a depth of about 2 km and we selected an α value of about 0.62. This critical pressure was then subtracted from the calculated fluid pressures to determine the location of the failure envelope.

In Figure 43a, the fracture fully penetrates the caprock and a permeable fracture is at the interface offset. The pressure gradient to the left of the deformation-band fault is 4%, while the gradient to the right is 0.2%. Left of the deformation-band fault the horizontal CO_2 velocity (v_x) is 4.4×10^{-4} m/s. Within the main caprock fracture, the pressure is 19.79 MPa and the vertical CO_2 velocity (v_z) is 6×10^{-4} m/s. Everywhere else, the CO_2 velocity is 0.0 m/s. The failure envelope encompasses the whole reservoir left of the deformation band and the whole caprock fracture.

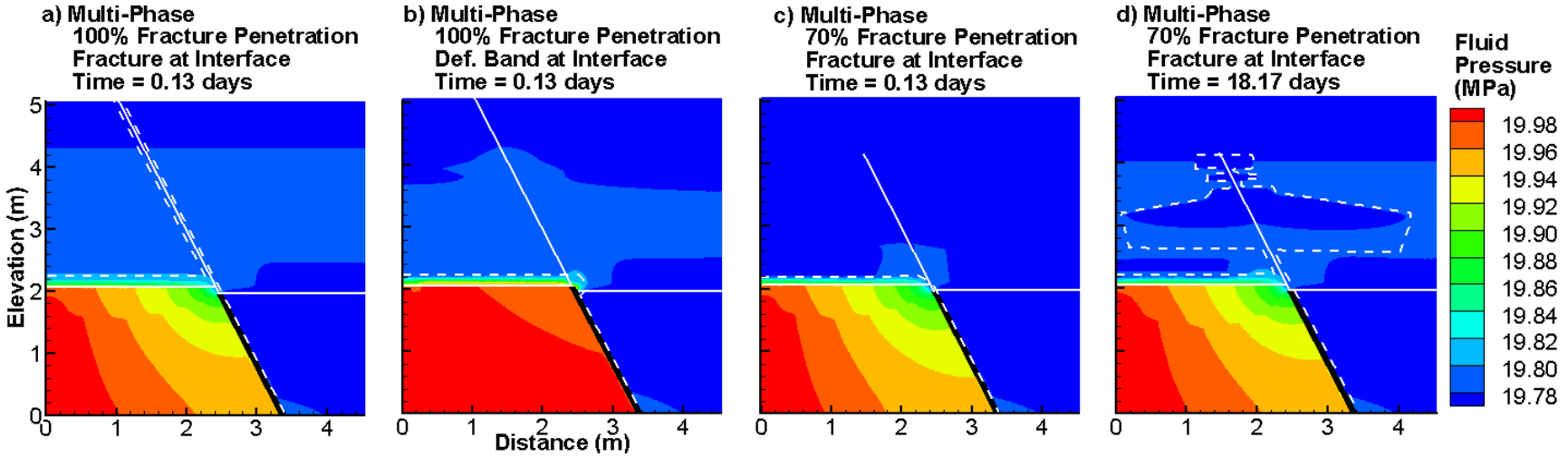

Figure 43. Calculated fluid pressure in megapascals, for the ISS 1 multi-phase models. The horizontal white lines represent the reservoir-caprock interface and the sub-vertical black and white lines represent the deformation-band fault and fracture, respectively. The dashed white line shows the failure envelope. Flow compartmentalization and focusing left of the deformation-band fault is observed when the fracture is at the interface offset (a). Greater compartmentalization is simulated when the deformation-band fault is at the interface offset (b). Compartmentalization and small vertical propagations of pressure into the caprock are simulated at early time, when the fracture penetrates 70% of the caprock thickness (c). Greater vertical propagations of pressures is simulated at late time, when the fracture penetrates 70% of the caprock thickness (d).

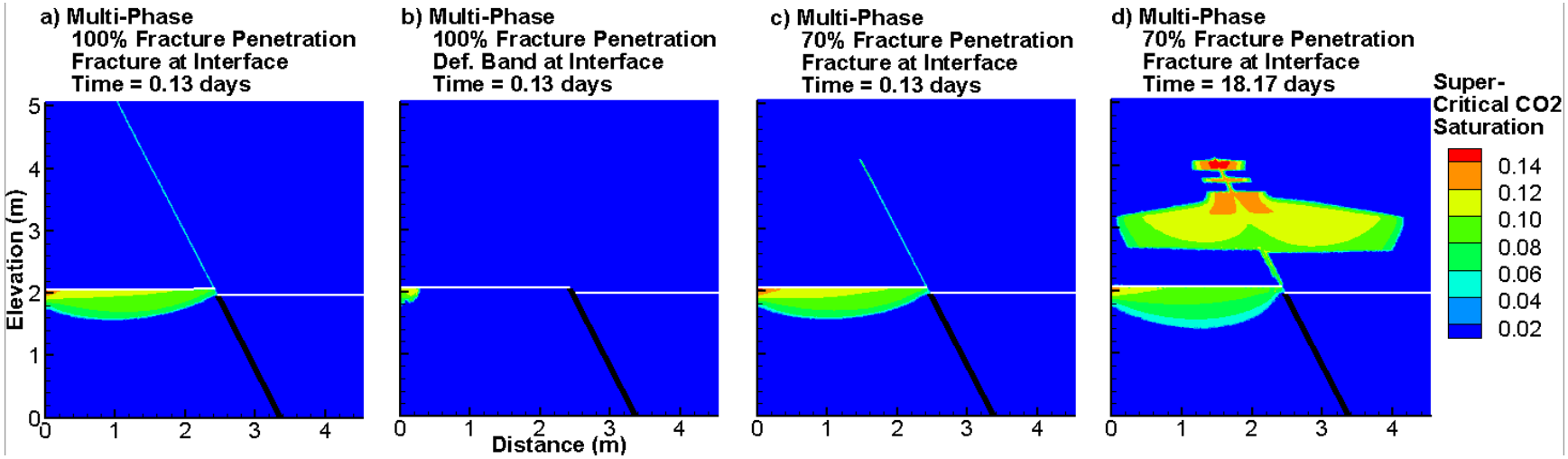

Figure 1. Calculated supercritical CO_2 saturation in volume fraction, for the ISS 1 multi-phase models. The horizontal white lines represent the reservoir-caprock interface and the sub-vertical black line represents the deformation-band fault. CO_2 bypasses the caprock when the fracture is at the interface offset (a). CO_2 does not enter the fracture when the deformation-band fault is at the interface offset (b). CO_2 is confined to the fracture at early time, when the fracture penetrates 70% of the caprock thickness (c). CO_2 has flowed laterally into relatively high permeability facies in the caprock at late time, when the fracture penetrates 70% of the caprock thickness (d).

As observed in the single-phase results, removing the permeable fracture at the reservoir-caprock interface has a profound effect on computed pressure patterns. In Figure 43b, the deformation-band fault is at the interface offset. This simulation shows significant pressure compartmentalization. Almost all of the lateral pressure change occurs across the deformation-band fault. The lateral pressure gradient across the deformation-band fault is 251%. The lateral pressure gradient to the left of the deformation-band fault is 0.56%, while the gradient to the right is 0.14%. Left of the deformation-band fault the horizontal CO_2 velocity (v_x) is 2.7×10^{-5} m/s. Within the main caprock fracture, the pressure is 19.79 MPa and the vertical CO_2 (v_z) is 0 m/s. Everywhere else, the CO_2 velocity is 0.0 m/s. The failure envelope extends over the whole reservoir left of the deformation band. It does not extend up the caprock fracture due to the presence of the deformation band fault at the interface offset.

As observed in the single-phase results, reducing the caprock fracture penetration to 70% of the caprock thickness creates a bottleneck for flow. The top of the fracture is encased in relatively low permeability caprock facies. The geometry of the fracture at the reservoir-caprock interface is the same as Figure 43a. The lateral pressure gradient to the left of the deformation-band fault is 4.3%, while the gradient to the right is 0.2%. Left of the deformation-band fault the horizontal CO_2 velocity (v_x) is 5.5×10^{-4} m/s. Within the main caprock fracture, the pressure is 19.77 MPa and the vertical CO_2 velocity (v_z) is 7.1×10^{-4} m/s. Everywhere else, the CO_2 velocity is 0.0 m/s. It should be noted that water in the fracture, displaced by the CO_2, flows laterally into the caprock. The failure envelope extends over the whole reservoir left of the deformation band. It does not extend up the caprock fracture due to the lower pressure within the fracture resulting from the partial caprock penetration.

The simulation presented in Figure 43d is nearly identical to Figure 43c, except for a difference in time. This model was run for 18.17 days while the rest of these models were run for 0.13 days. This “late time” simulation depicts greater lateral pressure propagation into the relatively high permeability caprock facies than observed in the “early time” simulation. The pressure gradient to the left of the deformation-band fault is 4.3%, while the gradient to the right is 0.2%. Left of the deformation-band fault the horizontal CO_2 velocity (v_x) is 5.8×10^{-4} m/s. Within the main caprock fracture, the pressure is 19.78 MPa and the vertical CO_2 velocity (v_z) is 6.6×10^{-4} m/s. The lateral CO_2 velocity into the permeable caprock facies is 1.4×10^{-6} m/s. Everywhere else, the CO_2 velocity is 0.0 m/s. The failure envelope extends over the whole reservoir left of the deformation band and up into the caprock. It spreads into layers of relatively high permeability within the caprock (Fig. 44d).

Next, we consider the effects of these three different fault zone scenarios on CO_2 transport (Fig. 44). The first three simulations are presented at 0.13 days; the fourth simulation is presented at 18.17 days. CO_2 was introduced (specified saturation) at the upper ten nodes of the reservoir unit, along the up-gradient side of the solution domain.

It should be noted that in all of the model scenarios, both CO_2 and water are migrating in the area of the CO_2 plume. Both CO_2 and water exist anywhere that the CO_2 saturation is not zero or one.

The geometry variations in Figure 44 are the same as the variations described for Figure 43. In all simulations, the CO_2 is restricted to the top of the reservoir. This is likely due to the focusing effects of the deformation-band fault, the hydrostatic pressure assigned to the top of the fracture, and the buoyancy of CO_2, although the influence of buoyancy is small compared to the influence of the specified pressures. In Figure 44a, the CO_2-water mixture flows towards and then up into the main fracture. Within the main caprock fracture, the CO_2 saturation is 0.06.

When the deformation-band fault is present at the interface, CO_2 does not enter the fracture after 0.13 days. In Figure 44b, the CO_2-water mixture just begins to enter the system and flow towards the main fracture over the time modeled. Within the main caprock fracture, the CO_2 saturation is 0.

When the top of the fracture is encased in relatively low permeability caprock facies, the CO_2-water mixture begins to invade the more permeable facies of the caprock, over longer times. In Figure 44c, the CO_2-water mixture flows towards and then up into the main fracture, however, it has not yet begun to infiltrate the caprock. Within the main caprock fracture, the CO_2 saturation is 0.06. By comparison, in Figure 44d, the CO_2-water mixture flows towards and up into the main fracture, then infiltrates a number of relatively high permeability facies within the caprock. The CO_2-water mixture flows both to the left and right out of the fracture. In this model the small subsidiary fractures represented in the single-phase model, are not included. Without these subsidiary fractures to focus flow, the CO_2-water mixture flows out of the main fracture in both directions. Within the main caprock fracture, the CO_2 saturation is 0.10. In the surrounding caprock facies, the CO_2 saturation reaches 0.14. The buildup of CO_2 at the top of the fracture is observed because CO_2 is more buoyant that water. This buildup helps drive the CO_2-water mixture into the surrounding caprock facies because the gradient between the fracture and the surrounding caprock increases.

Next, we consider calculated water and CO_2 fluxes in both the horizontal (Fig. 45) and vertical (Fig. 46) directions. The first row of simulations (a-d) in Figures 45 and 46 are the water flux results. The second row of simulations (e-h) are the CO_2 flux results. The first three simulations in each row are presented at 0.13 days; the fourth simulation is presented at 18.17 days.

In Figure 45a, c, and d, water fluxes focus toward the open fracture at the interface offset. In these three simulations, horizontal water fluxes in the reservoir vary from about 5.0×10^{-5} to 1.0×10^{-4} m/s, with fluxes increasing towards the fracture. In Figure 45b, water fluxes do not focus towards the interface offset. In this simulation, horizontal water fluxes in the reservoir also vary from about 5.0×10^{-5} to 1.0×10^{-4} m/s, however fluxes decrease towards the fracture.

In Figure 45e-h, horizontal CO_2 fluxes range from $1.0x10^{-7}$ to $4.0x10^{-7}$ m/s in the reservoir. For each scenario, these fluxes are restricted to the area of the plume. When the deformation band fault is at the interface offset (Figure 45f), lateral fluxes in the reservoir do not occupy a large area; this results from the small extent of the CO_2 plume in this scenario.

In Figure 46a, c, and d, water fluxes focus towards and up into the caprock fracture. In these three simulations where the fracture is at the interface offset, vertical water fluxes in the reservoir vary from about $1.0x10^{-6}$ to $1.0x10^{-3}$ m/s. Up the fracture, the vertical water flux for these three simulations ranges from 0.01 to 1.0 m/s. In Figure b, much less vertical flux of water is observed in the reservoir. The flux up the fracture is lower as well, ranging from about 0.01 to 0.1 m/s.

In Figure 46e, g, and h, vertical CO_2 fluxes are observed in the caprock fracture. The vertical CO_2 fluxes for these simulations ranged from $1.0x10^{-6}$ to $1.0x10^{-4}$ m/s. The fluxes are primarily observed within the caprock fracture. In Figure f, no vertical CO_2 fluxes are observed in the fracture.

Whole Section

The Whole Section model was created to investigate the impacts of deformation-band faults and fractures on fluid flow over multiple reservoirs and caprocks. No internal heterogeneities are represented within the caprocks. In Figures 47 and 48 below, the fluid pressure and the supercritical CO_2 saturation calculated by FEHM are presented, respectively.

In Figure 47a, the fracture fully penetrates the caprock and a permeable fracture is at both interface offsets. The pressure gradient to the left of the deformation-band fault is 6.6%, while the gradient to the right is 1.5%. Left of the deformation-band fault the horizontal CO_2 velocity (v_x) is $2.3x10^{-4}$ m/s. Within the main caprock fracture, the pressure is 12.40 MPa and the vertical CO_2 velocity (v_z) is $4.5x10^{-3}$ m/s. Everywhere else, the CO_2 velocity is zero because the CO_2 fluid phase is absent.

Unlike the results from ISS 1, removing the permeable fracture at the reservoir-caprock does not have a profound effect on the computed pressure patterns. A slight increase in pressure compartmentalization is observed, but it is not as obvious as in the ISS 1 models. In Figure 47b, the deformation-band fault is at both interface offsets. The pressure gradient to the left of the deformation-band fault is 4.3%, while the gradient to the right is 3.2%. Left of the deformation-band fault the horizontal CO_2 velocity (v_x) is $1.5x10^{-4}$ m/s. Within the main caprock fracture, the pressure is 12.39 MPa and the vertical CO_2 velocity (v_z) is 0 m/s. Everywhere else, the CO_2 velocity is 0.0 m/s.

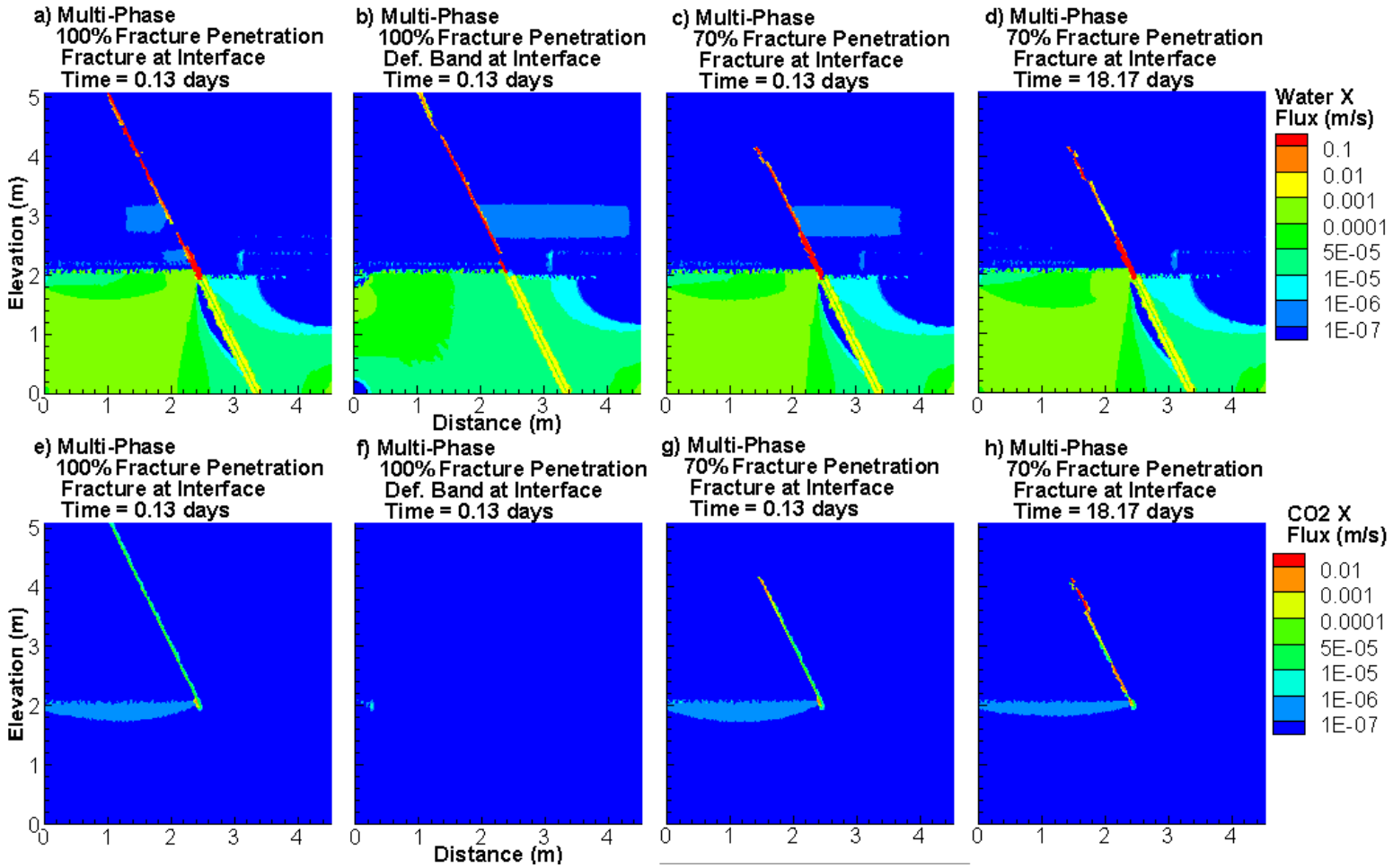

Figure 45. Calculated water and CO_2 fluxes in the X or horizontal direction. Horizontal Water fluxes (m/s) are shown in a-d. CO_2 X fluxes (m/s) are shown in e-h. Water can be seen flowing toward the caprock fracture (a-d). Larger water fluxes into the caprock fracture are recorded when fracture is at the interface offset (a,c,d). Note the horizontal CO_2 fluxes constrained to the area of the plume (e-h). Larger CO_2 fluxes are calculated when fracture is at the interface offset (e,g,h).

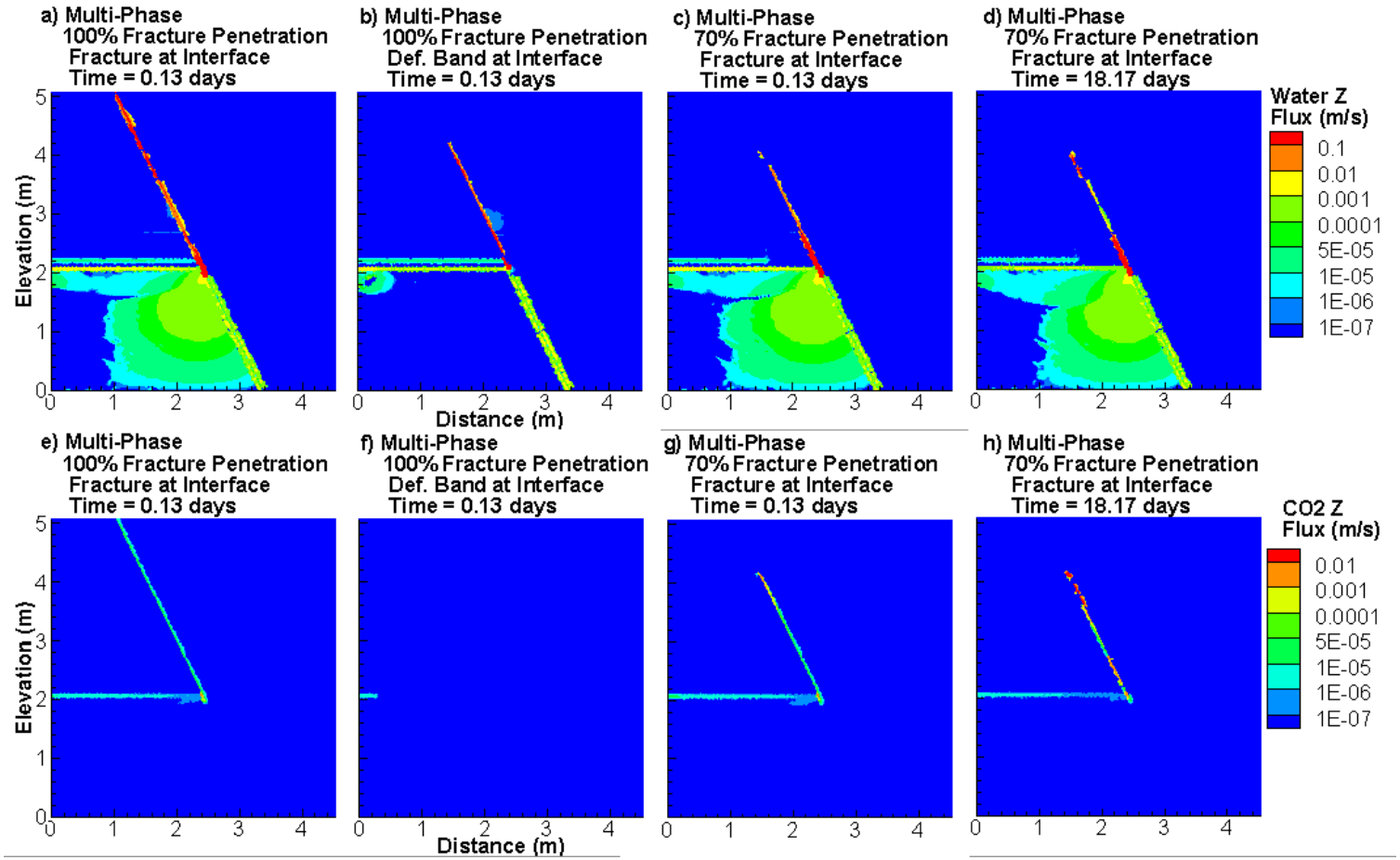

Figure 46. Calculated water and CO_2 fluxes in the Z or vertical direction. Vertical water fluxes (m/s) are shown in a-d. CO_2 Z fluxes (m/s) are shown in e-h. Water can be seen flowing toward and up the caprock fracture (a). Larger water fluxes into the caprock fracture are recorded when fracture is at the interface offset (a,c,d). Slightly lower fluxes are recorded when deformation band is at the interface offset (b). Vertical CO_2 fluxes are primarily up the fracture (e-h). Larger CO_2 fluxes are calculated when fracture is at the interface offset (e,g,h).

Unlike the results from ISS 1, a bottleneck for flow is not readily apparent in Figure 47c. This may be due to the homogeneous caprock used in the Whole Section model. In Figure 47c, the fracture penetrates 70% of the caprock and fracture is at both interface offsets. The pressure gradient to the left of the deformation-band fault is 7.0%, while the gradient to the right is 1.2%. Left of the deformation-band fault the horizontal CO_2 velocity (v_x) is $2.4x10^{-4}$ m/s. Within the main caprock fracture, the pressure is 12.50 MPa and the vertical CO_2 velocity (v_z) is $3.7x10^{-3}$ m/s. Everywhere else, the CO_2 velocity is 0.0 m/s. It should be noted that water in the fracture, displaced by the CO_2, flows laterally into the caprock.

We selected a common simulation time of 29.50 days to display CO_2 transport (Fig. 48). CO_2 was introduced (specified saturation) at the upper 2 nodes of the lower reservoir unit, along the up-gradient side of the solution domain. It should be noted that for these simulations of the Whole Section model, the permeability of the lower reservoir is anisotropic by 100:1 (k_x:k_y). This was done to maintain a relatively thin CO_2 plume. Simulations with isotropic reservoir permeability resulted in calculated CO_2 plumes that extended downward through about 70% of the reservoir.

The geometry variations in Figure 48 are the same as the variations described for Figure 47. In all simulations, the CO_2 is restricted to the top of the reservoir. This is likely due to the focusing effects of the deformation-band fault and the hydrostatic pressure assigned to the sides of the upper reservoir unit. In Figure 48a, the CO_2 flows towards and then up into the main fracture, however, it does not enter the upper reservoir. Within the main caprock fracture, the CO_2 saturation is 0.05, reaching 0.19 at the fracture terminus in the upper reservoir.

When a deformation-band fault is present at the interface offsets, CO_2 does not enter the caprock fracture over the time modeled. In Figure 48b, the CO_2 flows towards the main fracture, but it does not access the fracture. Within the main caprock fracture, the CO_2 saturation is 0.

Unlike the ISS 1 models, the caprock units in the Whole Section models are homogeneous, thus CO_2 does not invade the caprock. In Figure 48c, the CO_2 flows towards and then up into the main fracture. Due to the partially penetrating fracture the CO_2 does not enter the upper reservoir. Within the main caprock fracture, the CO_2 saturation is 0.05, reaching 0.16 at the fracture terminus in the caprock.

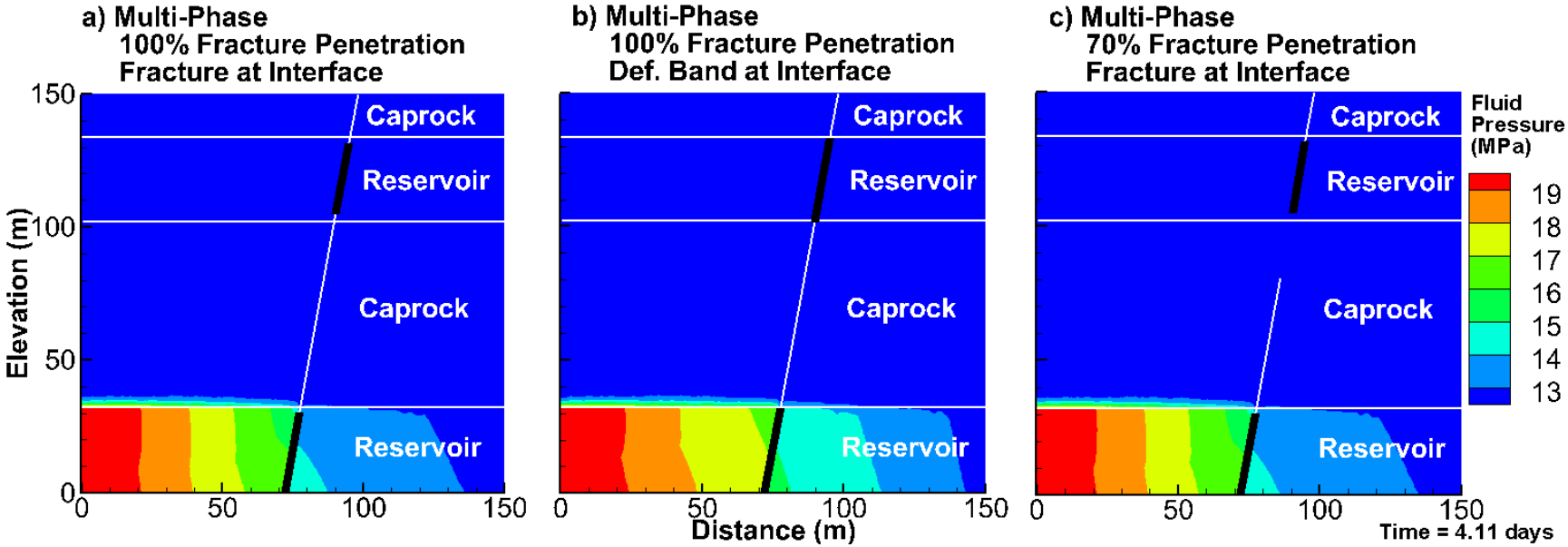

Figure 47. Calculated fluid pressure in megapascals, for the Whole Section multi-phase models. The horizontal white lines represent the reservoir-caprock interfaces and the sub-vertical black and white lines represent the deformation-band faults and fractures, respectively. Compartmentalization is observed when the fracture is at the interface offset (a). Slightly greater compartmentalization is observed when the deformation-band fault is at the interface offset (b). Compartmentalization similar to part a is observed when the fracture penetrates 70% of the caprock thickness (c).

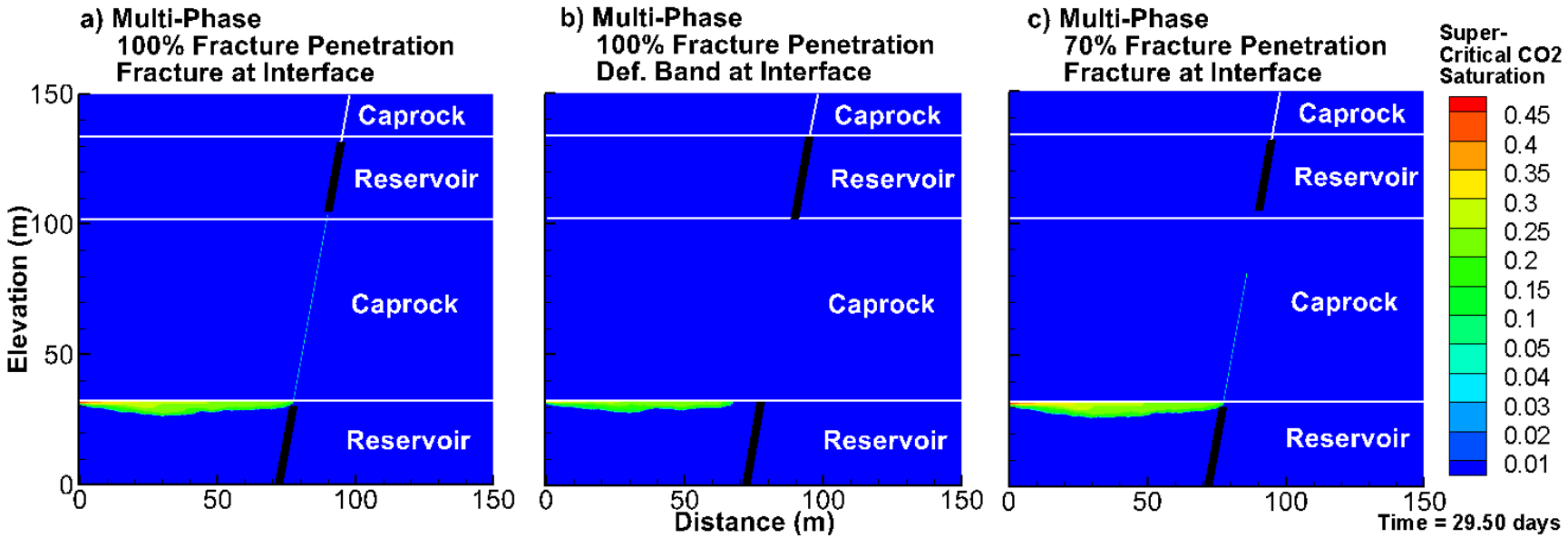

Figure 48. Calculated supercritical CO_2 saturation in volume fraction, for the Whole Section multi-phase models. The horizontal white lines represent the reservoir-caprock interface and the sub-vertical black and white lines represents the deformation-band faults and fractures, respectively. CO_2 bypasses the lower caprock when the fracture is at the interface offset (a). CO_2 does not enter the fracture when deformation-band fault is at the interface offset (b). CO_2 is confined to the fracture when the fracture penetrates 70% of the caprock thickness (c).

Description of Mt. Simon Eau Claire Core

We conducted a detailed petrographic and petrophysical analysis of the Mt. Simon and Eau Clair Formations in the core. For the sake of brevity we only present a few highlights here.

Deformation features

No significant deformation features were observed during examination of numerous outcrops of the Mount Simon/Eau Claire contact by PI Evans and Brenda Bowen (personal communication). However, the Mt. Simon/Eau Claire core that we examined contains numerous opening-mode fractures (Fig. 49), but no deformation bands. Many are filled with gypsum and to a lesser extend anhydrite and barite. The fractures are distributed at various levels within the core, but do not cut the reservoir/caprock interface. Fracture formation occurred prior to precipitation of barite, gypsum, and anhydrite cements, some compaction, and late-stage dissolution of feldspar and gypsum (Fig. 50).

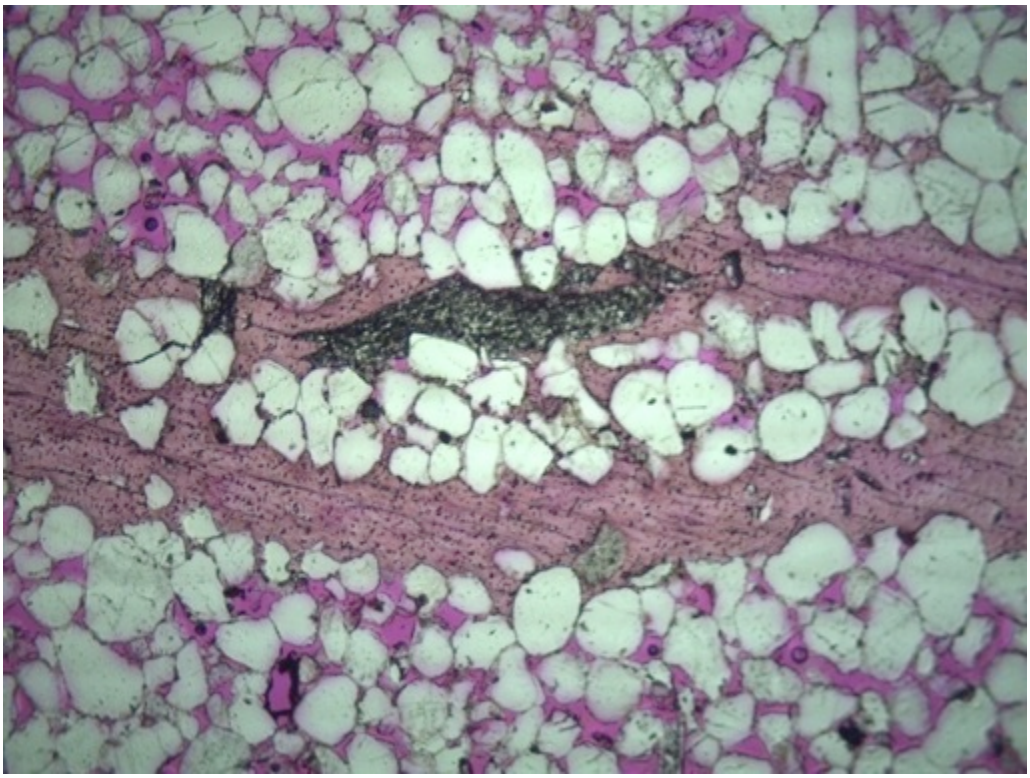

Figure 49. Thin-section photomicrograph showing opening-mode fracture filled with gypsum and barite. Note that these cements are confined to the fractures and do not extend into the surrounding porous sandstone. This suggests that a more soluble cement (halite?) may have been present in the surrounding sandstone at the time that gypsum and barite precipitated. 2931.10 ft, Photo width = 4.2 mm.

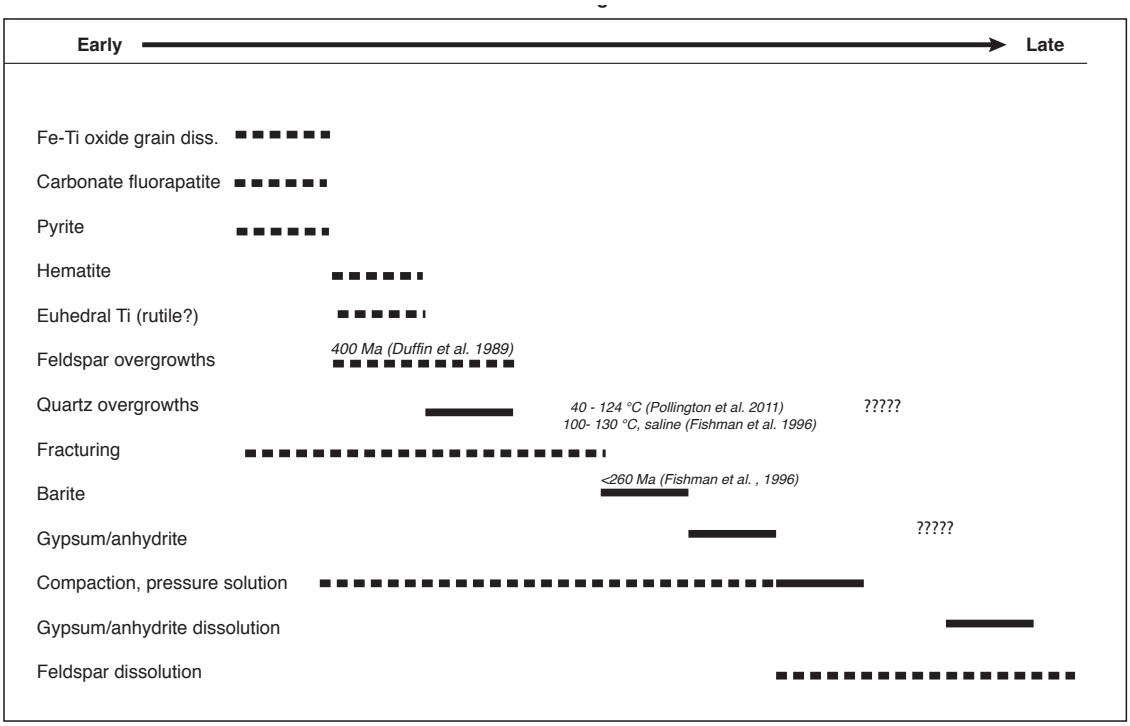

Figure 50. Relative timing of diagenetic alterations influencing the Mount Simon Sandstone. Solid lines indicate the period during which an event occurred, dashed indicate a range of time over which the event may have occurred. Relatively early events are plotted towards the left, late towards the right. Constraints on the age of authigenic feldspar overgrowths and temperature of precipitation of quartz overgrowths are indicated from the cited studies in the Illinois Basin.

Mercury Porosimetry Data

The size distribution of pore throats in the samples is highly variable. Broadly speaking, most samples can be placed into one of three main groups based upon the dominant pore-throat size. These three groups are: mesopore-macropore-throat dominated (4 - 40 micron diameter), micropore-throat dominated (<0.004 - 0.07 microns), and an intermediate group (0.15 - 1.2 microns), which in terms of nomenclature also classifies as micropore-throat dominated (see Nelson, 2009 for a discussion of pore-throat classification; Figs. 51, 52, 53, and 54). A fourth group is characterized by no dominant pore-throat size, but rather a relatively uniform distribution of sizes. One sample is bimodal, with weak modes in both micro and macropore ranges. All of the micropore-throat dominated samples are from the Eau Claire Formation, whereas all of the macropore and mesopore dominated samples are from the Mt. Simon Sandstone. The intermediate micropore throat and evenly distributed types are present in both units.

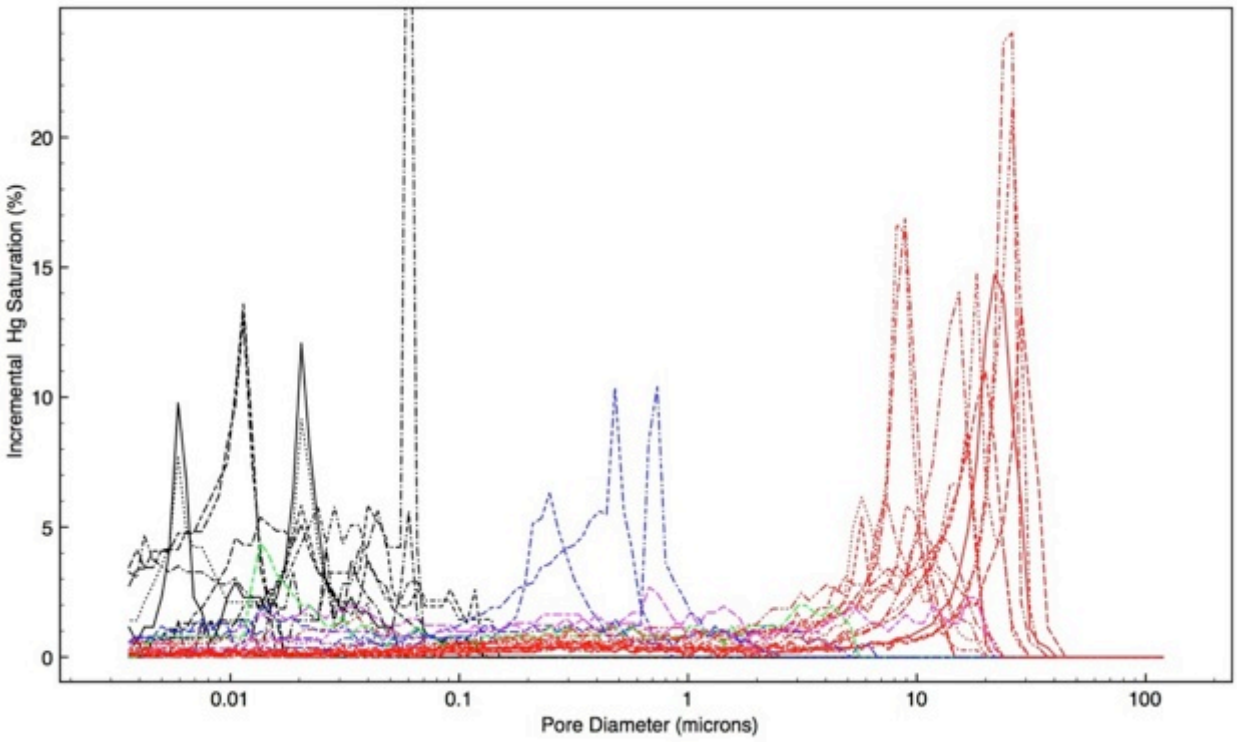

Figure 51. Plot of incremental mercury saturation versus pore-throat diameter for samples from the Eau Claire Formation and Mt Simon Sandstone. Samples can be subdivided into four groups based on pore-size characteristics: macropore dominated (red), micropore dominated (black), intermediate (blue), and evenly distributed (magenta). One sample exhibits an unusual bimodal distribution (green), with populations of both micro and macropores. All of the micropore-throat dominated samples are from the Eau Claire Formation, all of the macropore dominated samples are from the Mt. Simon Sandstone, and intermediate and evenly distributed types occur in both units.

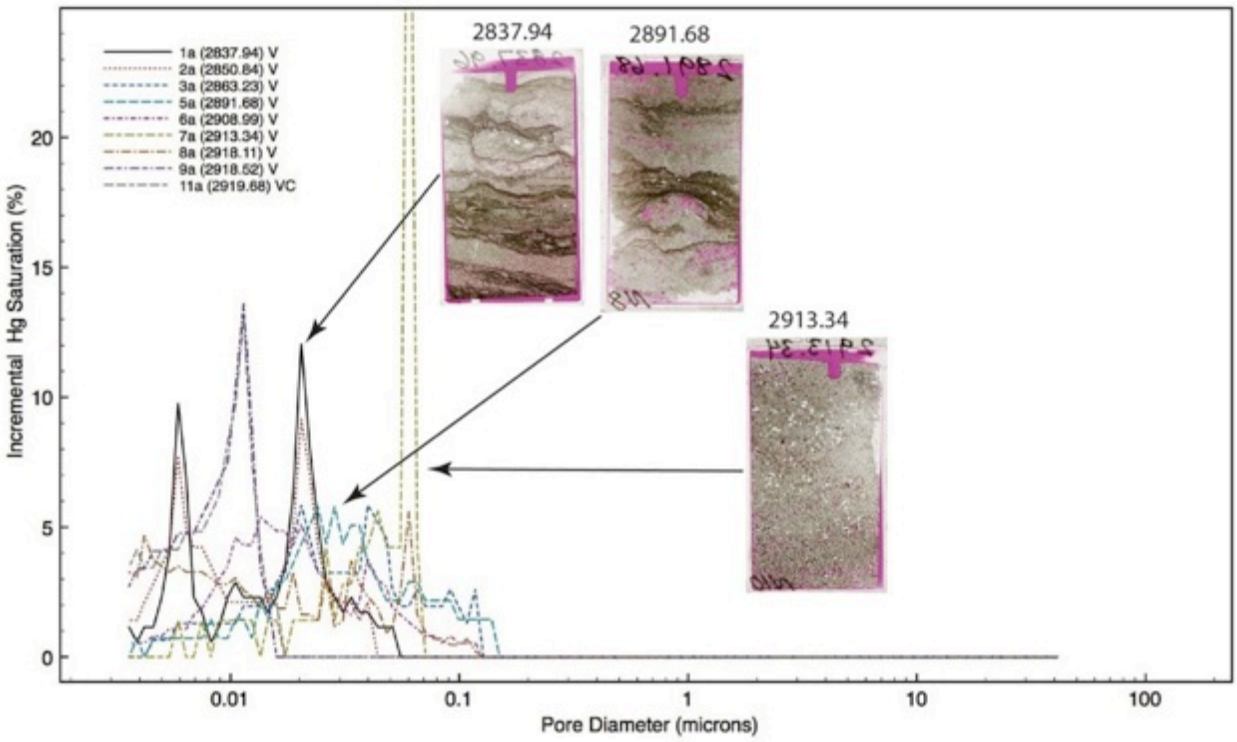

Figure 52. Plot of incremental mercury saturation versus pore-throat diameter for samples in the micropore-throat dominated group. Scans of thin sections from selected samples are shown, in which porosity is highlighted by red-dyed epoxy.

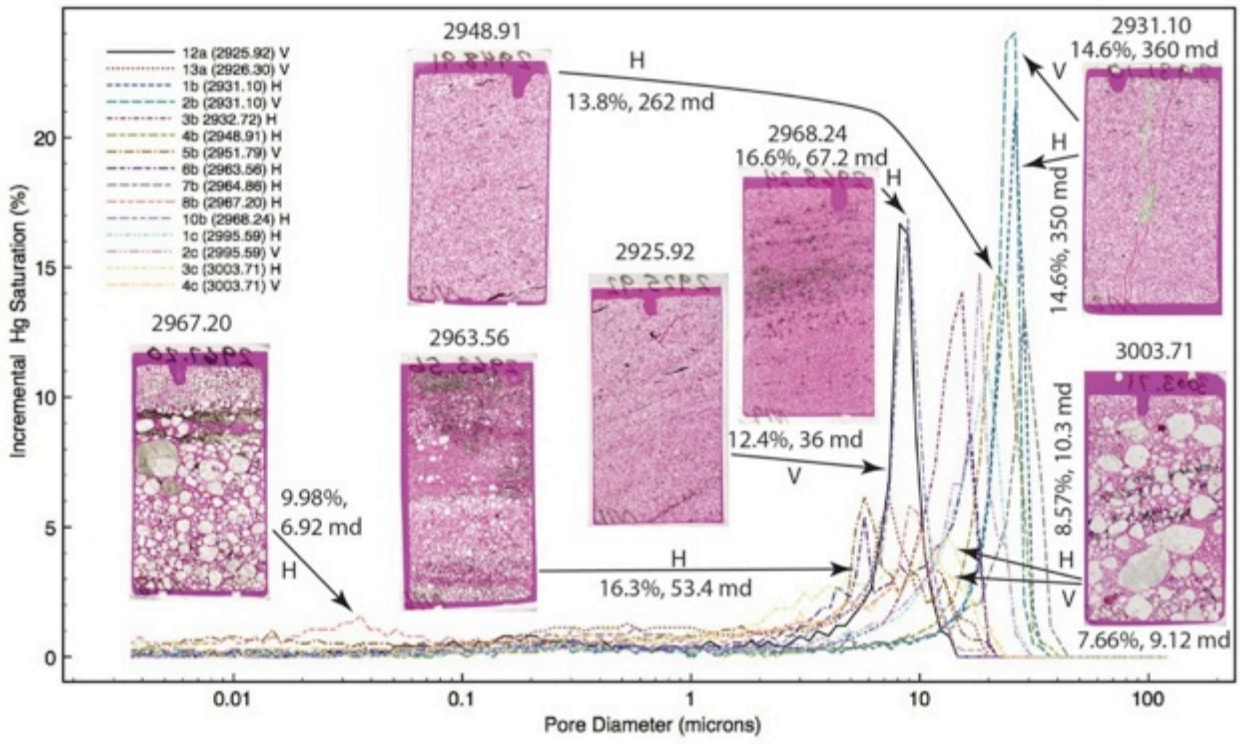

Figure 53. Plot of incremental mercury saturation versus pore-throat diameter for samples in the mesopore-macropore-throat dominated group. Scans of thin sections from selected samples are shown, in which porosity is highlighted by red-dyed epoxy. Measured porosity (%), calculated permeability (md), and orientation of measurement (H = horizontal, V = vertical) are indicated for each sample.

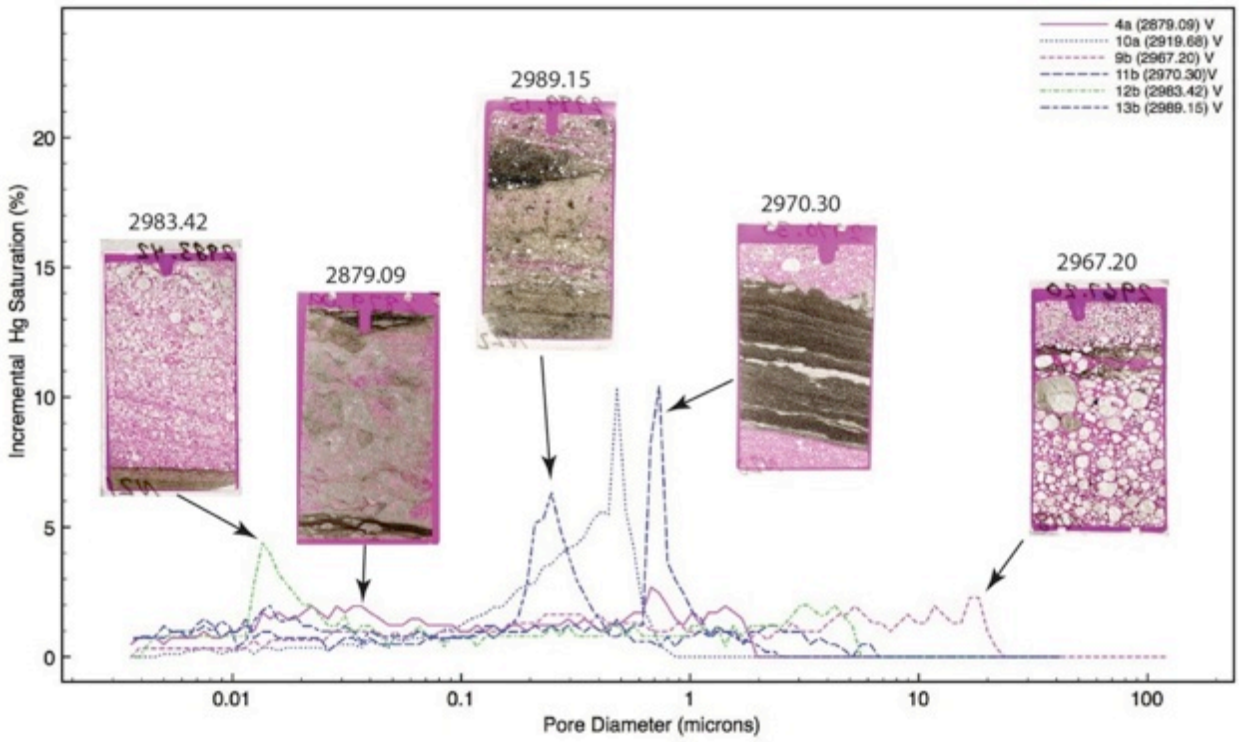

Figure 54. Plot of incremental mercury saturation versus pore throat diameter for samples in the intermediate (blue), evenly distributed (magenta), and bimodal (green) groups. Scans of thin sections from the samples are shown, in which porosity is highlighted by red-dyed epoxy. Note heterolithic nature of the samples.

The micropore-throat dominated samples fall into three broad categories, those characterized by a single dominant pore-throat size, those with a bimodal pore-throat size, and those characterized by a broad range of pore-throat sizes (Fig. 52). Although many of these samples contain abundant macroporosity, it does not appear in the mercury porosimetry data, which indicates that the scale of the porous domains must be smaller than that of the plugs analyzed (i.e., it is not effective porosity). This can be clearly seen in thin section, where macroporosity occurs in poorly interconnected subdomains (Fig. 55). The variability in pore-throat size distribution reflects the considerable textural heterogeneity of the samples, including heterogeneities imparted by depositional texture, as well as variable distribution of pore-filling cements.

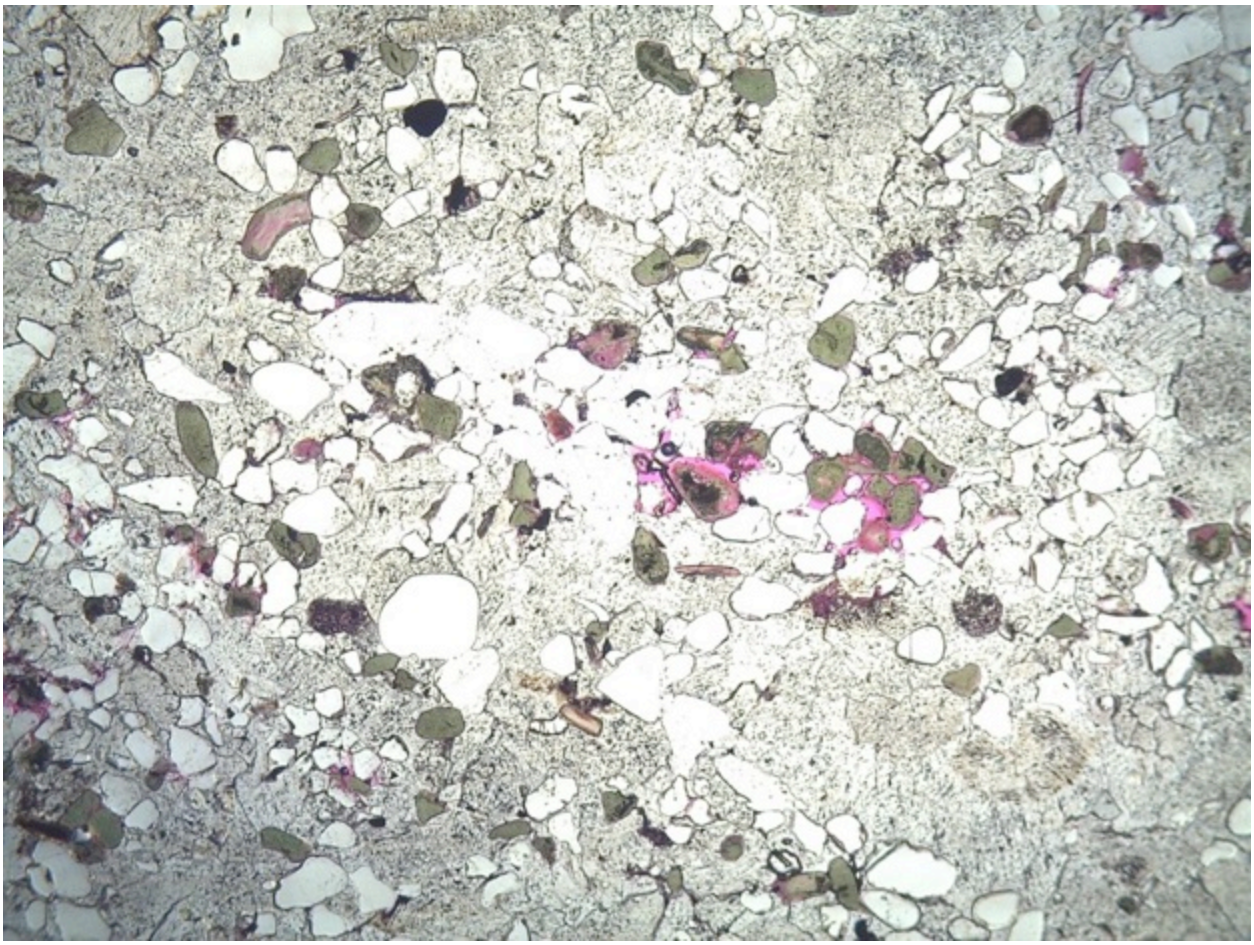

Figure 55. Thin-section photomicrograph showing distribution of porosity in a dolomitized glauconitic limestone. Porosity is highlighted by red-dyed epoxy. Zones of macroporosity are separated by regions in which porosity has been destroyed by quartz and dolomite cements, greatly reducing the effective pore-throat size of the sample. PPL, Eau Claire Formation, 2913.34 ft. Photo width 4.2 mm

The mesopore-macropore throat samples fall into two main distributions: those that are characterized by a single dominant pore-throat size, and those that have a broader distribution of sizes with several modes (Fig. 53). There is a clear primary textural influence on the two populations, with the former type occurring in lithologically and texturally homogeneous samples, and the latter type occurring in texturally and lithologically heterogeneous samples.

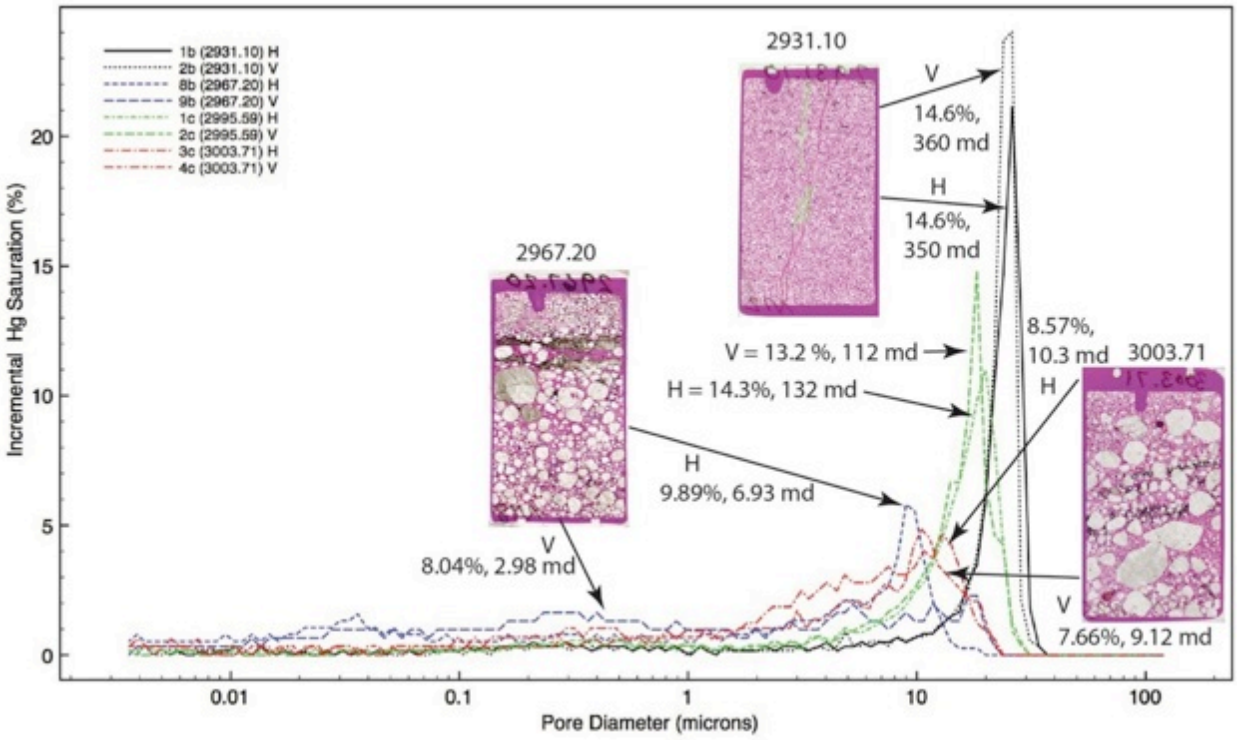

Figure 56. Plot of incremental mercury saturation versus pore-throat diameter for samples in the macropore throat dominated group for which horizontal and vertical measurements are available. Scans of thin sections from selected samples are shown, in which porosity is highlighted by red-dyed epoxy. Measured porosity (%), calculated permeability (md), and orientation of measurement (H = horizontal, V = vertical) are indicated for each sample.

For a subset of four of the mesopore-macropore dominated samples, mercury injection data was collected for both horizontally and vertically oriented jacketed core plugs (Fig. 56). For all but one of the sample pairs, the measured porosity is slightly greater for the horizontally oriented samples than the vertically oriented samples. This suggests that portions of the samples were not fully saturated with mercury during most of the vertically oriented runs. Because textural and lithologic heterogeneity is greatest in the vertical direction in most of the samples, this difference in accessible pore volume may result from three-dimensional effects in which zones of porosity are enclosed by very-small-pore-throat domains. This interpretation is strengthened if we consider the sample exhibiting the greatest difference in horizontal and vertical pore-throat size distribution. For three of the four paired samples the pore throat size distribution did not differ significantly between horizontal and vertical analyses; however, for sample 2967.20 ft, the horizontally oriented plug shows a distinct 9-micron pore throat diameter peak, whereas the vertically oriented plug shows a relatively evenly distributed pore-size distribution with no clear peaks. Sample 2967.20 ft is the most lithologically heterogeneous of the four samples, containing conglomerate, sandstone, and mudstone. In addition, zones of relatively large macropores are bounded above and below by thin mudstone laminae. Such zones would have been accessible to mercury injected

horizontally, but are less likely to have been accessed by vertical injection due to the bounding mudstone. Finally, one of the four samples, 2931.10 ft, exhibits no difference in porosity between the horizontal and vertical analyses. This sample has the least textural heterogeneity of the four samples. However, it is cut by a gypsum filled fracture that apparently did not influence the measurements. This is likely due to the fact that the gypsum fracture fill only traverses about 60% of the sample, allowing ready access of mercury to both sides of the fracture. In conclusion, the results for paired directional samples indicate that the measured porosity for many, perhaps most, of the vertically oriented measurements underestimate the total sample porosity. In addition, given the clear textural control on the pore-throat results, and the high degree of lithologic and textural heterogeneity of many of the samples, a portion of the vertically measured samples that exhibit no clear pore-throat peak probably would if measured horizontally.

Samples exhibiting intermediate, evenly distributed, and bimodal distributions in pore throat diameters have one thing in common, they are all texturally and lithologically heterogeneous, with greatest heterogeneity in the vertical direction (Fig. 54). All of these samples were measured in the vertical direction, thus, given the apparent influence of sample orientation discussed above, it is likely that the measured values were influenced by this vertical heterogeneity, and that if measured horizontally, the results may have been considerably different. Data for one of the samples, 2976.20 ft, supports this contention. This sample was measured both vertically and horizontally. The horizontal measurement produced a pore-throat size distribution in the mesopore-macropore-throat category, whereas the vertical measurement placed it in the evenly distributed category. Finally, the sample exhibiting a bimodal pore-throat distribution (2983.42 ft) appears to have been dramatically influenced by this vertical heterogeneity. It consists of interlayered sandstone and mudstone (Fig. 54). Two populations of pore sizes are evident, with a major peak in the micropore throat range and a weaker peak in the mesopore throat range. The sample is heterolithic, mainly consisting of sandstone (about 90%) with a layer of mudstone at its base. Although sandstone makes up the majority of the sample, it appears that the thin mudstone layer formed a continuous barrier in the jacketed sample, controlling mercury injection and providing a skewed analysis of overall pore-throat size distribution.

D. Discussion

Environment of formation of caprock fracture networks

When using outcrop analogues is necessary to demonstrate that features examined are representative of features that are of significance in the subsurface environment. Of particular concern in the present study was assuring that the fracture networks that we describe in outcrop are not the result of near-surface weathering. Observations made in outcrop, through petrographic analysis, and geochemical analyses of fracture filling material all indicate that the fractures did not originate through near surface weathering.

Specific evidence includes: (1) Bleaching of fracture margins (i.e., hematite dissolution). Such chemical bleaching is widespread on the Colorado Plateau and is ascribed to the transmission of chemically reducing fluids through the fractures at depth, in some cases associated with hydrocarbon migration (Garden et al., 2011). (2) As noted above, pyrite and pyrite pseaudomorphs are present in the fractures. Pyrite only forms under strongly reducing conditions, not in the highly oxidizing environment of near surface outcrop weathering. (3) Calcite fracture fill is Fe-enriched (Raduaha, 2013), also an indication of reducing conditions.

Implications of interface features for subsurface flow and transport

Numerical modeling of the interface features at ISS-1 provides quantitative constraints which allow assessment of the potential impact of such features on flow of supercritical CO2 at storage sites. Based upon our detailed work in outcrop, we constructed conceptual permeability models which formed the basis for this investigation. We also produced larger scale "whole section" models to assess the impact of the observed features at greater length scales.

In both the ISS 1 single- and multi-phase models, for all scenarios considered, reservoir compartmentalization was observed to some degree. The calculated head pattern varies depending on the geometry of the interface offset. When the reservoir directly contacts the fracture, calculated anomalous pressures are compartmentalized behind the deformation-band fault. A head gradient of approximately 200% was measured across the deformation-band fault in the single-phase model. The flow was focused up toward the top of the reservoir at the intersection with the open fracture, which served as an outlet. By contrast, when the reservoir does not contact the fracture, the area to the left of the deformation-band fault is of a nearly uniform high pressure. A head gradient of 0.53% was measured across the reservoir in the single-phase model. Flow dissipated across the caprock and the deformation-band fault. We conclude that these small changes at the interface offset drastically affect flow paths in all of the models. It seems that the geometry and properties of the small interface offset are key to flow patterns in these systems.

When the caprock fracture penetrates only 70% of the caprock thickness, some compartmentalization is apparent, but pressure appears to “bleed off” into the caprock along the open fracture through more permeable caprock facies. A head gradient of 0.58% was measured across the reservoir in the single-phase model. The greatest solute and CO_2 transport was observed when the fracture terminated below the top of the seal and solutes leaked into the more permeable caprock facies. This seems to indicate that most, if not all, of a caprock must be penetrated by a fracture before significant bypass will occur.

The calculated failure envelopes show that the compartmentalization which occurs in our models may lead to the failure of critically stressed faults in the same region

of the reservoir and cap rock. It seems that the re-activation of faults along zones of weakness, for example cemented fractures like those observed in the field (Raduha, 2013), is quite likely in areas where deformation-band fault/fracture systems intersect the reservoir-caprock interface. The pressure buildup behind deformation-band faults directly juxtaposed against a fracture seems to be an ideal scenario for fault failure.

While some pressure compartmentalization was observed in the Whole Section models, it was not as pronounced as the compartmentalization observed in the ISS 1 models. This is likely due to grid-discretization effects. However, it is still apparent that when a deformation-band fault is at the interface offset greater pressure compartmentalization occurs.

When caprock heterogeneity is incorporated, solutes and supercritical CO_2 propagate into comparatively high permeability units within the caprock. This suggests that caprocks may be capable of storing large quantities of CO_2 near the injection well when open fracture networks allow flow into the caprock.

Using the fluxes, saturations, and concentrations discussed above, mass-balance calculations were performed, for the fracture at the interface offset and the 70% fracture penetration cases, for the single- and multi-phase models of ISS 1. For the single-phase ISS 1 model, nearly 100% of the solute mass entering the reservoir, when an open fracture is at the interface offset, exits at the top of the fracture at 14.6 days. When the fracture penetrates 70% of the caprock thickness, approximately 60% of the injected solutes enter the permeable caprock facies. In the multi-phase models, when an open fracture is at the interface offset, nearly 100% of the injected CO_2 exits the system at 0.13 days. When the fracture penetrates 70% of the caprock, nearly 100% of the injected CO_2 enters into the caprock fracture or from the caprock fracture into the permeable caprock facies at 18.17 days.

How do these meso-scale features impact seal performance? A vertical CO_2 flux of 5.0×10^{-6} m/s for ISS 1 was taken as a representative value for supercritical CO_2 losses at the fracture offset. This flux was then converted into a mass flux of 7.2×10^{-6} kg/s. Assuming a constant CO_2 density of 720 kg/m^3 and a length of 1 m in the Y-direction (into the page). This mass flux was then compared to a CO_2 injection of 1Mt/yr, which is the current injection rate at the Sleipner field in the North Sea (Verdon et al., 2013). At this injection rate, one open fracture extending the length of the caprock would leak approximately 23% of the CO_2 injected in one year. This is significantly above the IPCC's seal performance criteria of 0.001% leakage per year (IPCC, 2005). When the deformation band fault is at the interface offset, no CO_2 enters the open fracture over our model time. Therefore, given our parameters, CO_2 leakage in this case would be 0% of the CO_2 injected in one year. It should be noted that CO_2 may enter the fracture over longer time scales and that the leakage rate would likely then increase. When the fracture penetrates 70% of the caprock thickness, CO2 does not bypass the caprock, however, it does flow laterally into units of relatively high permeability within the caprock. A lateral

CO_2 flux of $2.0x10^{-7}$ m/s was taken as a representative value for flow into the relatively permeable caprock units when the fracture penetrates 70% of the caprock thickness. This value was then converted into a mass flux of $1.0x10^{-4}$ kg/s, assuming a constant CO_2 density of 720 kg/m3, a length of 1 m in the Y-direction (into the page), and a permeable unit thickness of 0.7 m in the X-direction (vertically). This was then compared to a CO_2 injection rate of 1 Mt/yr. At this injection rate, all of the CO_2 injected in one year could be stored in the specified portion of the seal.

Deformation-band fault/fracture systems can transport large amounts of CO_2, depending on the geometry of the system. Any proposed CO_2 sequestration site must consider the impact of these features, as it seems that just one these features may have the potential to undermine a sequestration attempt. To fully understand these features, further research must be conducted to determine the geometry of the interface offset in the field, as this location is key to flow at the site. This sensitivity study focused on the effects of permeability heterogeneity on seal by-pass. We assumed that CO_2 entry pressure and saturation-relative permeability relationships were the same for all facies and fractures. Future work should vary these parameters with grain-size. Holtz et al. (2002) present a methodology for varying the parameters with porosity. However, that study only considered coarse-grained facies with sandstone reservoirs.

Spatial distribution and origin of interface structural features

Although our numerical modeling results clearly demonstrate the potential importance of interface structural features on flow and transport in the subsurface, the overall impact of the features depends on their spatial distribution at a given storage site. In order to predict the presence and distribution of such features in at potential sites it is necessary to understand the processes responsible for their formation, and to develop predictive conceptual models of their formation.

Fracture Connectivity and Uniformity

Seal bypass may occur where fractures in sealing lithologies are vertically connected to create fluid migration pathways from the lower reservoir (Shipton et al., 2004; Cartwright et al, 2007; Barton, 2011). Bleached and mineralized fracture walls in the lower Carmel Formation are interpreted to be caused by fluid migration through fractures that are connected to the underlying Navajo Sandstone. The fracture data collected here suggest a relationship between fracture density and fracture connectivity to the reservoir-seal interface. Both fracture sets have fractures with varying degrees of connectivity to the interface. Many fractures are constrained to individual beds in the Carmel Formation. Some fractures transcend bedding contacts, and it is the fractures which extend closer to the interface that are bleached. The fractures that terminates above the interface shows no alteration. Bleached and mineralized fractures are interpreted to be connected to the interface and potentially to fractures in the underlying reservoir. The

nature of the connectivity of the fractures between the Navajo Sandstone and the reservoir rocks stratigraphically above the Carmel Formation is unknown.

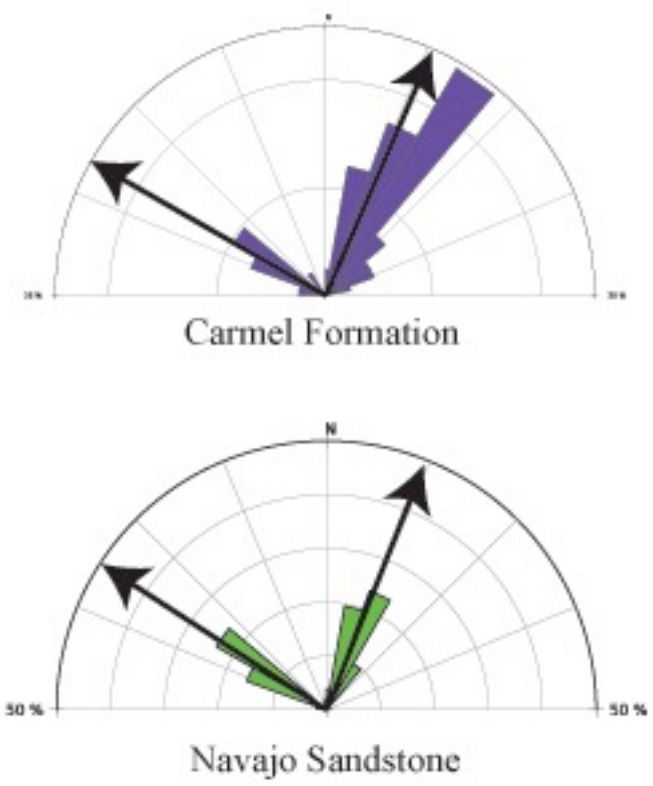

Figure 57. Example of fracture uniformity from Eardley station C. Fractures from sets J1 and J2 have similar strike orientations in the Navajo Sandstone and in the Carmel Formation. The black arrows show the mean strike orientation for each fracture set.

Fracture strike uniformity for a given setting above and below an interface between units may also affect connectivity. The strike of the fracture sets at each station is uniform above and below the interface (Fig. 57), increasing the chance for connectivity between fractures of similar strike (Barton, 2011).

The results of the fracture density from scan lines in the Eardley field site have implications when compared to the geometry of the syncline. High subsurface fracture densities are expected where curvature values are greatest, but the high curvature values are restricted to a smaller cross-sectional length than the places with low curvature values (Fig. 50). The greatest difference in cross-sectional hinge zone length is between stations A and E (Fig. 58).

The hinge zone near station A is expected to have a higher fracture density than station E because it has a smaller radius of curvature (higher curvature). Because of the interplay between fracture density and the cross-sectional length of the hinge zone, the total number of fractures may be greater in hinge zones with larger cross-sectional areas

because the fracture density is present over greater lengths. Though the total number of fractures may be higher, the number of transmissive fractures is likely higher in zones of higher curvatures because fracture connectivity may be related to fracture density. This suggests that a threshold for transmissive fractures may exist along the trend of the syncline axis as curvature and fracture density decrease.

.

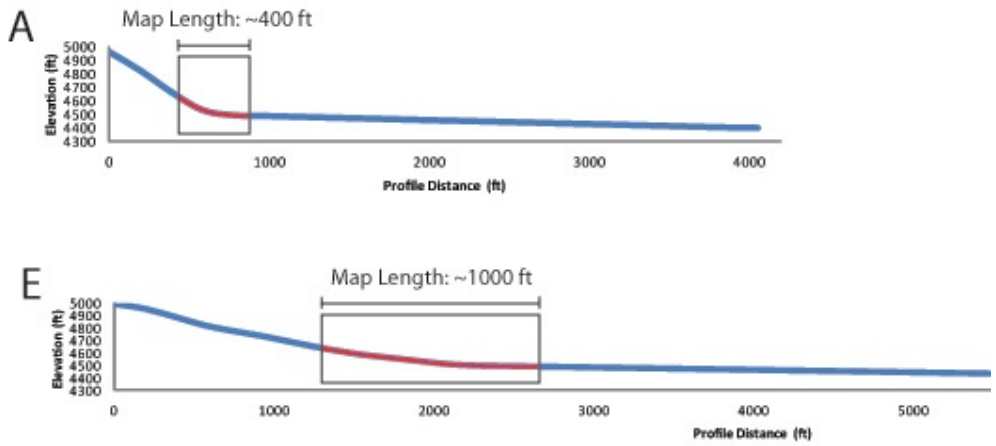

Figure 58. Hinge zone cross section lengths. The zone of strain occurs in a larger area along the syncline where curvature values are smaller.

Modern and Paleostress of the San Rafael Swell

Kinematic indicators and fracture orientations provide insight into ancient and current principal stress orientations, allowing us to infer how tectonic history is related to the development of seal-penetrating fractures. The orientations of the greatest principal stresses has changed significantly over the history of the Navajo Sandstone and Carmel Formation. Currently, the San Rafael Swell straddles the boundary that separates the Basin and Range province from the Colorado Plateau (WSM, 2013; Janecke, unpublished) (Fig. 59). The maximum horizontal stress for the Basin and Range province is generally N/S and extension occurs is the E/W direction. The maximum horizontal stress orientation for the Colorado Plateau, in the vicinity of the San Rafael Swell, is E/W, and extension occurs in the N/S direction. The change in stress orientation occurs near the western margin of the San Rafael Swell and is reflected in the orientation of normal faults (Janecke, unpublished) (Fig. 59).

The stress conditions during the Laramide Orogeny contrast to that of the present-day. The maximum principal stress orientation during the Laramide Orogeny was horizontal (Bird, 1998; Bump and Davis, 2003) characteristic of a compressional tectonic setting. The present-day maximum principal stress direction is vertical as is evident from normal faulting in the Basin and Range Province and the Colorado Plateau (Wong and Humphrey, 2009; WSM, 2013).

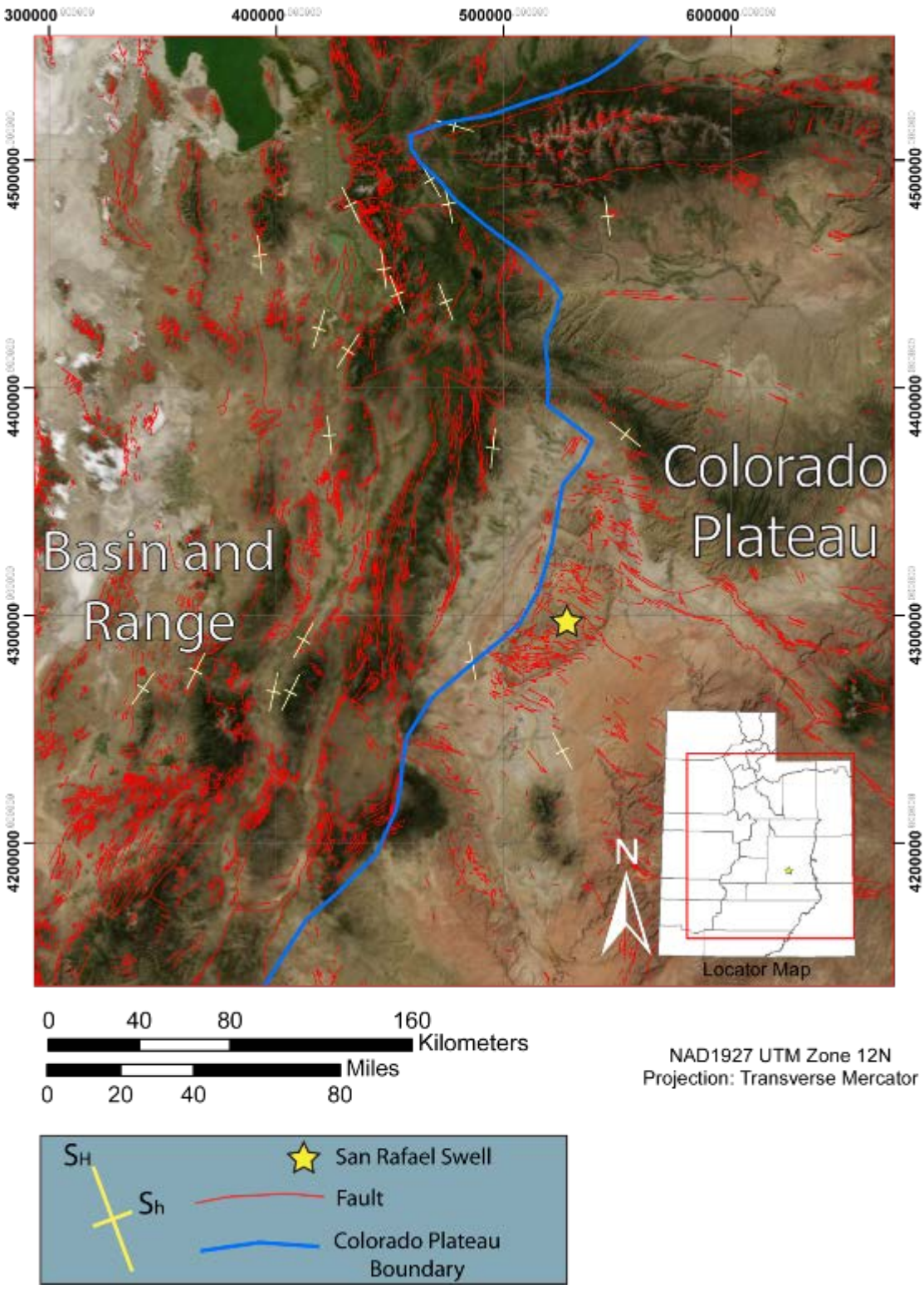

Figure 59. Fault and present-day stress map of central Utah. Modified from UGS, 2002 and WSM, 2008. Colorado Plateau Boundary from Janecke, personal communication 2013.

Structures observed on the eastern flank of the San Rafael Swell record the paleostress orientations present at the time of structure formation. Bump and Davis (2003) use the orientations of deformation bands and slicken-lines found in the San Rafael monocline to determine the maximum horizontal paleostress direction during the formation of the San Rafael Swell (Fig. 60). The orientation of the deformation bands indicate a max horizontal paleostress direction of S60E (120/300 az).

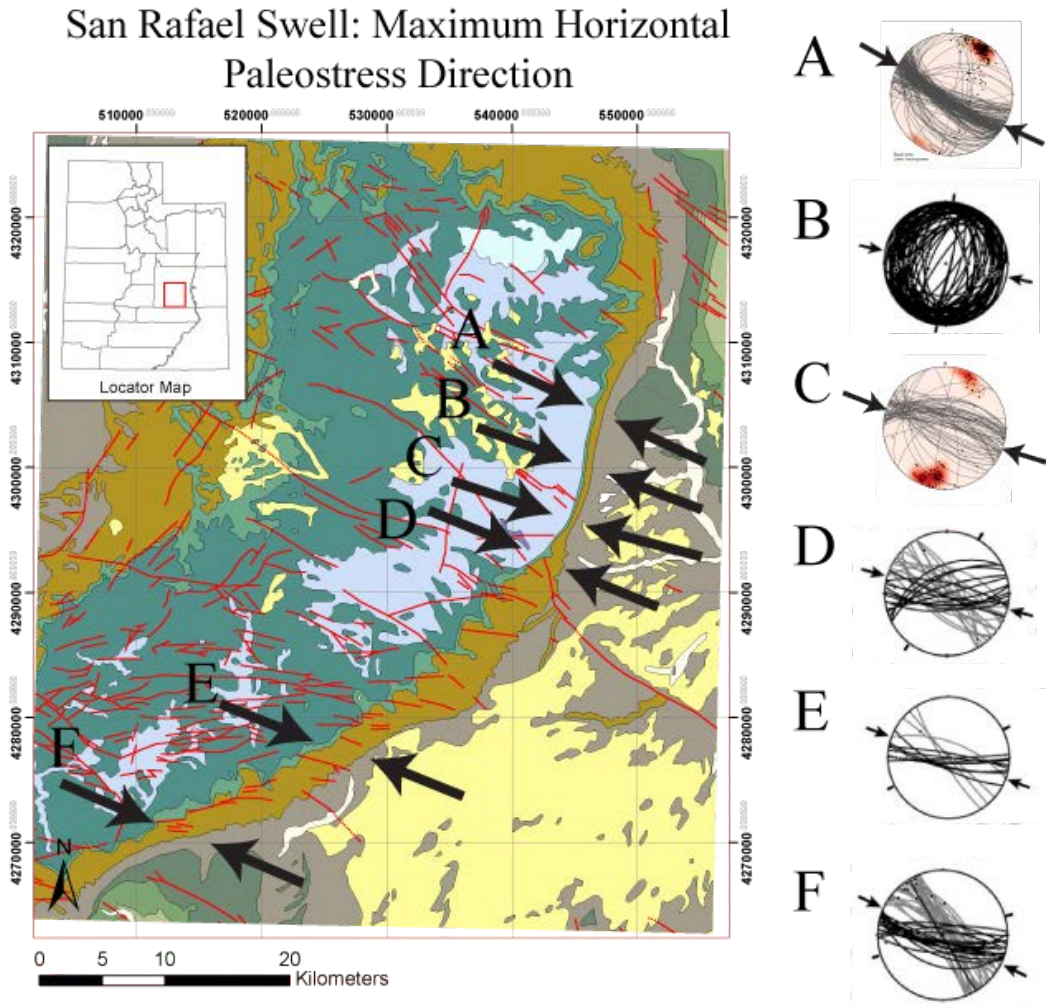

Figure 60. San Rafael Swell with the maximum horizontal paleostress directions labeled with arrows. A and C are from joints in this study, and B, D, E, and F are deformation bands and slicken-lines from Bump and Davis (2003).

T

The joint patterns in the Navajo Sandstone reflect the regional and local stress states. The regional maximum paleo stress orientation during the formation of the San Rafael Swell is a result of Laramide tectonics during the late Cretaceous and early Tertiary (Hawley et al, 1968; Bird, 1998; Bump and Davis, 2003,; Davis and Bump, 2009). The regional joint patterns and orientation data collected in this study match the observations and interpretations of Kelly (1960) and Bump and Davis (2003) and suggest

that the greatest regional principal horizontal stress during the formation of the San Rafael Swell during the Laramide Orogeny was oriented between 125/305az and 120/300az.

A second set of joints, which formed slightly later than the first set, is observed in the Eardley and Orange Stream field sites. The joints have strikes between 000/180az and 025/205az. This joint set is found near the hinge of the San Rafael Swell syncline and contain strike values similar to the trend of the syncline axis (Fig. 61). The second set of joints is slightly oblique (less than perpendicular) to the regional joint set and may represent localized stress related to folding (Fischer and Christensen, 2004).

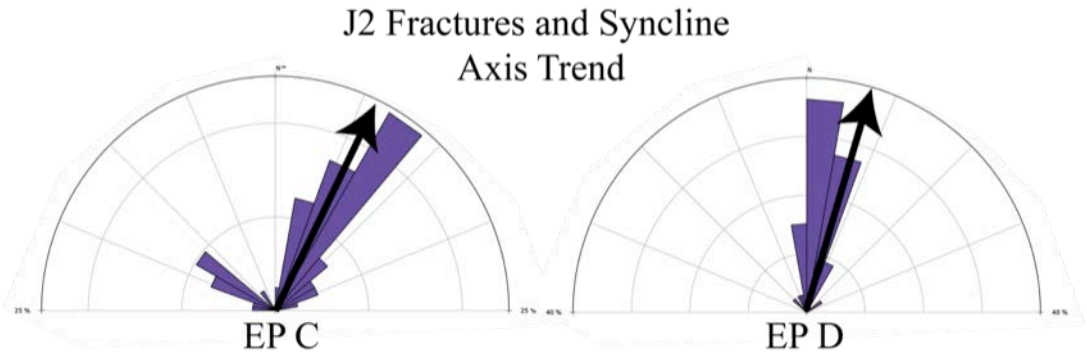

Figure 61. Syncline axis trend compared to J2 fractures from two stations at the Eardley site. The axis trend is represented with black arrows and the. The rose diagrams contain all Carmel Formation fractures from the scan line data. The mean J2 fracture orientation is nearly parallel to the axis trend.

Slip along the subsurface basement fault responsible for the formation of the San Rafael Swell is described as oblique with components of dextral and thrust motion (Bump and Davis, 2003). Kinematic indicators described by Bump and Davis (2003) suggest a maximum horizontal paleostress direction oblique to the fold axis, especially in the southern half of the San Rafael Swell. Near the center of the San Rafael Swell, north of Iron Wash near the Eardley site, the slip on the fault likely transitions to a dominant dip-slip motion as the maximum horizontal paleostress direction is nearly perpendicular to the fold axis. There is likely a minor component of dextral motion to account for the slightly non-orthogonal relationship between the two joint sets.

Significance of the Mount Simon/Eau Claire Observations

As noted above we did not observe any structural features at the reservoir/caprock interface in the core, and none have been reported in outcrop. We did however, observe numerous opening mode fractures in the Mount Simon Formation. These fractures are mostly filled by gypsum cement.

Although we did not observe any deformation bands in the Mount Simon, Chentnik (2012), and undergraduate student supervised by Brenda Bowen, documented

both deformation bands and fractures in the Mount Simon Sandstone in the Illinois basin. This leave open the possibility that deformation band faults in the Mount Simon may intersect the interface in a situation analogous to those we observe on out outcrop analogues. Further work could be pursued on this topic involving careful examination of available core to specifically look for small-scale deformation features that may have been overlooked.

Implications of pore-aperture heterogeneity for fluid flow in the Mt. Simon Sandstone

The mercury porosimetry data for the Mount Simon formation, while not directly relevant to the reservoir/caprock interface, does have implications for the use of the Mount Simon Formation for carbon storage. The pore size and throat distribution of our Mount Simon Sandstone samples are often highly heterogeneous, a reflection of (1) variable IGV due to cement dissolution and (2) primary textural heterogeneity at the thin section scale. The net result of this heterogeneity is that there is a greater than "normal" opportunity for capillary trapping (see Hotlz, 2002; Saadatpoor et al., 2010). The variation in capillary behavior of the middle Mount Simon Sandstone may lead to local regions of higher-than-average (relative to the rest of the formation) capillary trapping of the non-wetting phase. The amount of a non-wetting fluid (e.g., CO_2) in a water-wet system that is held in place by buoyancy due to capillary forces is affected by local variations in local capillary breakthrough pressure (Saadatpoor et al., 2010). When the capillary breakthrough pressure is locally larger than the average of the underlying reservoir rocks (of the same formation), additional capillary trapping can occur. Saadatpoor et al. (2002) note that this trapping mechanism can be much larger than that of residual saturations for a particular rock type. For CO_2 storage local capillary trapping may be desirable as another mechanism that improves over residual-saturation trapping within the target reservoir for CO storage (see Saadatpoor et al., 2010).

E. Conclusions

In this study we examined the potential impact of deformation features at the reservoir/caprock interface on flow and transport of supercritical CO2 in the subsurface. Specifically, we studied the impact of the intersection of deformation band faults in the reservoir that transition to fracture networks in the caprock lithology. Our work relies on exceptionally exposed outcrop analogues present on the eastern side of the San Rafael Swell in Utah. A particular advantage of our analogue sites is that diagenetic alterations affecting the fractures allow us to rule out the possibility that the fractures originated through outcrop weathering (i.e., they are real subsurface features of the sort that could be present at potential storage sites).

A conceptual permeability model generated for a representative analogue interface site was used as input data for single-phase and multiphase flow modeling. A number of significant findings emerged from this modeling, including:

(1) Deformation-band faults can compartmentalize flow in a reservoir by providing a barrier to cross-fault flow. This is in large part due to the intersection of the deformation band faults with the interface, which inhibits flow around the upper tip of the fault.

(2) The small-scale properties of the interface offset have a huge impact on flow through the system. When an open fracture is at the interface offset, as opposed to deformation-band fault, flow velocities in the single-phase models were higher by two orders of magnitude in the permeable caprock fracture ($3.0x10^{-4}$ m/s compared to $3.0x10^{-6}$ m/s). Higher amounts of transport into the fracture were also observed by measuring normalized solute concentration and CO_2 saturation in the fracture. With an open fracture at the interface, a concentration of 0.08 was measured in the fracture. By contrast, when a deformation-band fault is at the interface offset, a concentration of 0 was measured. Similar results were found for the multi-phase results, where CO_2 saturations of 0.06 and 0.00 were observed for the two cases, respectively.

(3) Fracture penetration through the caprock plays a deciding role in seal bypass. Two cases were considered to determine the influence of fracture penetration through the caprock on flow and transport in the system: 1) 100% fracture penetration through the caprock and 2) 70% fracture penetration through the caprock. It was observed in both the single- and multi-phase results of the smaller scale ISS 1 model, which included both high and low permeability caprock facies, that fluids charged the caprock when the fracture penetrated 70% of the caprock thickness. This was due to the heterogeneous permeabilities modeled in the caprock, which were based on field observations of caprock lithofacies. In addition, higher solute concentrations (0.12) and CO_2 saturations (0.06 at early time and 0.10 at late time) were observed when the fracture partially penetrated the caprock. Mass-balance calculations for the single-phase models ranged from 60-100%, varying with geometry. By contrast, mass-balance calculations for the multi-phase results were about 100%, for the fracture at the interface case.

(4) The caprock may be capable of storing significant amounts of CO_2 near the injection well. This is the result of flow of CO2 into permeable facies within caprocks.

Variations observed in fracture density indicates that it may be possible to predict the likelihood of similar features forming in a given subsurface site. For example, models that compare fracture density data to curvature results show that a relationship may exist between curvature and fracture density. Fewer fractures show evidence of fluid interactions at our sites where curvature values are lower in the syncline hinge of the San Rafael Swell monocline, suggesting that fracture connectivity to reservoir fluids may be related to fracture density. Therefore, a unique curvature threshold may exist for any given reservoir-seal pair for which there is minimal risk of seal failure.

Fractures and deformation bands have not been observed at the reservoir/caprock interface between the Mount Simon Sandstone and Eau Claire Formation. Nevertheless, the observation that deformation bands are locally present in some Mount Simon

Sandstone cores leaves open the possibility that deformation band to opening-mode fracture transitions similar to those observed in our outcrop analogues exist. Additional work is needed to further constrain this possibility.

Finally, although not directly relevant to the present study, the high degree of heterogeneity documented in the pore networks of the Mount Simon Sandstone is potentially good news in terms of using the unit for carbon storage. Such heterogeneity provides greater-than-normal opportunities for residual trapping of CO2, thus improving the likelihood of successful long-term storage.

ACKNOWLEDGEMENTS

Many people helped us with various aspects of this project. Our project managers at NETL, first Dawn Deal and then Brian Dressel, kept us on track with reporting and budget matters, and were always available to answer our sometimes naive questions. Dr. Mark Person (New Mexico Tech) supervised much of the modeling efforts and accompanied us in the field, for which we are exceedingly grateful. Dr. Carl Gable, Dr. Phil Stauffer, and Dr. Sharad Kelkar (Los Alamos National Laboratories) assisted us in developing the multi-phase flow models. This material is based upon work supported by the U.S. Department of Energy (DOE) National Energy Technology Laboratory (NETL) under Grant Number DEFE0004844. This project is managed and administered by the New Mexico Institute of Mining and Technology and funded by DOE/NETL and cost-sharing partners.

REFERENCES

Barton, D.C., 2011, Determining CO_2 storage potential: Characterization of seal integrity and reservoir failure in exposed analogs [M.S. Thesis]: Utah State University, Logan, Utah, 177 p.

Bird, P., 1998, Kinematic history of the Laramide orogeny in latitudes 35°-49°, western United States: Tectonics, v. 17, no. 5, p. 780-801.

Birkeland, P.W., 1984, Soils and Geomorphology: New York, Oxford University Press, 372 p.

Blakey, R.C., Peterson, F., Caputo, M.W., Geesaman, R.C., and Voorhees, B.J., 1983, Paleogeography of Middle Jurassic continental, shoreline, and shallow marine sedimentation, southern Utah, in Reynolds, M.W. and Dolley, E.D., eds., Mesozoic Paleogeography of the West Central United States: Society of Economic Paleontologists and Mineralogists, Rocky Mountain Sect., Symp., v. 2, p. 77-100.

Boles, J.R., and Johnson, K.S., 1984, Influences of mica surfaces on pore-water pH: Chemical Geology, v. 43, p. 303-317.

Bower, K.M., Gable, C.W., Zyvoloski, G.A., 2005. Grid resolution study of ground water flow and transport. Ground Water 43, 122-132.

Brace, W. F., 1980, Permeability of crystalline and argillaceous rocks. International Journal of Rock Mechanics and Mining Sciences & Geomechanics Abstracts, 17(5), 241–251.

Bump, A.P. and Davis, G.H., 2003, Late Cretaceous-early Tertiary Laramide deformation of the northern Colorado Plateau, Utah and Colorado: Journal of Structural Geology, v. 25, no. 3, p. 421-440.

Butler, D.L., 2014, Effects of meso-scale deformation features at the reservoir-caprock interface: Implications for carbon capture and storage projects [M.S. Thesis]: New Mexico Institute of Mining and Technology, Socorro, New Mexico, 62 p.

Caillet, G., 1993, The caprock of the Snorre Field, Norway: a possible leakage by hydraulic fracturing. Marine and Petroleum Geology, 10, 42 50.

Cartwright, J., Huuse, M., and Aplin, A., 2007, Seal bypass systems: American Association of Petroleum Geologists Bulletin, v. 91, n. 8, p. 1141-1166.

Chentnik, B., 2012, Characterizing fractures and deformation bands:_ Implications for long term CO_2 storage within the Cambrian Mount Simon Sandstone: Journal of Purdue Undergraduate Research, v. 2, p. 8–15.

Chopra, S. and Marfurt J., 2007, Curvature attribute applications to 3D surface seismic data: The Leading Edge, v. 26, p. 404-414.

Davis, G.H., and Bump, A. P., 2009, Structural geologic evolution of the Colorado Plateau: Geological Society of America Memoir, v. 204, p. 99-124.

Doelling, H.H., 2002, Interim geologic map of the San Rafael Desert 30' x 60' Quadrangle, Emery and Grand Counties, Utah: Utah Geological Survey Open-file report 404, scale 1:100,000.

Eschner, T., and Kocurek, G., 1986. Marine destruction of eolian sand seas: origin of mass flows. Journal of Sedimentary Petrology, 56(3), 401–411.

Fischer, M.P. and Wilkerson, M.S., 2000, Predicting the orientation of joints from fold shape: results of pseudo-three-dimensional modeling and curvature analysis: Geology, v. 28, p. 15-18.

Fischer, M.P., and Christensen, R.D., 2004, Insights into the growth of basement uplifts deduced from a study of fracture systems in the San Rafael monocline, east central Utah: Tectonics, v. 23, p. 1-14.

Flores, S.L., 2014, Mesoscale deformational features near outcrop analogs of a reservoir-seal interface: Implications for seal failure [M.S. Thesis]: Utah State University, Logan, UT, 143 p.

Fossen, H., Schultz, R.A., Shipton, Z.K., and Mair, K., 2007, Deformation bands in sandstone: a review: Journal of the Geological Society of London, v. 164, p. 1-15.

Fothergill, C.A., 1955, The cementation of oil reservoir sands and its origin: Proc. 4th World Petroleum Conference, Rome, 301-314.

Garden, I. R., Guscott, S. C., Burley, S. D., Foxford, K. A., Walsh, J. J., & Marshall, J., 2001, An exhumed palaeo-hydrocarbon migration fairway in a faulted carrier system, Entrada Sandstone of SE Utah, USA. Geofluids, 1(3), 195–213.

Hall, J.S., Mozley, P.S, Davis, J.M, and Delude Roy, N., 2004, Environments of formation and controls on the spatial distribution of calcite cementation in Plio-Pleistocene fluvial deposits, New Mexico, U.S.A.: Journal of Sedimentary Research, v. 74, p. 643-653.

Hawley, C.C., Robeck, R.C., and Dyer, H.B., 1968, Geology altered rocks and ore deposits of the San Rafael Swell, Emery County, Utah: United States Geological Survey Bulletin 1239, 115 p.

Hawkes, C. D., Bachu, S. & McLellan, P. J., 2004, Geomechanical factors affecting geological storage of CO_2 in depleted oil and gas reservoirs. Journal of Canadian Petroleum Geology 44(10), 52-61.

Hegland, R., 2005, Using gas chimneys in seal integrity analysis: A discussion based on case histories. In "(P. Boult and J. Laldi, J., eds.) "Evaluating fault and cap rock seals", AAPG Hedberg Series, no. 2, 237-245.

Hennings, P.H., Olson, J.E., and Thompson, L.B., 2000, Combining outcrop data and three-dimensional structural models to characterize fractured reservoirs: an example from Wyoming: American Association of Petroleum Geologists Bulletin, v. 84. p. 830-849.

Holtz, M. H., 2002, Residual gas saturation to aquifer influx: A calculation method for 3-D computer reservoir model construction, SPE 75502.

Huyakorn, P.S., 1983. Computational methods in subsurface flow. Academic Press, New York, NY.

Ingram, G.M. and Urai, J. L., 1999, Top-seal leakage through faults and fractures: the role of mudrock properties. In (Applin, A.C., Fleet, A.J., and Macquaker, J.H.S., eds) "Muds and Mudstones: Physical and Fluid Flow Properties". Geological Society, London, Special Publications 158, 125-135.

IPCC, 2005, IPCC Special Report on Carbon Dioxide Capture and Storage. Prepared by Working Group III of the Intergovernmental Panel on Climate Change [Metz, B., O. Davidson, H. C. de Coninck, M. Loos, and L. A. Meyer (eds.)]. Cambridge University Press, Cambridge, United Kingdom and New York, NY, USA, 442 pp.

Klein, J.S., Mozley, P.S., Campbell, A., and Cole, R., 1999, Spatial distribution of carbon and oxygen isotopes in laterally extensive carbonate cemented layers: Implications for mode of growth and subsurface identification: Journal of Sedimentary Research, v. 69, p. 184-201.

Laubach, S.E., Olson, J.E., and Gross, M.R., 2009, Mechanical and fractures stratigraphy: The American Association of Petroleum Geologists, v. 93, p. 1413-1426.

Lisle, R.J., 1992, Constant bed-length folding: three-dimensional geometrical implications: Journal of Structural Geology, v. 14, p. 245-252.

Lisle, R.J., 1994, Detection of zones of abnormal strains in structures using Gaussian curvature analysis: American Association of Petroleum Geologists Bulletin, v. 78, p. 1811-1819.
Marino, J., 1992, Erg Margin and Marginal Marine Facies Analysis of the Entrada Sandstone, San Rafael Swell, Utah: Implications to Hydrocarbon Entrapment. BYU Master's Thesis.
Moraes, M.A.S., and Surdam, R.C., 1993, Diagenetic heterogeneity and reservoir quality - fluvial, deltaic, and turbiditic sandstone reservoirs, Potiguar and Reconcavo rift basins, Brazil: American Association of Petroleum Geologists, v. 77, p. 1142.
National Research Council, 1996, Rock Fractures and Fluid Flow: Contemporary Understanding and Applications. National Academy Press, Washington D.C., 551 p.
Nelson, R.A. 2001, Geological Analysis of Naturally Fractured Reservoirs, 2nd edition. Gulf Publishing Co., Houston, Texas, 352 p.
Nelson, P.H., 2009, Pore-throat sizes in sandstones, tight sandstones, and shales: AAPG Bulletin, v. 93, no. 3 (March 2009), pp. 329–340.
Payne, W.G., 2011, Controls on porosity and permeability in the Carmel Formation: Implications for carbon sequestration at Gordon Creek, Utah [M.S. Thesis]: New Mexico Institute of Mining and Technology, Socorro, New Mexico, 173 p.
Person, M., Banerjee, A., Hofstra, A., Sweetkind, D., Gao, Y.L., 2008. Hydrologic models of modern and fossil geothermal systems in the Great Basin: Genetic implications for epithermal Au-Ag and Carlin-type gold deposits. Geosphere 4, 888-917.
Petrie, E.S., Evans, J.P., and Bauer, S.J., 2014, Failure of caprock seals as determined from mechanical stratigraphy, stress history and tensile failure analysis of exhumed analogs: American Association of Petroleum Geologists Bulletin.
Raduha, S.P., 2013, Influence of Mesoscale Features of the Reservoir-Caprock Interface on Fluid Transmission into and through Caprock [M.S. Thesis]: New Mexico Institute of Mining and Technology, Socorro, New Mexico, 272 p.
Reddy, J.N., 1984. An Introduction to the Finite Element Method. McGraw-Hill College, New York.
Reynolds, S.D., Paraschivoiu, E., Hillis, R.R., O'Brien, G.W., 2005, A regional analysis of fault reactivation and seal integrity based on geomechanical modeling: An example from the Bight Basin, Australia, In "(P. Boult and J. Laldi, J., eds.) "Evaluating fault and cap rock seals", AAPG Hedberg Series, no. 2, 57-71.
Richey, D.J., 2013, Fault Seal Analysis for CO_2 Storage: Fault Zone Architecture, Fault Permeability, and Fluid Migration Pathways in Exposed Analogs in Southeastern Utah [M.S. Thesis]: Utah State University, Logan, Utah, 172 p.
Roberts, A., 2001, Curvature attributes and their application to 3D interpreted horizons; First Break, v. 19, p. 85-100.
Rutqvist, J., Birkholzer, J. T. and Tsang, C. F., 2008, Coupled reservoir-geomechanical analysis of the potential for tensile and shear failure associated with CO_2 injection in multilayered reservoir-caprock systems. International Journal of Rock Mechanics and Mining Sciences 45(2), 132-143.
Saadatpoor, E., Byrant, S.L., and Sepehrnoori, K., 2010, New trapping mechanism in carbon sequestration: Transport in Porous Media, v. 82, p. 3–17.
Shipton, Z.K, J.P. Evans, K.R. Robeson, C.B. Forster, and S.H. Snelgrove. 2002, Structural heterogeneity and permeability in faulted eolian sandstone: Implications for subsurface modeling of faults. Am. Assoc. Pet. Geol. Bull., Vol. 86: 863-884.

Span, R., Wagner, W., 1996. A new equation of state for carbon dioxide covering the fluid region from the triple-point temperature to 1100 K at pressures up to 800 MPa. J. Phys. Chem. Ref. 25, 1509.
Suo, C., Peng, S., Chang, A., Rutai, D., Wang, G., 2012, A New Calculation Method of the Curvature to Predicting the Reservoir Fractures: Procedia Environmental Sciences, v. 12a, p 576-582.
Taylor, K.G., Gawthorpe, R.L., and Van Wagoner, J.C., 1995, Stratigraphic control on laterally persistent cementation, Book Cliffs, Utah: Journal of the Geological Society, London, v. 152, p. 225-228.
Taylor, K.G., Gawthorpe, R.L., Curtis, C.D., Marshall, J.D., and Awwiller, D.N., 2000, Carbonate cementation in a sequence-stratigraphic framework: Upper Cretaceous sandstones, Book Cliffs, Utah-Colorado: Journal of Sedimentary Research, v. 70, p. 360-372.
Theis, C.V., 1935. The relation between the lowering of the piezometric surface and the rate and duration of discharge of a well using ground water storage. US Department of the Interior, Geological Survey, Water Resources Division, Ground Water Branch.
Torabi, A., Fossen, H., & Alaei, B., 2008, Application of spatial correlation functions in permeability estimation of deformation bands in porous rocks. Journal of Geophysical Research, 113(B8), 1–10.
Verdon, J.P., Kendall, J.M., Stork, A.L., Chadwick, R.A., White, D.J., Bissell, R.C., 2013. Comparison of geomechanical deformation induced by megatonne-scale CO2 storage at Sleipner, Weyburn, and In Salah. P Natl Acad Sci USA 110, E2762-E2771.
Zheng, C., Wang, P.P., 1999. MT3DMS: A modular three-dimensional multispecies transport model for simulation of advection, dispersion, and chemical reactions of contaminants in groundwater systems; documentation and user's guide. DTIC Document, ADA373474, p. 219.
Zyvoloski, G., 2007. FEHM: A control volume finite element code for simulating subsurface multi-phase multi-fluid heat and mass transfer, in: Division, E.a.E.S. (Ed.). Los Alamos National Laboratory, LAUR-07-3359, Los Alamos, NM, p. 47.
Zyvoloski, G., Robinson, B., Dash, Z., Trease, L., 1999. Models and Methods Summary for the FEHM Application, in: Division, E.a.E.S. (Ed.). Los Alamos National Laboratory, SC-194, Los Alamos, NM, p. 74.
van Genuchten, M.T., 1980. A closed-form equation for predicting the hydraulic conductivity of unsaturated soils. Soil Science Society of America Journal 44, 892-898.